ΕΘΝΙΚΟ ΜΕΤΣΟΒΙΟ ΠΟΛΥΤΕΧΝΕΙΟ
ΣΧΟΛΗ ΠΟΛΙΚΩΝ ΜΗΧΑΝΙΚΩΝ

ΔΙΠΛΩΜΑΤΙΚΗ ΕΡΓΑΣΙΑ

Σεισμική Απόκριση Δεξαμενών Αποθήκευσης Υγρών με έμφαση στην Υδροδυναμική Καταπόνηση και σε Φαινόμενα Κοντινού Πεδίου

Seismic response of liquid-containing tanks with emphasis on the hydrodynamic distress and near-field phenomena.

Μαρίνα Ε. Καλογεράκου

Επιβλέπων:

Κ. Σπυράκος Καθηγητής Ε.Μ.Π.

Αθήνα

2015

ΠΕΡΙΛΗΨΗ

Αντικείμενο της παρούσας διπλωματικής εργασίας είναι η μελέτη της απόκρισης δεξαμενών αποθήκευσης υγρών με ειδική έμφαση σε φαινόμενα κοντινού πεδίου. Η κίνηση του υγρού εξετάζεται με βάση τις θεμελειώδεις αρχές της υδροδυναμικής και παρουσιάζεται η μεθοδολογία εύρεσης αναλυτικής λύσης. Κάνοντας χρήση πραγματικών επιταχυνσιογραφημάτων, και μέσω της τεχνικής του Ταχέως Μετασχηματισμού Φουριέ υπολογίζονται τα εντατικά μεγέθη (τέμνουσα βάσης, ροπή και πίεση επί των τοιχωμάτων) και το ύψος του κυματισμού. Ειδική έμφαση δίδεται στη συνεισφορά της δεύτερης ιδιομορφής. Μελετάται σε βάθος η σχέση μεταξύ του συχνοτικού περιεχομένου της εδαφικής κίνησης και της διέγερσης των διάφορων ιδομορφών ταλάντωσης, και τα αποτελέσματα της εργασίας συσχετίζονται με τις παραδοχές των ισχυόντων αντισεισμικών κανονισμών.

ABSTRACT

The aim of this dissertation is to study the behavior of liquid-containing tanks under seismic excitations with particular focus on near-fault phenomena. The fluid mechanics of sloshing are examined form first principles and their analytic treatment is given. Through the use of Fast Fourier Transform techniques and starting with accelerograms, we calculate force, pressure, moment, and height of the wave as functions of time. Particular emphasis on the contribution of the second convective mode to the above quantities is given. The relationship between the frequency content of seismic motion and the excitation of different hydrodynamic oscillatory modes (impulsive mode and convective modes) is studied. Findings of the present work are compared with the provisions of the Eurocode.

Table of Contents

1 Introduction

The aim of the dissertation is to study the behavior of liquid-containing tanks under seismic excitations. Special emphasis is given to the analysis of near-fault phenomena and their impact on the excitation of various modes of hydrodynamical oscillations. This is accomplished through an analytic treatment of the fluid-mechanical problem leading to expressions describing various dynamical quantities (force, pressure, moment) as well as the height of the wave. The relationship between the frequency content of the seismic motion and the excitation of the various oscillatory modes of fluid motion is studied in detail.

In section 2 we review the history of various seismic events with particular emphasis on the behavior of tanks. It becomes clear that the study of sloshing motion is important in the efficient design of such tanks.

Section 3 deals with fluid mechanics. In subsection 3.1 we review the main hydrodynamical assumptions, namely that the liquid adheres to the mechanics of incompressible, inviscid, irrotational flow. These assumptions lead, as is well-known, to the fact that the velocity potential obeys the Laplace equation. In subsection 3.2 we introduce the boundary conditions appropriate to the case of a fixed tank obeyed by the velocity potential on the tank walls and at the free surface and state the crucial assumption of small-amplitude waves. In subsection 3.3 we solve the Laplace equation and identify the normal modes. In subsection 3.4 we write the energy (kinetic plus gravitational potential) of a small-amplitude but otherwise arbitrary wave disturbance. In subsection 3.5 we consider the case of a tank accelerating in the x direction (the acceleration of gravity is in the z direction) and write down the boundary conditions appropriate to that case. The fact that the acceleration vanishes in the third direction restricts the number of modes we have to consider. In subsection 3.6 we write down expressions for the pressure, force and moment pertaining to a superposition of such modes. In subsection 3.7 we consider the response to sinusoidal lateral tank acceleration. In subsection 3.8 we consider a lateral excitation that is an arbitrary function of time using the methods of (i) the Duhamel integral, (ii) Fourier transformation. In the second method we take special care to ensure that the correct initial conditions at time $t = 0$ be obeyed. In the course of the argument we identify a natural splitting of the force to *impulsive* and *convective* components. In subsection 3.9 we review facts relate to the Fast Fourier Transform (FFT) method which is essential in the handling of time-histories.

In section 4 we compare the findings of section 3 with the provisions of the Eurocode.

In section 5 we apply the procedure developed in section 3 to the calculation of the response under (a) simplified pulses that simulate specific earthquakes, (b) original accelerograms of near-fault earthquakes. We look at three earthquakes and perform the analysis for four different values of the parameter H/R. One of the specific objectives is to analyze the importance of the second convective mode which is usually neglected in most provisions of the codes.

2 The behavior of liquid-containing tanks in major seismic events

2.1 Introduction

Storage tanks are widely used in many industrial facilities, and especially in the oil and gas industry. The consequences in the case of serious damage go beyond the economic value of the structure, to the harmful environment, business interruption..etc) apart from the economic value of the structure, in the case of water tanks water supply is immediately essential, following to the destructive earthquakes, not only to cope with possible subsequent fires, but also to avoid outbreaks of disease. Therefore, due to the requirement of remaining functional after a major earthquake event, the seismic performance of liquid storage tanks has been a matter of special importance.

The design of tanks can vary according to its use and construction limitations. Various types of tanks include concrete or steel, cylindrical, rectangular or spherical, vertical or horizontal, above or underground, ground supported or elevated. A typical tank consists of the steel cylindrical shells, a base plate, a roof, and roof support members. The behavior of the tank during an earthquake is a result of several different factors including the structural details of the tank (type of tank, material and size, foundation, supporting system etc.), the characteristics of the seismic motion and post-earthquake ground movements that may take place (such as ground sliding, liquefaction etc.) and the properties of the soil. The observation of the main damages in some major seismic events can give an insight about the various failure modes and the possible areas where the design process may need special attention . Often however such observations cannot lead to the evaluation of current design practice, since most events that demonstrated the importance of tank failures in the past concern tanks that were constructed prior to the existing regulation. Ohta and Zama (2005) documented fourteen cases of tank damage due to liquid sloshing (Figure 1). According to the report of Zama et al. (2012) damage to oil storage tanks is classified into three types on the basis of external forces (tsunami waves), long-period ground motions, and short-period strong ground motions. The effects of these three parameters in six major seismic events will be discussed in detail in the following subsection.

Earthquake	Year	M_W	Damage	Far-source?	Reference
Kanto	1923	7.9[a]	6,000 t oil tank	No	Hirano (1982)
Long Beach	1933	6.2	Water tank	Yes?	Steinbrugge (1970)
Kern County	1952	7.5	Oil tanks	Yes?	Steinbrugge and Moran (1954)
Alaska	1964	9.2	Many oil tanks, fires	Yes	Rinne (1967)
Niigata	1964	7.6[b]	Many oil tanks, fires	Yes	FDMA (1965)
Central Chile	1965	7.1[c]	Oil tanks	Yes	Shibata (1974)
San Fernando	1971	6.6	Oil tank	Yes	Shibata (1971)
Miyagi-oki	1978	7.4[d]	Oil tanks	Short period	FDMA (1979)
Imperial Valley	1979	6.5	Oil tank	No	Horoun (1983)
Coalinga	1983	6.2	Many oil tanks	No	Manos and Clough (1985)
Japan Sea	1983	7.7[e]	Many oil tanks, fire	Yes	Yoshiwara et al. (1984)
Kocaeli	1999	7.6	Many oil tanks, fires	No	JSCE (2000)
Chi-Chi	1999	7.7	Oil tanks	Yes	Yoshida et al. (2000)
Tokachi-oki	2003	8.3	Many oil tanks, fires	Yes	Ohta and Zama (2005)

The moment magnitudes were retrieved from the USGS earthquake database except for [a] Wald and Somerville (1995), [b] Ruff and Kanamori (1983), [c] M_S, [d] Seno et al. (1980), and [e] Dziewonski et al. (1983).

Figure 1: List of tank damage by liquid sloshing (Ohta and Zama 2005)

2.2 The response of liquid-containing tanks

2.2.1 The Great Alaskan Earthquake and Tsunami, 27 March 1964

One of the first earthquakes that triggered the interest in the investigation of the seismic response of storage tanks was the earthquake that struck the south coastal area of Alaska on March 27 in 1964, causing extensive damage to tanks and other structures. The epicenter was in the Northern part of Prince William Sound, about 120 km east of Anchorage and the magnitude of the earthquake was 9.2 Mw. The strong shaking was followed by the generation of a tsunami, causing fires and inundation in many waterfront areas. The main damages associated with tank failure took place in the following sites:

(i) At the time of the earthquake in the airport and the dock areas of Anchorage oil storage tanks of 13-37 m diameter and 13-16 m height were in existence. The soils in the dock area consisted mainly of silts and of a thick lens of "Bootlegger Cove Clay" . As observed from the data presented in Figure 2 full or nearly full tanks with ratio diameter/height (d/H) greater than 1.5 suffered mainly from damage to top shell and buckling of floating roof, whereas many with ratio $d/H < 1$ suffered from bottom shell buckling or collapsed (as it was reported, tanks less than half-full were not damaged by the earthquake) (Figure 3).

(ii) In Valdez (85 km from the epicenter) two tank farms with rel-

Tank	Diameter d m (ft)	Height H m (ft)	d/H	Damage Observed
A	9.1 (30)	14.6 (48)	0.63	Collapsed, failed
B	30.5 (100)	9.6 (32)	3.1	Damage to roof top shell and columns
C	13.7 (45)	9.6 (32)	1.4	Damage to roof top shell and buckled
D	36.6 (120)	9.6 (32)	3.8	Damage to roof top shell and columns
H	27.4 (90)	9.6 (32)	2.8	No damage except floating suction
I	16.7 (55)	7.0 (23)	1.7	Damage to top shell and rafters
J,K,L	9.1 (30)	12.2 (40)	0.75	Extensive bottom shell buckling
M	8.5 (28)	12.2 (40)	0.70	Collapsed, failed
N	12.8 (42)	12.2 (40)	1.05	Bottom shell buckling
O	6.1 (20)	12.2 (40)	0.50	Bottom shell buckling, broken shell/bottom weld
P	43.9 (144)	17.1 (56)	2.6	Floating roof buckled, large waves
Q	34.1 (112)	17.1 (56)	2.0	Floating roof damaged
R	14.9 (49)	14.6 (48)	1.02	Bottom buckled, 12-in uplift
S	27.4 (90)	14.6 (48)	1.9	3/4 full, roof and roof/shell damage

Figure 2: Anchorage tank properties and damage (National Institute of Science and Technology, 1997)

Figure 3: Tank with "elephant's foot" buckle at the base in the 1964 Anchorage, Alaska earthquake (http://www.fema.gov/ earthquake/fema-e-74-reducing-risks-nonstructural-earthquake-damage-31, PEER, Steinbrugge Collection, No. S2508)

atively small tanks and d/H ratios between 1.0 and 2.0 were damaged by the fire. Tanks were submerged by a landslide that occurred close to the shoreline .

(iii) In Whittier (60 km from epicenter) facilities and oil tanks were also destroyed by seismic sea waves and the spreading of flammable liquids along the waterfront

(iv) In Seward, located on the Gulf of Alaska about 135 km from the epicenter, the tsunami waves caused the sliding of a section of waterfront into the bay, followed by extensive fire destroying or badly damaging 18 of the 23 tanks that located on the site (Goto 2008).

(v) Nikiska, on the Kenai Peninsula, about 219 km from the epicenter is used by two oil refineries for the storage of LPG and crude oil. Tanks reported (National Institute of Science and Technology 1997) to have been damaged by the earthquake had diameters ranging from 8.5 m to 43.9 m and heights from 9.1m to 17.1m. Three tanks out of four with ratio $d/H < 1$ failed (one showing severe elephant foot buckling), and all five tanks with d/H about or above 1.5 had roof damage, but showed no buckling (some of them less than half-full).

Although much of the damage was caused by tsunami waves and post-tsunami widespread fires an important part of the damage was directly structural; under the same seismic conditions, the degree of damage and buckling of tank wall and roof differed according to d/H ratio and liquid level. Main observed types of failure included roof buckling, roof-column damage, roof-to-shell connection damage, shell buckling, and total collapse. In general, based on the reported data of Figure 4, it can be concluded that tanks nearly empty or partially full did not suffer great damage. Tanks with ratio $d/H < 1$ proved prone to bottom shell buckling type of failure (or "elephant's foot" bulge), and tanks with d/H ratio > 1.5 (in full conditions) to roof damage.

2.2.2 The Niigata Earthquake and Tsunami, 16 June 1964

On June 16, 1964 an earthquake of magnitude about 7.5 Mw occurred near the city of Niigata, north of middle Japan, causing widespread liquefaction which, along with the accompanying tsunami, led to major destruction along the coast of Japan.

The Showa Oil Co Niigata refinery plant located in the area comprised large crude oil tanks, including three floating roof-type 30,000 kl ones (51.1 m diameter by 14.5 m height) and two 45,000 kl ones (62 m diameter by 16.5 m height). The tanks were situated on roller compacted ground. The underlying soil consisted of loose, coarse dune sand and sedimentary deposits to a depth of 15 m, followed by a fine sand of sea-bed origin. The water table is shallow and is estimated to be about

Tank	Diameter d km (ft)	Height H km (ft)	d/H	Damage Observed
R200	9.1 (30)	14.6 (48)	0.63	Water, full, failed
R162	27.4 (90)	14.6 (48)	1.87	Full, cone roof damage no elephant foot buckling
R163	27.4 (90)	14.6 (48)	1.87	Full, cone roof damage no elephant foot buckling
R100	34.1 (112)	17.1 (56)	2.00	Floating roof, 1/6 full, roof damage
R120	21.3 (70)	14.6 (48)	1.46	Floating roof, 1/3 full, roof damage
R110	43.9 (144)	17.1 (56)	2.57	Floating roof, roof damage, 39 ft level
R140	14.9 (49)	14.6 (48)	1.02	Elephant foot buckling, no failure
AA4	3.2 (10.5)	9.1 (30)	0.35	1/3 full, walked, no damage
AA7	12.1 (40)	13.0 (42.5)	0.94	Severe elephant foot buckling, failed
AA5	8.5 (28)	12.2 (40)	0.70	Failure, collapsed

R designation believed to be Nikiska Refinery; AA is Anchorage Airport

Figure 4: (National Institute of Science and Technology 1997)

3m below the surface of the compacted mound.

The site is located about 56 km from the epicenter and peak acceleration was approximately 0.162 g in the North-South direction, 0.158 g in the East-West direction (Hausler and Sitar qwerty). The 4 m-high tsunami that followed the earthquake caused additional damage to storage tanks, spreading objects and leaking oil into the harbor, and inundating land. Burning crude oil spread over the water that flooded the area, causing the extension of the fire to other flammable parts of the plant and into residential areas, leading to massive destruction. (Iwabuchi et al., 2006).

The content of the tanks was subjected to large amplitude sloshing due to the long - period ground motion resulting from local liquefaction. Along with the uneven settlement caused by ground liquefaction, this resulted in ignition of the oil by sparks generated by the collision between the floating roof and the side wall. The sparks were generated by the metal touch sealing between the floating roof and the side wall (Akatsuka and Kobayashi qwerty). As a result five storage tanks caught fire including the large 30,000 kl tank which was full of oil. However little damage to tank bases was observed. Their settlements were estimated 20 to 30 cm, while tanks that were constructed on a thinner sand mound (30 cm) without contraction showed a significant settlement (about 50 cm) and tilt (Figure 5).

The Niigata earthquake was one of the first major seismic events to draw attention to the design of tanks against the combined action of

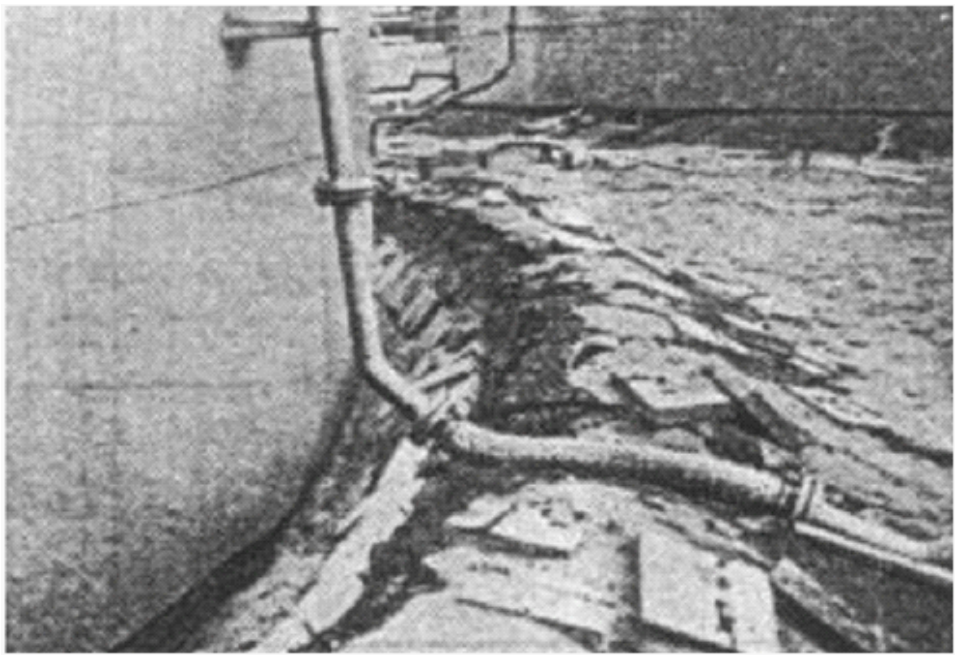

Figure 5: Settlement of tank on unimproved ground (Watanabe 1966)

various earthquake-related geo-hazards, such as ground shaking, excessive ground deformation caused by liquefaction, and inundation and fire caused by tsunami waves.

2.2.3 The Imperial Valley Earthquake, 17 October 1979

The Imperial Valley earthquake had a magnitude of 6.5 Mw and caused significant damage to a number of storage tanks located about 30 km from the epicenter. The Imperial fault, which was about 5 km east of the location of the tanks, generated surface movement in the proximity of the tanks.

Two tanks at the Imperial Irrigation District power plant, which were full at the time, sustained roof damage. Failure of the fixed steel-plate roof and separation of the perimeter weld around the roof allowed oil to spill over the top. Both tanks had a d/H ratio near 3, and the largest one that had 41.2 m diameter, 13.7 m height and a d/H ratio of 3 showed signs of uplifting.

A total number of eighteen unanchored tanks were located at the Southern Pacific Pipe Lines Inc. terminal, all constructed according to API 650 that was in effect at the time. The tanks' diameter varied between 6m and 24m and the ratio d/H was between 0.8 and 1.6. Four of them sustained damage in the form of a moderate elephant-foot buckling, and almost all had secondary problems such as roof seal dam-

TANK NO	DIAMETER d m (ft)	HEIGHT H_{TK} m (ft)	d/H	H_{LIQ} (ft)	PER UNIT FULL	FDN	ROOF
1	24. 4 (80)	14.6 (48)	1.67	(20.3)	.43	E	F
2	24.4 (80)	14.6 (48)	1.67	(23.4)	.49	E	F
3	20.4 (67)	12.3 (40.5)	1.65	(15.7)	.39	E	C
4	14.6 (48)	14.6 (48)	1.0	(25.5)	.53	E	F
5*	14.6 (48)	14.6 (48)	1.0	(34.9)	.73	E	F
6	13.0 (42.5)	12.2 (40)	1.06	(15.2)	.38	C	F
7	13.0 (42.5)	12.2 (40)	1.06	(15.7)	.40	C	C
8	24.7 (81)	14.6 (48)	1.53	(39.4)	.82	C	F
9	13.0 (42.5)	12.2 (40)	1.06	(25.8)	.65	C	F
10	13.0 (42.5)	12.2 (40)	1.06	(30.5)	.76	C	F
11	14.2 (46.5)	12.2 (40)	1.16	(34.4)	.86	C	C
12	13.0 (42.5)	12.2 (40)	1.06	(34.5)	.86	C	F
13*	12.6 (41.25)	14.9 (49)	0.84	(43.5)	.70	C	CIP
14	14.7 (48.2)	14.9 (49)	0.84	(29.9)	.61	C	CIP
15	15.2 (49.8)	14.9 (49)	1.0	(29.8)	.61	C	CIP
16*	14.6 (48)	14.6 (48)	1.0	(39.9)	.83	C	CIP
C-1	6.5 (21.25)	7.3 (24.1)	0.88	(7.1)	.30	E	CIP
C-2	6.5 (21.25)	7.3 (24)	0.88	(9.4)	.39	E	F

FDN: E-ON EARTH (ROCK BASE), C-CONCRETE RINGWALL
ROOF: F-FLOATING ROOF, C-CONE, CIP-CONE/INTERNAL PAN
*: MAJOR DAMAGE

Figure 6: Details of the tanks located at the Southern Pacific Pipe Lines Inc. terminal (dimensions, fluid heights, type of foundation and roof design) (National Institute of Science and Technology 1997)

age, broken anti-rotation devices, relief piping damage, grounding cable pulled off, settlement and roof strain, and swing line damage. The tank that suffered greatest damage had a cone roof with an internal floating pan, a concrete ring wall foundation and was 70% full at the time of the earthquake. The damage consisted of a severe elephant foot buckling (with an arc over 90 degrees) and a 10 cm weld separation at the shell-bottom plate joint causing a gasoline leakage. Two other cone roof tanks (one with internal floating pan and one without) that were over 70% full suffered also significant damage. The details (dimensions, fluid heights, type of foundation and roof design) of the eighteen tanks of the site are presented in Figure 6.

The performance of these various types of tanks shows both the vulnerability and survivability of tanks subject to strong shaking. Among the tanks with earth foundation the one that suffered major damage had a much higher liquid height than the others. Tanks with cone roof and internal pan are the most vulnerable (out of five tanks with cone roof and internal pan two sustained major damage, whereas among the thirteen

Figure 7: Collapse of a steel tank during the 1979 Imperial Valley Earthquake. (http://nisee.berkeley.edu/jpg/6257_3021_0662/IMG0037.jpg, Steinbrugge Collection, Earthquake Engineering Research Center, UC Berkeley)

without internal pan only one was severely damaged). Regarding the foundation system "compression buckles were more prominent in tanks supported on concrete ring walls than those on gravel fill" (EERI 1986). According to the National Institute of Science and Technology 1997 report it is possible that some type of anchorage would have prevented a number of the above failures.

Minor to moderate damage was also reported in two elevated tanks. A 380,000 l water tank (30 m high by 9 m base) water tank with four tubular legs braced with tiers of diagonal rods collapsed during the earthquake.(EERI 1986) (Figure 7).

A brief description of the structural and nonstructural damages of unanchored tanks during the 1979 Imperial Valley earthquake is presented by Haroun (1983). He reports that buckling of the bottom of tank shells due to excessive compressive stresses, damage to fixed roofs due to liquid sloshing and failure of attached pipes due to their inability to allow for the shell movement occurred.

2.2.4 The Coalinga Earthquake, 2 May 1983

On May 2, 1983 an earthquake of magnitude 6.7 Mw shook the town of Coalinga, California causing serious damage throughout the epicentral region. A number of large diameter (over 31 m) oil storage tanks were located at several sites, labeled below by A to F, within a relatively short distance (about 6.5 km) from the epicenter. The peak acceleration in the area was estimated between 0.60 g and 0.82 g, and the foundation soil consisted mainly of alluvium deposits. The tanks were of cylindrical shape, ground supported and unanchored, and most of them had floating roofs (National Institute of Science and Technology 1997). The main observed damages and structural details of oil storage tanks in various sites within the epicentral region included:

(i) site A (6 km east of the epicenter): out of nineteen tanks (built 70 years before the earthquake) only the two largest tanks, which were at the moment nearly full, suffered floating roof damage.

(ii) site B (5 km north-east of the epicenter): tanks of 43 m diameter and 14.8 m height with concrete ring foundations, 1/4 inch bottom plate, constructed in 1956 according to API Standard 650 sustained some secondary roof seal damage (which occurred also to one which was nearly empty), with oil splashing over the top.

(iii) site C (4.5 km southwest of the epicenter): a mainline crude oil pumping station used four large tanks with 61.5 m diameter by 14.8 m height, built to the API Standard 650. Two tanks were built in the mid 1960s and had 1/4 inch bottom plate, and two were built in the mid 1970s and had $\frac{1}{2}$ inch annular rings. None had concrete ring foundations and all were set on gravel pads. All tanks (nearly full or nearly empty) incurred roof seal damage (90 degrees or more bending of the seal in the NE-SW direction). One tank which contained 10.7 m (out of 14.8 m) crude oil pounded into the foundation soil and splashed oil over the top. A water-draw bottom plate weld broke due to uplifting, allowing leakage of crude oil and bending a pipe support on the west side.

(iv) site D (3.2 m north of the epicenter): one of the two tanks suffered failure of the top riveted ring due to buckling. Figure 8 shows a bolted tank which pounded into the ground. Figure 9 shows oil roof spillage of a bolted tank located 16 km north of the epicenter.

(v) site E, where a gathering station with two bolted production tanks about 2 km south of the epicenter, with tanks of small d/H and set on crushed rock foundations, was located. Main damage consisted of broken cast iron valves and fittings, pulling of pipes out of Dresser Couplings, and a minor soil/tank settlement.

(vi) site F: a crude oil treatment facility about 6.5 km west off epicenter in which two bolted tanks of 17m diameter by 10m height that were

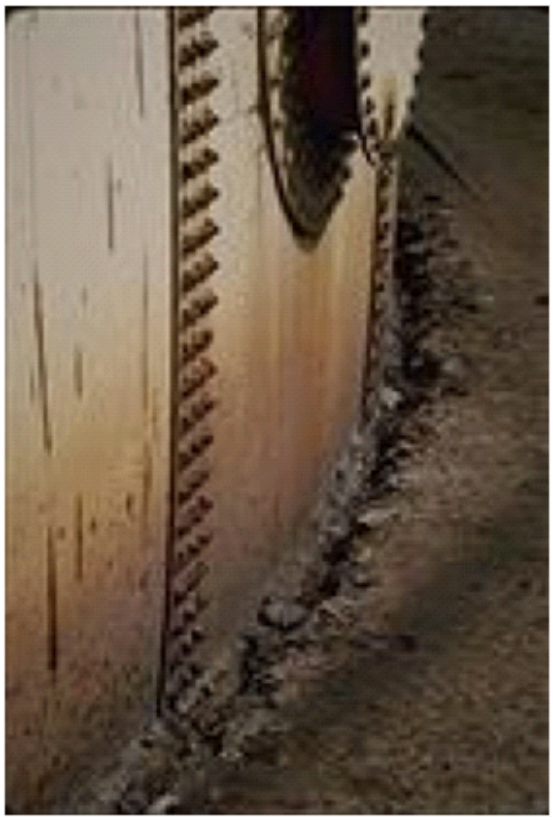

Figure 8: Settlement of the tank base (http://nisee.berkeley.edu/elibrary/Image/S5824, Karl V. Steinbrugge Collection: S5824)

Figure 9: Damage to Shell Oil tanks, Chevron Coalinga Station #4, north of Coalinga (http://nisee.berkeley.edu/elibrary/Image/S5813, Karl V. Steinbrugge Collection: S5813)

about three quarters full suffered elephant foot buckling, while other tanks that were less or equal to half-full had leakage at bolt holes and other minor damage.

Generally it was observed that large (about 60 m diameter) tanks are prone to uplift, that sloshing causes damage to the floating roof mechanism, and that smaller tanks can be susceptible to elephant foot buckling. Quoting Manos and Clough 1985: "current U.S. practice underestimates the sloshing response of tanks with floating roofs and does not adequately address the uplifting mechanism of unanchored ground supported tanks."

2.2.5 The Kocaeli Earthquake, Turkey, 17 August 1999

On August 17, 1999 an earthquake of 7.4 Mw struck the Kocaeli province or northwestern Turkey. The epicenter of the earthquake was 7 km southeast of Izmit (capitak of Kocaeli) and 80 km east of Istanbul. (Yazici and Cili, 2008)

Nearly half of the country's heavy industry is located in the Gulf of Izmit, which is in close proximity to the epicenter. The widespread damage of mechanical, electrical and plumbing facilities generated significant economic losses for the country. A number of petrochemical facilities that were damaged were located within 15 km from the epicenter where the levels of ground shaking were moderate to high.

(i) The Tupras oil refinery

The Tupras oil refinery, responsible for about one third of Turkey's total oil production, was constructed in 1961 according to the U.S. standards in effect at the time (Danis 1999), and expanded in size in 1974 and 1983. There were over 100 unanchored above-ground liquid storage tanks of various sizes in the refinery, many of which had floating roofs (Bendimerad et al, 2000). General earthquake response of tanks included buckling of tank walls, poor performance of floating roof systems, and fire related damages. The major fire occured in a floating-roof tank that contained naphtha (a highly volatile flammable liquid mixture distilled from petroleum). Excessive sloshing of the floating roof gave rise to sparks, due to the metal-to-metal contact between the metallic seal and tank wall, that ignited the naptha fuel. Four naptha tanks with diameters of 20-25 m and two with diameters of 10 m were burned down (Hamada, 1999). The fire later spread to crude and product oil, jet fuel and gasoline tanks damaging 30 of the 45 floating roof tanks in the crude and product oil storage area (Johnson, 2000). The fires caused an immediate evacuation and the multiple ruptures of the main water pipeline lead to a three day delay in their extinguishment. Danis (1999) reported substantial damage to a large number of tanks (30+) in the farm; the inability of perimeter seals to retain the sloshing fluid in the tanks resulted in failure or sinking of these floating roofs. Each of these damaged floating roofs required repair or replacement before the tanks could be returned to service. Sloshing of fluid caused overtopping in the tank of Figure 10 and extensive damage to the walls of the tanks of Figure 11. Although none of the tanks were anchored no significant sliding of the tanks was evident. Appreciable movement of the tanks would have caused failures of the hard piping that was attached to the base, but no such failures were observed. (ASCE 1997).

The near-fault ground motion observed near the tank damaged by the 1999 Kocaeli earthquake, which is the middle trace of the right-hand panel in qwerty Fig. 1, shows considerable later phases, which resulted in motion of longer duration compared to the other traces. This may be because of the long causative fault and site effect, and may have caused the exceptional tank damage.

(ii) The Habas plant

The Habas gas plant in Izmit provides liquefied gas for regional commercial plants and medical facilities. Primary damage consisted of the collapse of two of the three identical cylindrical elevated liquid storage tanks due to failure of their support structures, as shown in Figure 12. The three 14.63 m-diameter tanks were built in 1995. Each tank was made of two concentric stainless steel shells, an inside shell with a diameter of 12.80 m and an outer shell with a diameter of 14.63 m. The gap

Figure 10: Overtopping of tank wall due to sloshing and failure of perimeter seals (http://nisee.berkeley.edu/turkey/Fturkch4.pdf)

Figure 11: View of tank wall damage. (http://nisee.berkeley.edu/turkey/Fturkch4.pdf)

Figure 12: Liquid gas plants at the Habas plant (http://nisee.berkeley.edu/turkey/Fturkch4.pdf)

Figure 13: Buckling of the outer stainless steel shell in liquid oxygen tank (http://nisee.berkeley.edu/turkey/Fturkch4.pdf)

between the shells was filled with insulation material. Both shells were supported on a 1.07 m-thick reinforced concrete slab that was supported by sixteen identical reinforced concrete columns of 200 mm-diameter and qwerty 2.54 height. Columns were reinforced with sixteen 16 mm-diameter longitudinal bars and 8 mm-diameter spiral ties with a spacing of 100 mm. The two collapsed tanks containing liquid oxygen are shown in Figure 12. The two tanks containing liquid nitrogen were undamaged, and so was the supporting structure except for some hairline cracks in the columns. The two oxygen-containing damaged tanks were reported to be 85% full while the third nitrogen-containing tank was 25% (Sezen and Whittaker (2006), Hamada (1999)). The outer shells of the collapsed tanks buckled (Figure 13). Photographs of some of the failed columns beneath one of the liquid nitrogen tanks are presented in Figure 14.

2.2.6 Tohoku Earthquake and Tsunami, Japan, 11 March 2011

On 11 March 2011 a strong earthquake of Mw 9.0 that occurred off the Pacific coast of Tohoku shook Miyagi Prefecture and generated a tsunami wave causing extensive damage to oil storage tanks and to other hazardous materials facilities in the petrochemical industrial complex.

Figure 14: Failed columns beneath slab under liquid oxygen tank, Habas facility (http://nisee.berkeley.edu/turkey/Fturkch4.pdf)

Oil storage tanks and pipelines on the Pacific coast of northeast Japan were led by the tsunami to drift and collapse. On the Japan Sea coast of northwest Japan and Tokyo Bay area long-period strong ground motions excited large liquid sloshing of oil storage tanks and caused sinking of floating roofs. Although PGA more than 0.5 g was observed near tank sites along the coast of northeast Japan, oil storage tanks were damaged indirectly by liquefaction of soil rather than directly. About 1,404 hazardous materials facilities were damaged by the strong ground motion and 1,807 hazardous materials facilities were damaged by the tsunami (Nishi 2012) (accounting for 1.6% of the total surveyed hazardous materials facilities in the east Japan area). A total of 284 fires spawned by the tsunami occurred in 42 facilities (FDMA 2012) including two major oil refineries (Scawthorn 2013).

Due to the tsunami one empty tank submerged and many pipelines were bent. The latter caused substantial oil spill in the Sendai dyke. A section of the Sendai refinery housing gasoline, asphalt and molten sulfur tanks was burnt-down. The probable cause is the collision of tank lorries against oil handling facilities, which was caused by the tsunami. In Kesennuma city 22 out of 23 oil storage tanks were washed away resulting to leakage of heavy oil, kerosene, diesel fuel and gasoline. The total amount of liquid lost is estimated at about 12,000 kl. In Kuji city underground oil tanks escaped damage whereas all aboveground tanks were destroyed.

Oil storage tanks suffered damages such as sinking of inner roof, leakage of oil onto deck, deformation of gauge pole, and fracture of pontoon. These were caused by long period ground motion that excited the sloshing mode in the tanks. The complete breaking down of a gasoline tank in Sakata city is attributed by Zama et al. (2012) to the excitement of the sloshing mode; the authors estimate the period of the first order mode at 4.19 sec.

Zama et al. (2012) report that short period ground motions ($0.3 - 0.5$ Hz) caused elephant foot bulge of a water tank at Sendai and extraction of anchor bolts of an oil storage tank at Kashima. According to the press release of August 2011 by Cosmo Oil Company (http://www.cosmo-oil.co.jp/eng/press/110802/) regarding the disaster at the Ichihara refinery, an LPG tank happened to be filled with water at the time of the earthquake, rather than with the lighter LPG (the tank was in the process of being cleaned and inspected). The first earthquake exerted heavy load on the braces and some of them were fractured (Figure 15). As a result of the second earthquake, about one and a half hour later, the tank collapsed leading to damage of several pipes near the tank and to subsequent LPG leakage. The company has been unable to identify

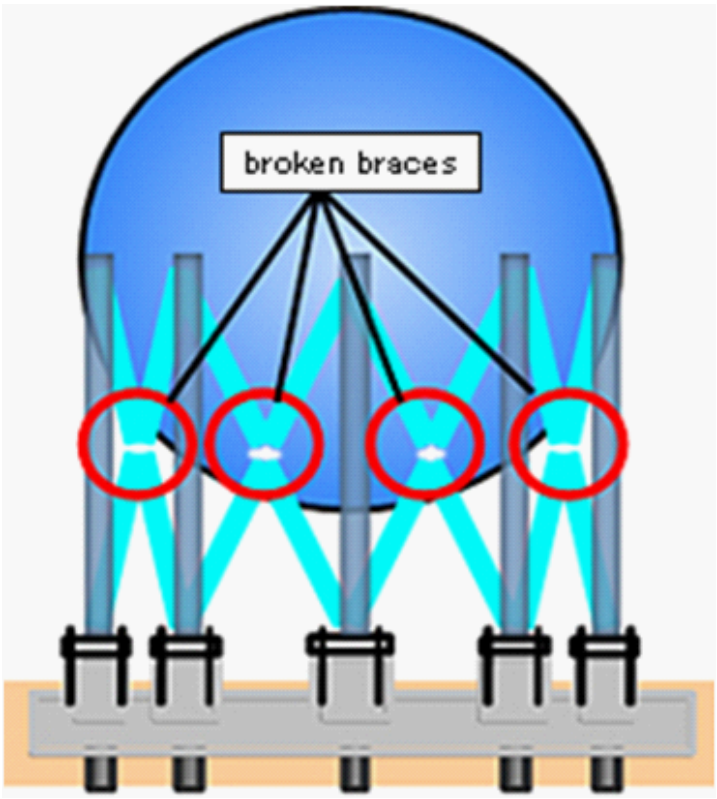

Figure 15: Braces broke that supported the legs holding the LPG tank (http://www.cosmo-oil.co.jp/eng/press/110802/)

Figure 16: Tank settlement due to liquefaction around the foundation (Zama S et al. 2012)

the cause of the ignition of the leaked LPG tank. The diameter of the largest fire ball in the explosions was about 600 m. Many fragments of the LPG tanks were scattered as a result of the explosions spreading the fire to the asphalt tanks, the control room and the neighboring factory. Metal sheets flew to adjacent inhabited areas leading to an evacuation order.

In Iwaki city damage inflicted to tanks was due to liquefaction caused by strong ground motions. Figure 16 shows the valve of a tank almost touching the ground due to liquefaction around its foundations. Furthermore the center part of bottom plate was uplifted about 50cm high owing to the lateral flow of neighboring soil of the tank, and the welding area of the bottom plate cracked and oil leaked.

2.3 Discussion

The preceding subsections lead to the conclusion that the behavior of a storage tank during an earthquake depends on several different factors including the structural details of the tank (type of tank, material

Figure 17: Elephant-foot bulge (Hosseinzadeh (2008))

and size, foundation, supporting system etc.), the characteristics of the seismic motion and post-earthquake ground movements that may take place (such as ground sliding, liquefaction etc.) and the properties of the soil. Folowing Priestley, Wood and Davidson (1986), Barros(2004),and the report of the Task Committee on Seismic Evaluation and Design of the Petrochemical Committee of the Energy Division of the American Society of Civil Engineers (2011) we identify various observed types of failure:

1. Buckling of tank wall above base known as "elephant foot bulge" (Figure 17), which typically occurs around the perimeter of unanchored tanks due to large compressive stress of the tank wall. Another less common (and less damaging) buckling mode of the tank shell is the "diamond shape" buckling, usually associated with taller tanks with very thin shells.

2. Damage of the upper shell of the tank wall and/or roof as well as failure of frangible joints between wall and roof due to long-period

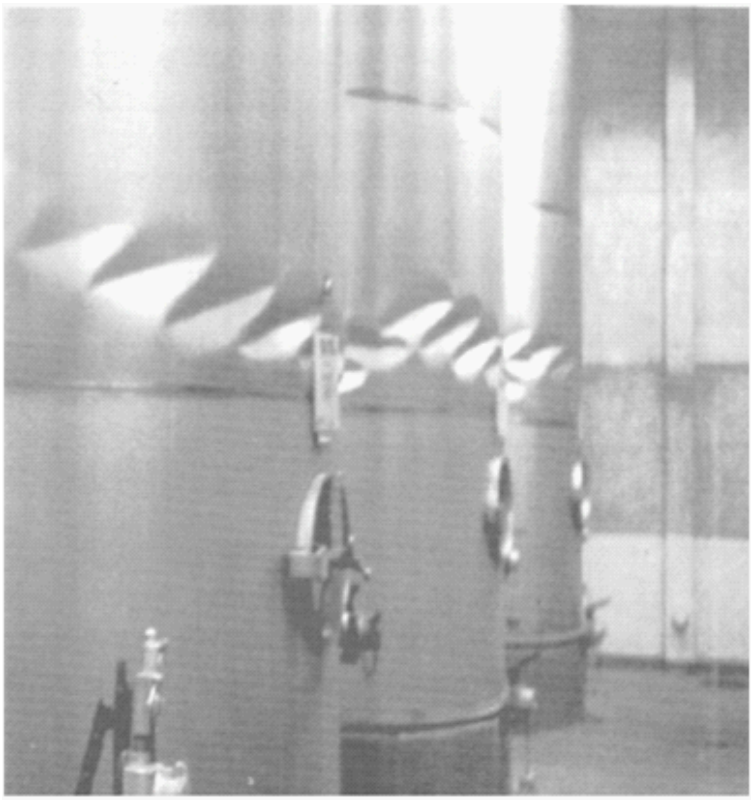

Figure 18: Diamond-shaped buckling (Barros 2004))

Figure 19: Roof damage by liquid sloshing (Hosseinzadeh (2008))

sloshing of fluid and hydrodynamic pressure (Figure 19).

3. Weld failure between the bottom plate and the tank shell as a result of high-tension forces during uplift.

4. Breakage of piping connected to the tank shell or bottom plate due to lack of flexibility in the piping system to accommodate the resulting uplift (Figure 20).

5. Foundation failure by differential settlements associated with liquefaction of soils.

6. Failure of inner supporting columns leading to roof buckling for fixed roof tanks and failure of the tank support system for elevated tanks.

7. Tearing of the tank shell or failure of the anchorage due to non-ductile anchorage

connection details for anchored tanks.

8. Tearing of tank shell or bottom plate due to over-constrained stairway, ladder, or piping anchored at a foundation and at the tank

Figure 20: Failure of connections between piping and tank wall (Seyed-Razzaghi and Eshghi (2004))

shell. Tearing of tank shell due to over-constrained walkways connecting two tanks experiencing differential movement.

9. Sliding/rocking/overturning of tank.

10. Splitting of tank shells subsequent leakage due to high tensile hoop stress in bolted or riveted tanks.

3 Dynamics of a fluid in a tank

3.1 Generalities

In this chapter we study the mechanics of a fluid in a container subject to a given acceleration. The first study of the distribution of water pressure in a rectangular tank caused by a simulated earthquake is presented in Hoskins and Jacobsen (1934), where experimental data are also given. The authors work in the impulsive approximation, i. e. they neglect the second term in the left hand side of (6); they also neglect the g-dependent term in the right hand side of (6), the reasoning being that their treatment addresses the motion of the fluid short after the external excitation has acted and before gravity waves are set up. A treatment of the somewhat similar problem of earthquake-produced water waves in a basin and of the subsequent pressure exerted on a dam is presented in Westergaard (1931). A more thorough treatment of water waves in an accelerating tank, again in the impulsive approximation but now including the case of cylindrical geometry, is given in Jacobsen (1949). Inclusion of both impulsive and convective terms in (6) was first presented in three papers by Housner in 1954,1957 and 1963. He uses a simplified hydrodynamical model, the benefit being that the results do not involve Bessel functions. In his study he also takes into account the flexibility of the tank walls. In his treatment of tanks with rigid walls, Housner provided a mechanical analog that has been widely used ever since: the total fluid mass is divided in two parts, one that does not participate in oscillations, and a few (typically at most four) oscillating masses attached to the wall at different heights by springs of different spring constants. We review his results in subsection 2.8.4 below. Haroun (who was Housner's student) treats cylindrical containers with flexible walls based on assumptions **A1** to **A5** below. Veletsos (1984) gives a full treatment of both impulsive and convective terms for cylindrical tanks following mainstream methods of hydrodynamics. Further to the above developments that sprang from the civil engineering community, it must be noted that the problem of sloshing in cylindrical containers has been widely studied by the rocket science community since the 1950s (we refer to the sloshing of the propellant inside a rocket tank subject to acceleration). Important contributors include Abramson, Ransleben, Bauer and Ibrahim and references are given in Ibrahim's book (2005).

Following Haroun we present the fundamental fluid-mechanical assumptions **A1** to **A4**:

A1 No sources or sinks are anywhere in the flow field.

Clearly this assumption is certainly valid in the situations we are

going to consider. As a result we may write down the continuity equation valid throughout the flow field:

$$\frac{\partial \rho}{\partial t} + \boldsymbol{\nabla} \cdot (\rho \mathbf{v}) = 0. \tag{1}$$

A2 The fluid is inviscid.

The absence of viscosity means that no energy is dissipated to heat. In thermodynamic terms this means that entropy stays constant (*isentropic flow*). In the case of a gas constancy of entropy, i.e. absence of heat flow, implies that pressure and density are connected via the adiabatic law $p = \text{const} \cdot \rho^{\gamma}$, where $\gamma = c_p/c_v$.

A3 Liquids are taken to be incompressible.

Incompressibility, i.e. density being constant in space as well as in time, means that we neglect sound waves in the liquid. This is probably a good assumption at least as long as velocities are small, i.e. smaller than the speed of sound in the liquid. As a result of this assumption equation (1) simplifies greatly since (a) $\partial\rho/\partial t = 0$, (b) ρ can be taken outside the divergence. Thus the continuity equation reads:

$$\boldsymbol{\nabla} \cdot \mathbf{v} = 0. \tag{2}$$

A4 The flow field is irrotational.

This means that no vortices appear. Given the way that a tank is excited by the earthquake this is probably a good assumption. Mathematically it is equivalent to the vanishing of the curl of the velocity:

$$\boldsymbol{\nabla} \times \mathbf{v} = 0. \tag{3}$$

This in turn means that the velocity can be written as the gradient of a potential (the velocity potential):

$$\mathbf{v} = \boldsymbol{\nabla} \Phi. \tag{4}$$

We substitute (4) in (2) to deduce:

$$\nabla^2 \Phi = 0. \tag{5}$$

Thus the velocity potential $\Phi(x, y, z, t)$ obeys Laplace's equation. Our main task in this chapter is to solve (5) subject to boundary conditions that shall be discussed below.

3.2 Fluid mechanics in a fixed tank

The motion of a fluid is governed by Newton's law. If the only external force acting on the fluid is gravity (the acceleration of gravity pointing

downwards along the z axis) then Newton's law reads (see chapter 2 of Curle and Davies (1968))

$$\frac{\partial \mathbf{v}}{\partial t} + (\mathbf{v} \cdot \boldsymbol{\nabla})\, \mathbf{v} = -\frac{1}{\rho}\boldsymbol{\nabla} p - g\mathbf{k}, \tag{6}$$

where is the unit vector along the z axis and p is the gauge pressure (the difference between fluid pressure and atmospheric pressure). We use the well-known vector identity

$$\frac{1}{2}\boldsymbol{\nabla}\left(v^2\right) = \mathbf{v}\times(\boldsymbol{\nabla}\times\mathbf{v}) + (\mathbf{v}\cdot\boldsymbol{\nabla})\,\mathbf{v}, \tag{7}$$

together with $\boldsymbol{\nabla}\times\mathbf{v}=0$ to rewrite (6) in the form

$$\frac{\partial \mathbf{v}}{\partial t} + \frac{1}{2}\boldsymbol{\nabla}\left(v^2\right) = -\frac{1}{\rho}\boldsymbol{\nabla} p - g\mathbf{k}, \tag{8}$$

or, using (4),

$$\boldsymbol{\nabla}\left(\frac{\partial \Phi}{\partial t} + \frac{1}{2}\left(\boldsymbol{\nabla}\Phi\right)^2 + \frac{p}{\rho} + g\left(z - H\right)\right) = 0, \tag{9}$$

where H is the height of the liquid at rest. Physically, writing $g\left(z-H\right)$ instead of gz means that we take gravitational potential energy to be zero at the surface of the liquid at equilibrium. The fact that the parenthesis in (9) has zero gradient means that the former is a constant that can be taken to be zero (strictly speaking it can be any function of time but it is easily shown in fluid mechanics textbooks that it can in fact be set equal to zero). Thus,

$$\frac{\partial \Phi}{\partial t} + \frac{1}{2}\left(\boldsymbol{\nabla}\Phi\right)^2 + \frac{p}{\rho} + g\left(z - H\right) = 0. \tag{10}$$

This is *Bernoulli's equation* valid at all instants and at all points in space.

In the case of a fixed wall the boundary condition that accompanies (5) is that the velocity of the fluid normal to the surface vanishes, i.e. there is no penetration of fluid into the surface:

$$\mathbf{n}\cdot\mathbf{v} = 0, \tag{11}$$

where $\mathbf{n}$ is the unit vector normal to the surface. In terms of the velocity potential the above reads:

$$\mathbf{n}\cdot\boldsymbol{\nabla}\Phi = 0. \tag{12}$$

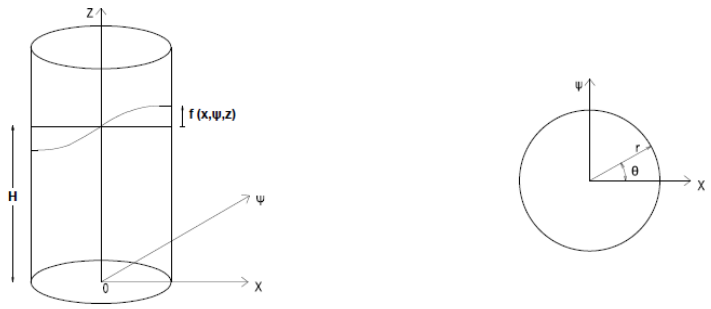

Figure 21: Tank geometry

This equation is to be applied at the bottom and at the sides of the tank.

We now have to impose boundary conditions at the free surface of the liquid. One requirement is that the velocity of the surface at a certain point coincides with the velocity of a liquid particle at the same point. This is the so-called kinematic boundary condition. To formulate it in a precise way we take the case of a cylindrical tank and introduce a coordinate system $Oxyz$ with the z axis coinciding with the axis of a cylinder and the plane $x - y$ coinciding with the bottom base of the cylinder (see Figure 21). The liquid surface is described by the function $\xi(x, y, t)$ that gives the deviation from the equilibrium level:

$$\xi(x, y, t) = z - H. \tag{13}$$

The kinematic boundary condition assumes the form (see Appendix A):

$$\frac{\partial \xi}{\partial t} + \frac{\partial \Phi}{\partial x}\frac{\partial \xi}{\partial x} + \frac{\partial \Phi}{\partial y}\frac{\partial \xi}{\partial y} - \frac{\partial \Phi}{\partial z} = 0. \tag{14}$$

A further boundary condition is provided by the requirement that the pressure at the surface be equal to the atmospheric, i.e. that the gauge pressure be zero. This is the so-called *dynamic* boundary condition. Setting $p = 0$ in (10) we obtain

$$\frac{\partial \Phi}{\partial t} + \frac{1}{2}\left(\boldsymbol{\nabla}\Phi\right)^2 + g\xi = 0. \tag{15}$$

At this point following Haroun we introduce a further assumption **A5**:

Deviations from equilibrium are small (linear approximation). Neglecting quadratic terms some of the above equations simplify greatly.

Bernoulli's equation (10) reads

$$\frac{\partial \Phi}{\partial t} + \frac{p}{\rho} + g(z - H) = 0, \tag{16}$$

the kinematic boundary condition (14) reads

$$\frac{\partial \xi}{\partial t} - \frac{\partial \Phi}{\partial z} = 0, \tag{17}$$

and the dynamic boundary condition (15) reads

$$\frac{\partial \Phi}{\partial t} + g\xi = 0. \tag{18}$$

We combine (17) and (18) to obtain

$$\frac{\partial^2 \Phi}{\partial t^2} + g\frac{\partial \Phi}{\partial z} = 0. \tag{19}$$

This is a surface boundary condition expressed wholly in terms of Φ, and in the spirit of the linear approximation it is to be applied at the equilibrium level $z = H$.

3.3 Solution of the Laplace equation subject to the boundary conditions previously derived

A sloshing mode $\Phi(x, y, z, t)$ is a solution of Laplace equation subject to boundary conditions (12) and (19). We introduce cylindrical coordinates r, ϑ (see Figure 21):

$$r = \sqrt{x^2 + y^2}, \quad x = r\cos\vartheta, \quad y = r\sin\vartheta. \tag{20}$$

Laplace's equation in cylindrical coordinates reads (see chapter 7 of Spiegel (1959))

$$\nabla^2 \Phi = \frac{\partial^2 \Phi}{\partial r^2} + \frac{1}{r}\frac{\partial \Phi}{\partial r} + \frac{1}{r^2}\frac{\partial^2 \Phi}{\partial \vartheta^2} + \frac{\partial^2 \Phi}{\partial z^2} = 0. \tag{21}$$

From here to equation (30) we follow Appendix I-c of Haroun (1980). We solve (21) by the method of separation of variables, i. e. we write

$$\Phi(r, \vartheta, z, t) = \tilde{T}(t)\tilde{\Theta}(\vartheta)\tilde{R}(r)\tilde{Z}(z), \tag{22}$$

where $\tilde{T}$, $\tilde{\Theta}$, $\tilde{R}$, $\tilde{Z}$ are functions of t, ϑ, r, z respectively. We obtain for $\tilde{\Theta}$:

$$\tilde{\Theta}(\vartheta) = \alpha_n \cos(n\vartheta) + \beta_n \sin(n\vartheta), \tag{23}$$

where n is a non-negative integer. We note that (i) the function $\tilde{R}$ must obviously be non-singular at $r = 0$ and (ii) boundary condition (12) applied at the bottom of the tank reads

$$\frac{d\tilde{Z}}{dz} = 0 \quad \text{at } z = 0. \tag{24}$$

Conditions (i) and (ii) are satisfied by the following form of $\tilde{R}\tilde{Z}$

$$\tilde{R}(r)\tilde{Z}(z) = J_n(\kappa r)\cosh(\kappa z), \tag{25}$$

where J_n is the Bessel function of order n (non-singular at $r = 0$), n is the integer appearing in (23) and κ is a positive number. The function J_n satisfies the Bessel equation:

$$r^2\frac{d^2\tilde{R}}{dr^2} + r\frac{d\tilde{R}}{dr} + \left(\kappa^2 r^2 - n^2\right)\tilde{R} = 0. \tag{26}$$

We now turn to boundary condition (12) and apply it at the side-walls of the tank (i.e. at $r = R$). By expressing $\boldsymbol{\nabla}\Phi$ in cylindrical coordinates

$$\boldsymbol{\nabla}\Phi = \frac{\partial\Phi}{\partial r}\hat{\mathbf{r}} + \frac{1}{r}\frac{\partial\Phi}{\partial\vartheta}\hat{\boldsymbol{\vartheta}} + \frac{\partial\Phi}{\partial z}\hat{\mathbf{z}}, \tag{27}$$

we obtain

$$\frac{\partial\Phi}{\partial r} = 0 \quad \text{at} \quad r = R. \tag{28}$$

In terms of solution (25) this reads

$$J_n'(\kappa r) = 0 \quad \text{at} \quad r = R, \tag{29}$$

where the prime in (29) denotes derivative with respect to the argument. For a certain value of the index n we denote by λ_{nm} the zeros of J_n'. Then equation (29) gives

$$\kappa_{nm} = \frac{\lambda_{nm}}{R}. \tag{30}$$

For a certain value of the index $n = 0, 1, 2, ..$ equation (30) gives the allowed values of $m = 1, 2, .. .$ The integers n, m label the sloshing modes of a rigid cylindrical tank. In Appendix B we quote the first five zeros for $n = 0, 1, 2$ and $m = 1, 2,..,5$.

We combine (22), (23), (25) and (30) to write down the velocity potential for a mode (n, m):

$$\Phi_{nm} = \tilde{T}_{nm}(t)\Psi_{nm}, \tag{31}$$

$$\Psi_{nm} = \left(\alpha_n\cos(n\vartheta) + \beta_n\sin(n\vartheta)\right) J_n\left(\lambda_{nm}\frac{r}{R}\right)\cosh\left(\lambda_{nm}\frac{z}{R}\right). \tag{32}$$

To determine $\tilde{T}_{nm}$ we use the last remaining boundary condition (19) at $z = H$ which, in terms of (31), (32), reads

$$\frac{d^2\tilde{T}_{nm}}{dt^2}\cosh\left(\lambda_{nm}\frac{H}{R}\right) + \lambda_{nm}\frac{g}{R}\sinh\left(\lambda_{nm}\frac{H}{R}\right)\tilde{T}_{nm} = 0. \tag{33}$$

This is the equation of an harmonic oscillator. If we write

$$\tilde{T}_{nm}(t) = A_{nm}\cos\left(\omega_{nm}t\right), \tag{34}$$

where A_{nm} is the amplitude and where we made a choice of phase, then the angular frequency for the (n, m) mode is given by the expression

$$\omega_{nm}^2 = \lambda_{nm}\frac{g}{R}\tanh\left(\lambda_{nm}\frac{H}{R}\right). \tag{35}$$

For example for a tank of radius $R = 15$ m and height of wetted surface $H = 7.5$ m the period of the $(1, 1)$ mode is 6.7 s. For a saucepan of radius $R = 0.1$ m and height $H = 0.02$ m the period of the $(1, 1)$ mode is 0.8 s. In terms of the period $\tau_{nm} = 2\pi/\omega_{nm}$ equation (35) takes the form

$$\frac{\tau_{nm}^2}{4\pi^2}\frac{g}{R} = \frac{1}{\lambda_{nm}}\coth\left(\lambda_{nm}\frac{H}{R}\right), \tag{36}$$

where the left hand side is obviously dimensionless. In Figure 22 we plot the angular frequency as a function of H/R.

For a tank with given R we observe that as the height of the liquid increases, the angular frequencies of the various modes approach asymptotically constant values. For the first mode, the approach to the asymptotic value starts when H becomes somewhat larger than R. For higher modes, the asymptotic value is achieved for much smaller heights. Using (34) in (31) we write down the full expression for the (n, m) mode:

$$\Phi_{nm} = A_{nm}\cos\left(\omega_{nm}t\right)\left(\alpha_n\cos\left(n\vartheta\right) + \beta_n\sin\left(n\vartheta\right)\right)J_n\left(\lambda_{nm}\frac{r}{R}\right)\cosh\left(\lambda_{nm}\frac{z}{R}\right). \tag{37}$$

The constants A_{nm}, α_n, β_n are determined from the initial conditions. The surface displacement is obtained from (18) (valid at $z = H$):

$$\begin{aligned}\xi_{nm}(r, \vartheta, t) = &\frac{1}{g}\omega_{nm}A_{nm}\cosh\left(\lambda_{nm}\frac{H}{R}\right)\sin\left(\omega_{nm}t\right)\\ &\times\left(\alpha_n\cos\left(n\vartheta\right) + \beta_n\sin\left(n\vartheta\right)\right)J_n\left(\lambda_{nm}\frac{r}{R}\right).\end{aligned} \tag{38}$$

It shall be seen in following subsections that lateral acceleration (acceleration along the $x-$axis) excites the $(1, m)$ modes with $\beta_1 = 0$. It may

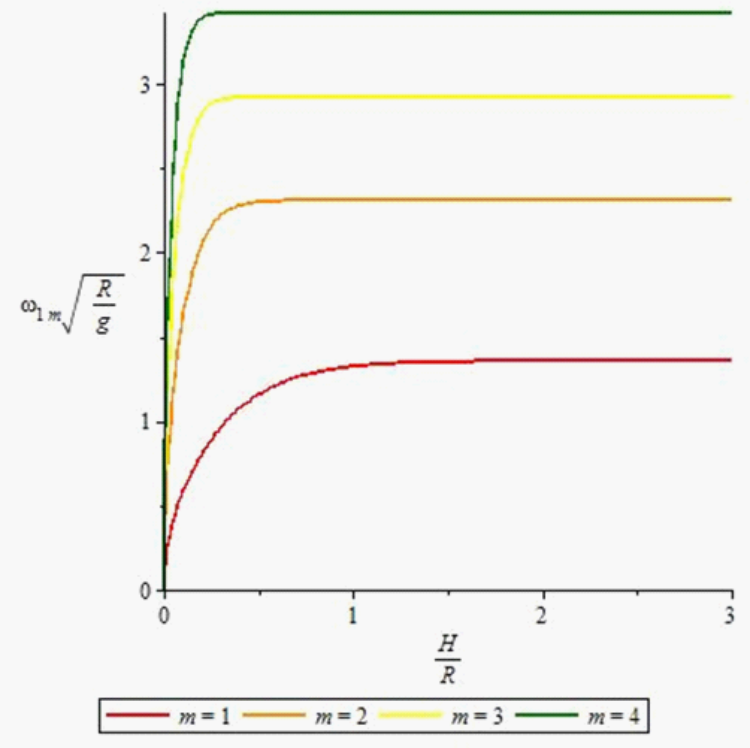

Figure 22: Scaled frequencies of the first three convective modes vs H/R

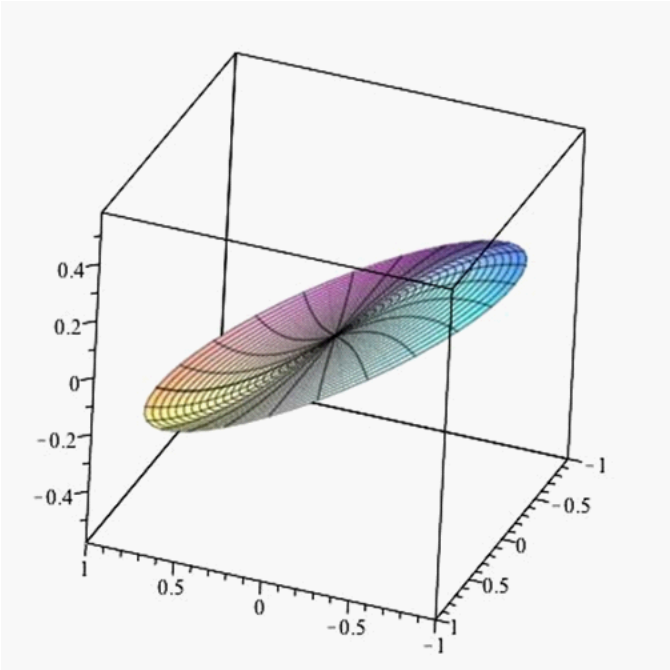

Figure 23: Plot of $\xi_{11}(r, \vartheta)$

thus be of interest to provide plots for the surface displacements ξ_{11}, ξ_{12}, ξ_{13} (Figures 23 to 25). In each figure, the bottom plane coincides with the horizontal plane, and the elevation ξ is measured along the third axis. The scale in this plot is arbitrary. In the case where $\beta_i = 0, \alpha_1 \neq 0$, $\alpha_{i\neq 1} = 0$ the extreme displacements take place along the horizontal axis ($\vartheta = 0$) and the displacement always vanishes for $\vartheta = \pi/2$ (the y axis is the *line of nodes).* It is explained after (63) that these are the modes relevant to lateral excitation along the x axis. The intersections of the red curve with the x axis determine the mode frequencies. The shape of the first eigenmode (see Figure) is described by the portion of the blue curve between the origin and the first zero, the shape of the second eigenmode (see Figure) is described by the portion of the blue curve between the origin and the second zero etc.

The pressure corresponding to an (n, m) mode is obtained from the Bernoulli equation (16)

$$\begin{aligned} & p_{nm}(r, \vartheta, z, t) \\ & = \rho g(H - z) + \rho \omega_{nm} A_{nm} \sin(\omega_{nm} t) \\ & \times (\alpha_n \cos(n\vartheta) + \beta_n \sin(n\vartheta)) J_n\left(\lambda_{nm} \frac{r}{R}\right) \cosh\left(\lambda_{nm} \frac{z}{R}\right), \end{aligned} \tag{39}$$

where the first term is the usual hydrostatic pressure.

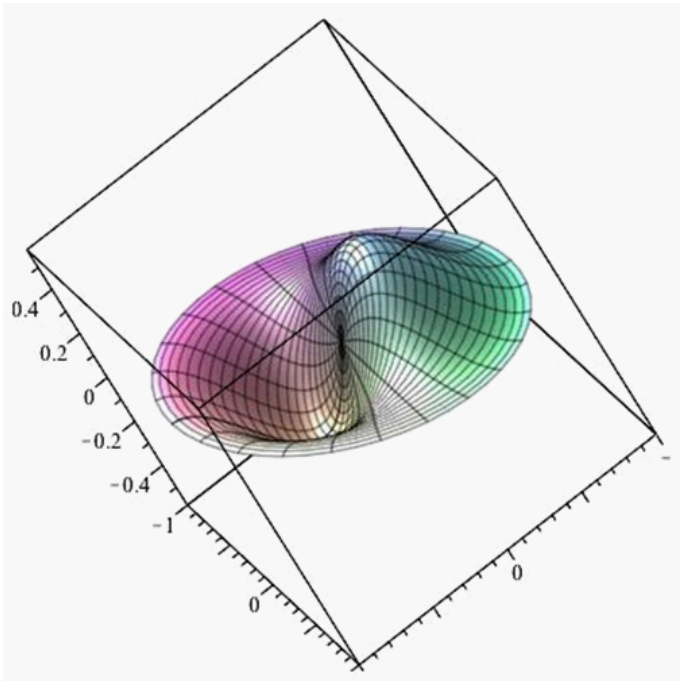

Figure 24: Plot of $\xi_{12}(r, \vartheta)$

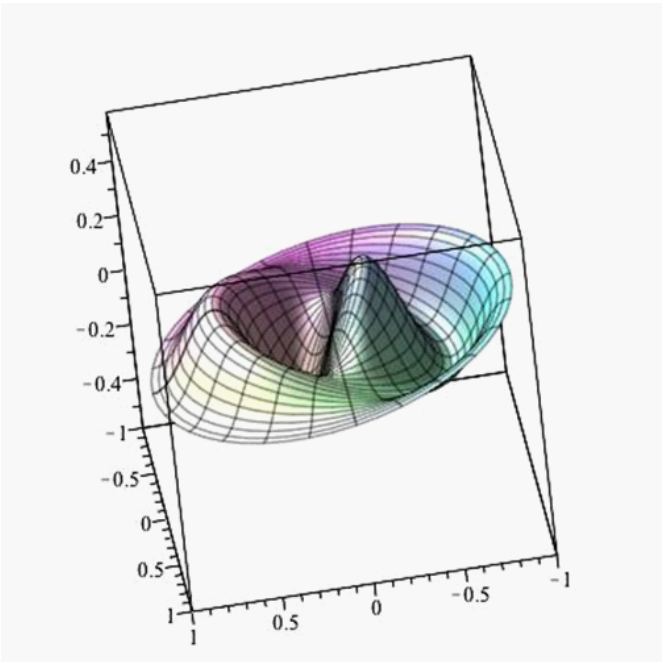

Figure 25: Plot of $\xi_{13}(r, \vartheta)$

3.4 General expression for the fluid energy in a fixed tank

In this subsection we derive general expressions for the total kinetic K and gravitational potential V energies of the fluid. To calculate V we divide the fluid to columns of base area dS and height z. The potential energy of one column is (*mass* $\rho z dS$) $\times$ (*acceleration of gravity* g) $\times$ (*height of center of mass of column* $z/2$):

$$V = \frac{1}{2}\rho g \int_S dS z^2 \tag{40}$$

where S is the cross-section of the cylinder. In terms of ξ (13):

$$V = \frac{1}{2}\rho g \int_S dS \left(\xi^2 + 2\xi H + H^2\right). \tag{41}$$

The third term in the above integral leads to a contribution equal to $\pi R^2 H^2 \varrho g/2 = m_l g H/2$, and this is the potential energy of the fluid at rest. Measuring potential energy differences with respect to the fluid at rest this term can be dropped. Using eqn (18) we obtain

$$V = \frac{\rho}{2g}\int_S dS \left(\frac{\partial \Phi}{\partial t}\right)^2 - \rho H \int_S dS \frac{\partial \Phi}{\partial t}. \tag{42}$$

The kinetic energy of the fluid is

$$K = \frac{1}{2}\varrho \int dV v^2, \tag{43}$$

where v is the magnitude of the velocity and where we took into account that due to incompressibility the density is uniform and can be taken outside the integral sign. The integration in (43) is over the whole volume of the fluid. In terms of the velocity potential

$$K = \frac{1}{2}\varrho \int dV \left(\boldsymbol{\nabla}\Phi\right)^2. \tag{44}$$

We integrate the above by parts to obtain a volume term and a surface term:

$$K = -\frac{1}{2}\varrho \int dV \Phi \nabla^2 \Phi + \frac{1}{2}\rho \int_{boundary} dS \ \left(\hat{\mathbf{n}} \cdot \boldsymbol{\nabla}\Phi\right)\Phi, \tag{45}$$

where the surface integral is over the whole boundary of the fluid and $\hat{\mathbf{n}}$ is the outer normal to the boundary. We note that (a) the volume

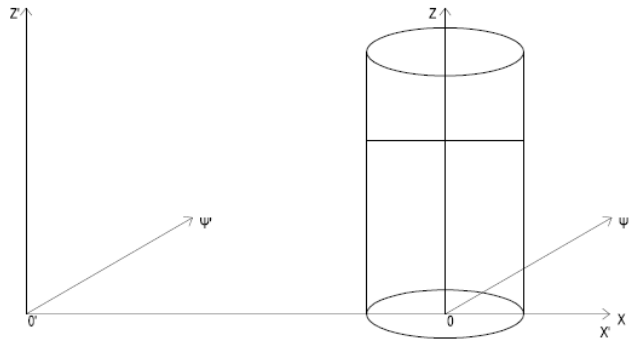

Figure 26: Fixed and accelerated coordinate systems

integral vanishes due to Laplace's eqn (5), (b) the surface integral over the base and the walls of the tank vanishes due to boundary condition (12). We are thus left with the surface integral over the free surface of the fluid. In the linear approximation where the height of the wave is small compared to wavelength we can set

$$\hat{\mathbf{n}} \simeq \mathbf{k} \Rightarrow \hat{\mathbf{n}} \cdot \boldsymbol{\nabla}\Phi \simeq \mathbf{k} \cdot \boldsymbol{\nabla}\Phi = \frac{\partial \Phi}{\partial z}.$$

Hence, the kinetic energy takes the form

$$K = \frac{1}{2}\varrho \int\limits_S dS \frac{\partial \Phi}{\partial z}\Phi, \tag{46}$$

and the final expression for the total energy is

$$E = K + V = \frac{1}{2}\varrho \int\limits_S dS \frac{\partial \Phi}{\partial z}\Phi + \frac{\rho}{2g}\int\limits_S dS \left(\frac{\partial \Phi}{\partial t}\right)^2 - \rho H \int\limits_S dS \frac{\partial \Phi}{\partial t}. \tag{47}$$

3.5 Fluid mechanics in an accelerating tank

We consider a rigid tank performing accelerated translational motion along the Ox axis. The coordinate system $Oxyz$ is fixed at the tank and is defined as previously (O is the center of the tank's circular base). We consider an inertial frame $O'x'y'z'$ with axes $O'x', O'y', O'z'$ respectively parallel to Ox, Oy, Oz (Figure 26). We intend to describe the sloshing modes from the point of view of an observer accelerating with the tank.

Let $\mathbf{X}_O$ be the position vector of the center of the base with respect to the inertial frame, $\mathbf{V}_O$ its velocity and $\mathbf{a}_O$ its acceleration. If f is any

mechanical quantity (either scalar or component of a vector) then

$$\left(\frac{\partial f}{\partial t}\right)_{\text{inertial}} = \left(\frac{\partial f}{\partial t}\right)_{\text{tank}} - \mathbf{V}_O \cdot \boldsymbol{\nabla} f \tag{48}$$

and

$$\frac{\partial f}{\partial x'} = \frac{\partial f}{\partial x}, \quad \frac{\partial f}{\partial y'} = \frac{\partial f}{\partial y}, \quad \frac{\partial f}{\partial z'} = \frac{\partial f}{\partial z}. \tag{49}$$

where by definition

$$\mathbf{V}_O = \frac{d\mathbf{X}_O}{dt}.$$

Newton's law (6) refers to the inertial frame and reads

$$\left(\frac{\partial \mathbf{v}}{\partial t}\right)_{\text{inertial}} + (\mathbf{v} \cdot \boldsymbol{\nabla})\, \mathbf{v} = -\frac{1}{\rho}\boldsymbol{\nabla} p - g\mathbf{k}. \tag{50}$$

We use (48) and (49) to rewrite the above

$$\left(\frac{\partial \mathbf{v}}{\partial t}\right)_{\text{tank}} - (\mathbf{V}_O \cdot \boldsymbol{\nabla})\, \mathbf{v} + (\mathbf{v} \cdot \boldsymbol{\nabla})\, \mathbf{v} = -\frac{1}{\rho}\boldsymbol{\nabla} p - g\mathbf{k}. \tag{51}$$

In what follows time derivatives shall always refer to the tank and the subscript shall be omitted. We express the fluid velocity as a sum of the tank velocity and of a relative velocity

$$\mathbf{v}(x, y, z, t) = \mathbf{V}_O(t) + \mathbf{v}_{rel}(x, y, z, t), \tag{52}$$

and substitute in (51) to obtain

$$\frac{\partial \mathbf{v}_{rel}}{\partial t} + (\mathbf{v}_{rel} \cdot \boldsymbol{\nabla})\, \mathbf{v}_{rel} = -\frac{1}{\rho}\boldsymbol{\nabla} p - g\mathbf{k} - \mathbf{a}_O(t). \tag{53}$$

Equation (53) is probably obvious: comparing with equation (6) we see that as far as relative motion is concerned the acceleration of the tank is equivalent to a gravitational field in the direction opposite to that of the acceleration. We can now consider small displacements and velocities of the liquid relative to the tank and simplify the above:

$$\frac{\partial \mathbf{v}_{rel}}{\partial t} = -\frac{1}{\rho}\boldsymbol{\nabla} p - g\mathbf{k} - \mathbf{a}_O(t). \tag{54}$$

In what follows we shall take motion of the tank along the $x-$axis and thus write

$$\frac{\partial \mathbf{v}_{rel}}{\partial t} = -\frac{1}{\rho}\boldsymbol{\nabla} p - g\mathbf{k} - a_O(t)\mathbf{i}. \tag{55}$$

From (52) we see that $\boldsymbol{\nabla} \times \mathbf{v} = 0$ implies that $\boldsymbol{\nabla} \times \mathbf{v}_{rel} = 0$, so we can introduce a velocity potential for $\mathbf{v}_{rel}$:

$$\mathbf{v}_{rel} = \boldsymbol{\nabla}\Phi. \tag{56}$$

Then equation (55) reads

$$\frac{\partial \boldsymbol{\nabla}\Phi}{\partial t} = -\frac{1}{\rho}\boldsymbol{\nabla}p - g\mathbf{k} - a_O(t)\mathbf{i}, \tag{57}$$

or

$$\boldsymbol{\nabla}\left(\frac{\partial \Phi}{\partial t} + \frac{p}{\rho} + g(z-H) + a_O(t)x\right) = 0. \tag{58}$$

Hence Bernoulli's equation for an accelerated tank reads:

$$\frac{\partial \Phi}{\partial t} + \frac{p}{\rho} + g(z-H) + a_O(t)x = 0. \tag{59}$$

From (56) and (2) we obtain Laplace's equation (5) valid for the relative velocity potential. As previously, this has to be solved subject to appropriate boundary conditions.

Equations (12), (24) and (28) are still valid. Physically they reflect the fact that the relative velocity has no component perpendicular to the walls of the tank. The solution to Laplace's equation under these boundary conditions still has the form (31), (32). It is shown in Appendix A that the kinematic boundary condition still has the form (17). Thus, the acceptable sloshing modes are of the form Φ_{nm} given from (31). However the dynamic boundary condition obtained from Bernoulli's equation now reads (setting $p = 0$ in (59)):

$$\frac{\partial \Phi}{\partial t} + g\xi + a_O(t)x = 0 \quad \text{at} \quad z = H. \tag{60}$$

Equation (59) agrees with equation (2.2d) of Ibrahim (2005). We differentiate (60) with respect to time and combine with (17) to deduce the surface boundary condition appropriate for an accelerating tank

$$\frac{\partial^2 \Phi}{\partial t^2} + g\frac{\partial \Phi}{\partial z} + \dot{a}_O(t)x = 0 \quad \text{at} \quad z = H, \tag{61}$$

where a dot indicates derivative with respect to time. Equation (61) agrees with equation (2.3) of Ibrahim (2005). It is important to observe that boundary condition (61) is *non-homogeneous*. We thus express the velocity potential Φ as a superposition

$$\Phi = \sum_{n=0}^{\infty}\sum_{m=1}^{\infty} T_{nm}\Psi_{nm}, \tag{62}$$

where T_{nm} are certainly different from $\tilde{T}_{nm}$ and are to be determined. Note that the units of T_{nm} are meter^2/second. We substitute (62) in (61) to obtain:

$$\sum_{n=0}^{\infty}\sum_{m=1}^{\infty}\frac{d^2T_{nm}}{dt^2}\left(\alpha_n\cos\left(n\vartheta\right)+\beta_n\sin\left(n\vartheta\right)\right)J_n\left(\lambda_{nm}\frac{r}{R}\right)\cosh\left(\lambda_{nm}\frac{H}{R}\right)+$$
$$\frac{g}{R}\sum_{n=0}^{\infty}\sum_{m=1}^{\infty}\lambda_{nm}T_{nm}\left(\alpha_n\cos\left(n\vartheta\right)+\beta_n\sin\left(n\vartheta\right)\right)J_n\left(\lambda_{nm}\frac{r}{R}\right)\sinh\left(\lambda_{nm}\frac{H}{R}\right)+$$
$$\dot{a}_O(t)r\cos\vartheta=0. \tag{63}$$

Equation (63) must be valid for all $0\leq\vartheta\leq2\pi$ and the only way that this can happen is if $\alpha_n=0$ and $\beta_n=0$ for $n\neq1$ and $\beta_1=0$, $\alpha_1\neq0$. Thus (63) simplifies to

$$\sum_{m=1}^{\infty}\frac{d^2T_{1m}}{dt^2}J_1\left(\lambda_{1m}\frac{r}{R}\right)\cosh\left(\lambda_{1m}\frac{H}{R}\right)+$$
$$\frac{g}{R}\sum_{m=1}^{\infty}\lambda_{1m}T_{1m}J_1\left(\lambda_{1m}\frac{r}{R}\right)\sinh\left(\lambda_{1m}\frac{H}{R}\right)+\dot{a}_O(t)r=0. \tag{64}$$

Further progress is made if we use the Fourier-Bessel expansion (178) for $x=r/R$

$$r=\sum_{m=1}^{\infty}\frac{2R}{\left(\lambda_{1m}^2-1\right)J_1\left(\lambda_{1m}\right)}J_1\left(\lambda_{1m}\frac{r}{R}\right), \tag{65}$$

and substitute it in (64) to obtain

$$\sum_{m=1}^{\infty}J_1\left(\lambda_{1m}\frac{r}{R}\right)\times$$
$$\times\left\{\frac{d^2T_{1m}}{dt^2}\cosh\left(\lambda_{1m}\frac{H}{R}\right)+\frac{g}{R}T_{1m}\lambda_{1m}\sinh\left(\lambda_{1m}\frac{H}{R}\right)+\frac{2R}{\left(\lambda_{1m}^2-1\right)J_1\left(\lambda_{1m}\right)}\dot{a}_O(t)\right\}=0. \tag{66}$$

Because $J_1\left(\lambda_{1m}r/R\right)$ are a set of orthogonal functions equation (66) can only be satisfied if

$$\frac{d^2T_{1m}}{dt^2}\cosh\left(\lambda_{1m}\frac{H}{R}\right)$$
$$+\frac{g}{R}T_{1m}\lambda_{1m}\sinh\left(\lambda_{1m}\frac{H}{R}\right)+\frac{2R}{\left(\lambda_{1m}^2-1\right)J_1\left(\lambda_{1m}\right)}\dot{a}_O(t)=0 \tag{67}$$

for each m separately. In the notation (35) the above reads

$$\frac{d^2T_{1m}}{dt^2} + \omega_{1m}^2 T_{1m} + \zeta_m \dot{a}_O(t) = 0, \tag{68}$$

where

$$\zeta_m \equiv \frac{2R}{\left(\lambda_{1m}^2 - 1\right) J_1(\lambda_{1m}) \cosh\left(\lambda_{1m}\frac{H}{R}\right)} \tag{69}$$

is a length.

The conclusion from the above calculation is that in the case of lateral excitation only the $n = 1$ modes are excited. Haroun (1980) however points out that this conclusion is valid for strictly circular tanks and that small deviations from the perfect circle (which are in practice unavoidable) lead to non-negligible excitations of the $n \neq 1$ modes. Under this simplification the velocity potential (62) reads using (31), (32)

$$\Phi = \sum_{m=1}^{\infty} T_{1m} \cos\vartheta J_1\left(\lambda_{1m}\frac{r}{R}\right) \cosh\left(\lambda_{1m}\frac{z}{R}\right), \tag{70}$$

where the constant α_1 has been absorbed in T_{1m}. Equation (68) shows that each $(1, m)$ mode corresponds to a forced harmonic oscillator. The time dependence in $T_{1m}(t)$ is determined once a specific form for $\dot{a}_O(t)$ is known.

The height of the wave as a function of space and time is obtained from the dynamic boundary condition (60):

$$\xi = -\frac{1}{g}\frac{\partial\Phi}{\partial t} - \frac{a_O(t)x}{g} \tag{71}$$

We substitute (70) for the velocity potential and (88) for the acceleration in the above to express it in terms of dT_{1m}/dt:

$$\xi = -\frac{1}{g}\cos\vartheta \sum_{m=1}^{\infty} \frac{dT_{1m}}{dt} J_1\left(\lambda_{1m}\frac{r}{R}\right) \cosh\left(\lambda_{1m}\frac{H}{R}\right) - \frac{a_O(t)x}{g}. \tag{72}$$

3.6 Expressions for the pressure, force, and moment exerted by the liquid on the tank

The pressure can be expressed using Bernoulli's equation (59) after substituting Φ from (70) and x from (20):

$$p = -\varrho\cos\vartheta \sum_{m=1}^{\infty} \frac{dT_{1m}}{dt} J_1\left(\lambda_{1m}\frac{r}{R}\right) \cosh\left(\lambda_{1m}\frac{z}{R}\right) + g\rho(H - z) - a_o(t)\rho r\cos\vartheta. \tag{73}$$

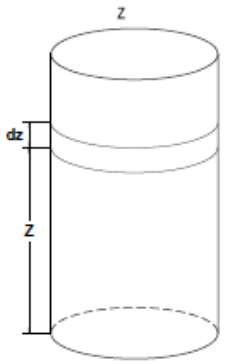

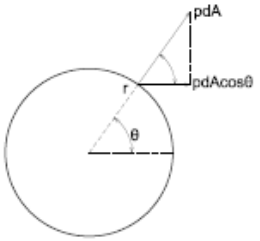

For $r = R$ in (73) we obtain the pressure against the tank walls:

$$p = -\varrho \cos\vartheta \sum_{m=1}^{\infty} \frac{dT_{1m}}{dt} J_1(\lambda_{1m}) \cosh\left(\lambda_{1m}\frac{z}{R}\right) + g\rho(H-z) - a_o(t)\rho R\cos\vartheta. \tag{74}$$

We consider a small element of the cylindrical wall of width dz at a height z from the base (see Figure 27). As shown, the area is $dA = Rd\vartheta dz$ and the force along the x-axis acting on the element is $pdA\cos\vartheta$. Hence, the total force in the x direction can be obtained by computing the integral

$$F_x = \int_{z=0}^{H}\int_{\vartheta=0}^{2\pi} pR\cos\vartheta d\vartheta dz \tag{75}$$

or

$$F_x = -\varrho R\sum_{m=1}^{\infty} \frac{dT_{1m}}{dt} J_1(\lambda_{1m}) \int_{z=0}^{H}\int_{\vartheta=0}^{2\pi} \cos^2\vartheta \cosh\left(\lambda_{1m}\frac{z}{R}\right) d\vartheta dz + g\rho R\int_{z=0}^{H}\int_{\vartheta=0}^{2\pi}(H-z)\cos\vartheta d\vartheta dz - \varrho a_o(t)R^2\int_{z=0}^{H}\int_{\vartheta=0}^{2\pi}\cos^2\vartheta d\vartheta dz. \tag{76}$$

The integrations in (76) are elementary and the result is:

$$F_x = -m_l a_O(t) - \frac{m_l}{H}\sum_{m=1}^{\infty}\frac{J_1(\lambda_{1m})}{\lambda_{1m}}\sinh\left(\lambda_{1m}\frac{H}{R}\right)\frac{dT_{1m}}{dt}, \tag{77}$$

where m_l is the liquid mass. To calculate the total force acting in the y direction we return to the remark made in the lines following (74)

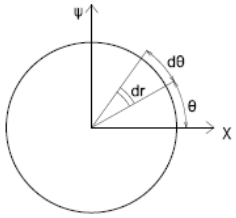

and note that the force along the y- axis acting on the surface element is $pdA\sin\vartheta$, hence the total force acting in the y direction is (compare with (75))

$$F_y = \int_{z=0}^{H}\int_{\vartheta=0}^{2\pi} pR\sin\vartheta d\vartheta dz. \tag{78}$$

We now see from expression (74) that the angular integration in (78) gives zero:

$$F_y = 0. \tag{79}$$

The bending moment immediately above the tank bottom (which includes only the contributions of pressures on the walls) can be easily calculated through the integral

$$M_y = \int_0^H \int_0^{2\pi} pR\cos\vartheta z d\vartheta dz \tag{80}$$

to give:

$$\begin{aligned} M_y = &-m_l\frac{H}{2}a_O(t) - m_l\sum_{m=1}^{\infty}\frac{dT_{1m}}{dt}\frac{J_1\left(\lambda_{1m}\right)}{\lambda_{1m}^2} \\ &\times\left(\sinh\left(\frac{\lambda_{1m}H}{R}\right)\lambda_{1m} - \cosh\left(\frac{\lambda_{1m}H}{R}\right)\frac{R}{H} + \frac{R}{H}\right). \end{aligned} \tag{81}$$

From (81) we see that the d' Alembert force provides a moment as if the force is exerted at the center of mass of the liquid at equilibrium. The pressure on the tank base is obtained by setting $z = 0$ in equation (73):

$$p = -\varrho\sum_{m=1}^{\infty}\frac{dT_{1m}}{dt}\cos\vartheta J_1\left(\lambda_{1m}\frac{r}{R}\right) + g\rho H - a_o(t)\rho r\cos\vartheta. \tag{82}$$

In Figure 28 we consider a small element of the tank base of area $dA = rd\vartheta dr$. The force acting on each element of the base is $dF = prd\vartheta dr$, and generates a moment about the Oy axis given by the integral:

$$M_{base,y} = \int_{r=0}^{R}\int_{\vartheta=0}^{2\pi} r\cos\vartheta prd\vartheta dr, \tag{83}$$

where $r\cos\vartheta$ is the lever-arm of the force dF. Equation (83) gives

$$M_{base,y} = -\varrho \sum_{m=1}^{\infty} \frac{dT_{1m}}{dt} \int_{r=0}^{R} \int_{\vartheta=0}^{2\pi} r^2 \cos^2\vartheta J_1\left(\lambda_{1m}\frac{r}{R}\right) d\vartheta dr \qquad (84)$$
$$-\varrho a_o(t) \int_{r=0}^{R} \int_{\vartheta=0}^{2\pi} r^3 \cos^2\vartheta d\vartheta dr.$$

Using equation (176) of Appendix C to calculate the integral

$$\int_{r=0}^{R} r^2 J_1\left(\lambda_{1m}\frac{r}{R}\right) dr \qquad (85)$$

we have

$$M_{above\ base,y} = -a_o(t) m_l \frac{R^2}{4H} - m_l \frac{R}{H} \sum_{m=1}^{\infty} \frac{J_1(\lambda_{1m})}{\lambda_{1m}^2} \frac{dT_{1m}}{dt}. \qquad (86)$$

In order to check the tank against overturning, one would have to calculate the moment just below the bottom plate of the tank, $M_{below\ base,y}$. This includes the bending moment exerted on the tank walls and the moment due to the pressures acting on the base plate:

$$M_{below\ base,y} = -m_l \left(\frac{H}{2} + \frac{R^2}{4H}\right) a_O(t) \qquad (87)$$
$$-m_l \sum_{m=1}^{\infty} \frac{dT_{1m}}{dt} \frac{J_1(\lambda_{1m})}{\lambda_{1m}^2} \left(\sinh\left(\frac{\lambda_{1m}H}{R}\right)\lambda_{1m} - \cosh\left(\frac{\lambda_{1m}H}{R}\right)\frac{R}{H} + 2\frac{R}{H}\right).$$

3.7 The tank under a lateral sinusoidal excitation

3.7.1 Generalities

We consider the case of a ground acceleration of the form

$$a_O(t) = A\cos\Omega t. \qquad (88)$$

Equation (68) is then written

$$\frac{d^2T_{1m}}{dt^2} + \omega_{1m}^2 T_{1m} - A\Omega\zeta_m \sin\Omega t = 0. \qquad (89)$$

The solution of the above differential equation for the initial conditions $T_{1m}(0) = 0$ and $\frac{dT_{1m}}{dt}(0) = 0$ is

$$T_{1m}(t) = \frac{A\Omega\zeta_m}{\omega_{1m}^2 - \Omega^2}\left(\sin\Omega t - \frac{\Omega}{\omega_{1m}}\sin\omega_{1m}t\right). \qquad (90)$$

3.7.2 Expressions for pressure, force, and moment

We substitute T_{1m} in (73) and get the expression for the pressure:

$$p = -\varrho A\Omega^2 \cos\vartheta \sum_{m=1}^{\infty} \zeta_m \cosh\left(\lambda_{1m}\frac{z}{R}\right) J_1\left(\lambda_{1m}\frac{r}{R}\right) \frac{1}{\omega_{1m}^2 - \Omega^2} \left(\cos\Omega t - \cos\omega_{1m} t\right) + g\rho(H - z) - \rho r A \cos\vartheta \cos\Omega t. \tag{91}$$

Expression (77) for the force combines with (90) to give

$$F_x = -m_l A\cos\Omega t - m_l \frac{2RA\Omega^2}{H} \sum_{m=1}^{\infty} \frac{\tanh\left(\lambda_{1m}\frac{H}{R}\right)}{\lambda_{1m}\left(\lambda_{1m}^2 - 1\right)} \frac{1}{\omega_{1m}^2 - \Omega^2} \left(\cos\Omega t - \cos\omega_{1m} t\right). \tag{92}$$

In a model that includes viscosity the terms proportional to $\cos\omega_{1m} t$ will represent *transient* oscillations and will be damped. To obtain the expression for the bending moment immediately above the base of the tank we substitute (90) in (81):

$$\begin{aligned} M_{above\ base,y} = &-m_l \frac{H}{2} a_O(t) \\ &- m_l 2RA\Omega^2 \sum_{m=1}^{\infty} \frac{\tanh\left(\lambda_{1m}\frac{H}{R}\right)}{\lambda_{1m}(\lambda_{1m}^2 - 1)} \frac{1}{\omega_{1m}^2 - \Omega^2} \\ &\times \left(1 + \frac{1 - \cosh\left(\lambda_{1m}\frac{H}{R}\right)}{\lambda_{1m}\frac{H}{R}\sinh\left(\lambda_{1m}\frac{H}{R}\right)}\right) \left(\cos\Omega t - \cos\omega_{1m} t\right), \end{aligned} \tag{93}$$

which agrees with (130).

3.7.3 The height of the wave

We use (88) and (90) in general expression (72) to obtain

$$\xi = -2\frac{A}{g} R\cos\vartheta \sum_{m=1}^{\infty} \frac{J_1\left(\lambda_{1m}\frac{r}{R}\right)}{(\lambda_{1m}^2 - 1) J_1(\lambda_{1m})} \frac{\Omega^2}{\omega_{1m}^2 - \Omega^2} \left(\cos\Omega t - \cos\omega_{1m} t\right) - \frac{A}{g} r\cos\vartheta\cos\Omega t. \tag{94}$$

3.8 The response of the tank under an arbitrary lateral excitation

3.8.1 The differential equation

One of the aims of the present chapter is to examine the response of the tank under ground motion dictated either by a pulse of known mathematical form or by a seismic signal. In both cases the ground acceleration

$a_O(t)$ either vanishes before a certain time t_0 or, as in the case of the Gabor pulse, is exponentially small as $t \to 0$. In the second case we shall again choose an initial time t_0 at which the ground acceleration is small enough for all practical purposes. Differential equation (68) describes (for each m) a forced harmonic oscillator. It is convenient to introduce new quantities G_m having units of length defined by

$$G_m \equiv \frac{T_{1m}}{\omega_{1m}\zeta_m}. \tag{95}$$

Then equation (68) reads

$$\ddot{G}_m + \omega_{1m}^2 G_m + \frac{1}{\omega_{1m}}\dot{a}_O(t) = 0. \tag{96}$$

Once T_{1m} are calculated either analytically or numerically the behaviour of the system is completely known. For example the velocity potential is calculated through (70), the height of the wave through (72), and pressure, force and moment through (73), (77), and (128) respectively. To specify the boundary conditions that accompany (96) we note that at time $t = t_0$ the velocity of the wave must vanish and hence, according to (62), T_{1m} must vanish. Thus from (95):

$$G_m(t_0) = 0. \tag{97}$$

Similarly pressure, force and moment must vanish at $t = t_0$ and according to (73), (77) and (95), and (128):

$$\dot{G}_m(t_0) = 0. \tag{98}$$

3.8.2 Solution via the Duhamel integral

The solution of (96) subject to boundary conditions (97) and (98) is given by the well-known Duhamel integral (see e. g. Chopra (2007)):

$$G_m(t) = -\frac{1}{\omega_{1m}^2}\int_{t_0}^{t} d\tau \frac{da_O(\tau)}{d\tau}\sin\left(\omega_{1m}\left(t-\tau\right)\right). \tag{99}$$

We integrate (99) by parts:

$$G_m(t) = -\frac{1}{\omega_{1m}^2}\left[a_O(\tau)\sin\left(\omega_{1m}\left(t-\tau\right)\right)\right]_{\tau=t_0}^{\tau=t} + \frac{1}{\omega_{1m}^2}\int_{t_0}^{t} d\tau a_O(\tau)\frac{d}{d\tau}\sin\left(\omega_{1m}\left(t-\tau\right)\right). \tag{100}$$

The first term vanishes for $\tau = t$ and we obtain:

$$G_m(t) = \frac{1}{\omega_{1m}^2}a_O\left(t_0\right)\sin\left(\omega_{1m}\left(t-t_0\right)\right) - \frac{1}{\omega_{1m}}\int_{t_0}^{t} d\tau a_O(\tau)\cos\left(\omega_{1m}\left(t-\tau\right)\right). \tag{101}$$

Pressure, force and moment depend on dT_{1m}/dt and to obtain an expression for the latter we differentiate (101) with respect to t:

$$\dot{G}_m(t) = \frac{1}{\omega_{1m}} a_O(t_0) \cos(\omega_{1m}(t-t_0)) - \frac{1}{\omega_{1m}} a_O(t) + \int_{t_0}^{t} d\tau a_O(\tau) \sin(\omega_{1m}(t-\tau)). \tag{102}$$

Note that the above derivation assumes that the function $a_O(t)$ does not have any Heaviside-type discontinuities for $t > t_0$, else (102) contains further terms resulting from the integration by parts. If $a_O(t)$ does not have a Heaviside-type discontinuity at $t = t_0$, i. e. if $a_O(t_0) = 0$, then the first term in (102) is absent. In what follows we shall assume that this is always the case:

$$a_O(t_0) = 0. \tag{103}$$

Then

$$\dot{G}_m(t) = -\frac{1}{\omega_{1m}} a_O(t) + \int_{t_0}^{t} d\tau a_O(\tau) \sin(\omega_{1m}(t-\tau)). \tag{104}$$

3.8.3 Solution via the Fourier transformation

Notation: In what follows given a function $y(t)$ we denote by $\hat{}$ its Fourier transform

$$\hat{y}(\omega) = \int_{-\infty}^{+\infty} e^{-i\omega t} y(t) dt. \tag{105}$$

The technicalities of the Fourier transform are easier in the case of an oscillator with damping. In the present problem damping comes about as a result of viscosity as well as of friction between liquid and walls. These factors have been neglected in the hydrodynamical treatment; however damping can be put in by hand in (96) by writing it in the form (see e.g. Meirovitch (2001))

$$\ddot{G}_m + 2\eta_m \omega_{1m} \dot{G}_m + \omega_{1m}^2 G_m + \frac{1}{\omega_{1m}} \dot{a}_O(t) = 0. \tag{106}$$

We use the notation η_m since in a proper hydrodynamical treatment each mode may well have its own damping factor. However in a following subsection where we will consider accelerograms we shall take $\eta_m = 0.005$ for all modes.

We first look for solutions $g_m(t)$ that satisfy (106) but not the boundary conditions (97) and (98). According to the standard theory (see Chopra (2007) and Meirovitch (2001)) the response $g_m(t)$ under damping is

$$g_m(t) = -\frac{1}{2\pi\omega_{1m}} \int_{-\infty}^{+\infty} e^{i\omega t} \frac{\widehat{\dot{a}}_O(\omega)}{-\omega^2 + \omega_{1m}^2 + i2\eta_m \omega_{1m} \omega} d\omega, \tag{107}$$

and the integral, if $\widehat{\dot{a}}_O(\omega)$ is simple enough, can be evaluated exactly. In a following subsection the integral (107) will be evaluated via the FFT.

We use the well-known property (see Boggess and Narcowich (2009))

$$\widehat{\dot{a}}_O(\omega) = i\omega \hat{a}_O(\omega)$$

to obtain

$$g_m(t) = -\frac{i}{2\pi\omega_{1m}} \int_{-\infty}^{+\infty} e^{i\omega t} \frac{\omega}{-\omega^2 + \omega_{1m}^2 + i2\eta_m\omega_{1m}\omega} \hat{a}_O(\omega) d\omega \tag{108}$$

as one solution of (106). From the above we obtain

$$\dot{g}_m(t) = \frac{1}{2\pi\omega_{1m}} \int_{-\infty}^{+\infty} e^{i\omega t} \frac{\omega^2}{-\omega^2 + \omega_{1m}^2 + i2\eta_m\omega_{1m}\omega} \hat{a}_O(\omega) d\omega. \tag{109}$$

We now turn to the initial conditions and note that equations (108) and (109) determine the values $g_m(0)$, $\dot{g}_m(0)$. The requisite solutions $G_m(t)$ are obtained if to $g_m(t)$ we add solutions of the homogeneous differential equations:

$$\begin{aligned} G_m(t) = g_m(t) + A_m e^{-\eta_m\omega_{1m}t} \cos\left(\omega_{1m}\sqrt{1-\eta_m^2}t\right) \\ + B_m e^{-\eta_m\omega_{1m}t} \sin\left(\omega_{1m}\sqrt{1-\eta_m^2}t\right). \end{aligned} \tag{110}$$

In the present case of small η_m we may neglect the square roots in (110) and write

$$G_m(t) = g_m(t) + A_m e^{-\eta_m\omega_{1m}t} \cos\omega_{1m}t + B_m e^{-\eta_m\omega_{1m}t} \sin\omega_{1m}t. \tag{111}$$

The last two terms in (111) are called *transients* since they die away at large times. Initial condition (97) gives

$$A_m = -g_m(0). \tag{112}$$

Differentiating (111) we obtain

$$\begin{aligned} \dot{G}_m(t) = \dot{g}_m(t) - (A_m + B_m\eta_m)\,\omega_{1m} e^{-\eta_m\omega_{1m}t} \sin\omega_{1m}t + \\ (B_m - A_m\eta_m)\,\omega_{1m} e^{-\eta_m\omega_{1m}t} \cos\omega_{1m}t. \end{aligned} \tag{113}$$

Applying initial condition (98) in (113) we obtain

$$B_m = -\frac{\dot{g}_m(0)}{\omega_{1m}} - g_m(0)\eta_m. \tag{114}$$

Thus the final expressions for $G_m(t), \dot{G}_m(t)$ are:

$$G_m(t) = g_m(t) - g_m(0)e^{-\eta_m\omega_{1m}t}\cos\omega_{1m}t - \left(\frac{\dot{g}_m(0)}{\omega_{1m}} + g_m(0)\eta_m\right)e^{-\eta_m\omega_{1m}t}\sin\omega_{1m}t, \tag{115}$$

$$\dot{G}_m(t) = \dot{g}_m(t) + \left(g_m(0) + \frac{\dot{g}_m(0)\eta_m}{\omega_{1m}}\right)\omega_m e^{-\eta_m\omega_m t}\sin\omega_{1m}t - \dot{g}_m(0)e^{-\eta_m\omega_{1m}t}\cos\omega_{1m}t, \tag{116}$$

where we neglected a term proportional to η_m^2.

Another way to express the above results for $G_m(t), \dot{G}_m(t)$ is as follows. We rewrite (109) in the form

$$\dot{g}_m(t) = -\frac{1}{2\pi\omega_{1m}}\int_{-\infty}^{+\infty} e^{i\omega t}\left(1 - \frac{\omega_{1m}^2}{-\omega^2 + \omega_{1m}^2 + i2\eta_m\omega_{1m}\omega}\right)\hat{a}_O(\omega)d\omega, \tag{117}$$

and use the inverse Fourier transform in the first term together with the abbreviation

$$l_m(t) = \frac{1}{2\pi}\int_{-\infty}^{+\infty} e^{i\omega t}\frac{1}{-\omega^2 + \omega_{1m}^2 + i2\eta_m\omega_{1m}\omega}\hat{a}_O(\omega)d\omega, \tag{118}$$

to obtain

$$\dot{g}_m(t) = -\frac{a_O(t)}{\omega_{1m}} + \omega_{1m}l_m(t). \tag{119}$$

Note that the quantities l_m have dimensions of length and according to (118) describe the response of an harmonic oscillator to a forcing term that coincides with $\hat{a}_O(t)$. In that sense they are identical to the oscillators first introduced by Housner. The separation in (119) essentially amounts to the distinction between impulsive and convective modes and its consequences will be seen in the calculation of the force.

From (119) and (103) we obtain

$$\dot{g}_m(0) = \omega_{1m}l_m(0), \tag{120}$$

hence

$$G_m(t) = g_m(t) - g_m(0)e^{-\eta_m\omega_{1m}t}\cos\omega_{1m}t - \left(l_m(0) + g_m(0)\eta_m\right)e^{-\eta_m\omega_{1m}t}\sin\omega_{1m}t, \tag{121}$$

$$\dot{G}_m(t) = -\frac{a_O(t)}{\omega_{1m}} + \omega_{1m}l_m(t) + \left(g_m(0) + l_m(0)\eta_m\right)\omega_{1m}e^{-\eta_m\omega_{1m}t}\sin\omega_{1m}t - \omega_{1m}l_m(0)e^{-\eta_m\omega_{1m}t}\cos\omega_{1m}t. \tag{122}$$

Equations (115), (116), (121), and (122) are the central results of this subsection.

3.8.4 Calculation of the force

The lateral force is given by the combination of (77) and (95). In terms of $\dot{G}_m(t)$

$$F_x = -m_l a_O(t) - \sum_{m=1}^{\infty} \mu_m \omega_{1m} \dot{G}_m(t), \tag{123}$$

where we introduced

$$\begin{aligned}\mu_m &\equiv \frac{m_l}{H} \frac{J_1(\lambda_{1m})}{\lambda_{1m}} \sinh\left(\lambda_{1m}\frac{H}{R}\right) \zeta_m \\ &= m_l \frac{2R}{H} \tanh\left(\lambda_{1m}\frac{H}{R}\right) \frac{1}{\lambda_{1m}(\lambda_{1m}^2 - 1)}.\end{aligned} \tag{124}$$

We use equation (122) for $\dot{G}_m(t)$ and write

$$F_x(t) = -\mu_0 a_O(t) - \sum_{m=1}^{\infty} \mu_m \omega_{1m}^2 \widetilde{L}_m(t), \tag{125}$$

where μ_0 is defined as the *impulsive* mass,

$$\mu_0 = m_l - \sum_{m=1}^{\infty} \mu_m,$$

and

$$\widetilde{L}_m(t) = l_m(t) + (g_m(0) + l_m(0)\eta_m)\, e^{-\eta_m \omega_{1m} t} \sin \omega_{1m} t - l_m(0) e^{-\eta_m \omega_{1m} t} \cos \omega_{1m} t. \tag{126}$$

The interpretation of (125) justifies the picture advocated by Housner (1957). If the excitation is such that $a_O(t_0) = 0$ then the system behaves as if it consists of an impulsive mass rigidly following the tank and of *convective* masses μ_m connected to springs of constants K_m

$$K_m \equiv \mu_m \omega_{1m}^2, \tag{127}$$

giving rise to elastic forces $F_x^{(m)}$ proportional to stretchings instantaneously given by the Duhamel integrals. Housner's development was based on a simplified model of the fluid. Veletsos in various publications (notably Veletsos and Yang (1977)) further developed this picture starting with the full hydrodynamical model for an inviscid fluid and separating the velocity potential to impulsive and convective components. The dependence of impulsive and convective masses on H/R is given in Figure 29.

The spring analog is further illustrated in Figure 30 where the masses are attached at heights h_m given by (128) so that the moments of the spring forces coincide with the moments given by (130).

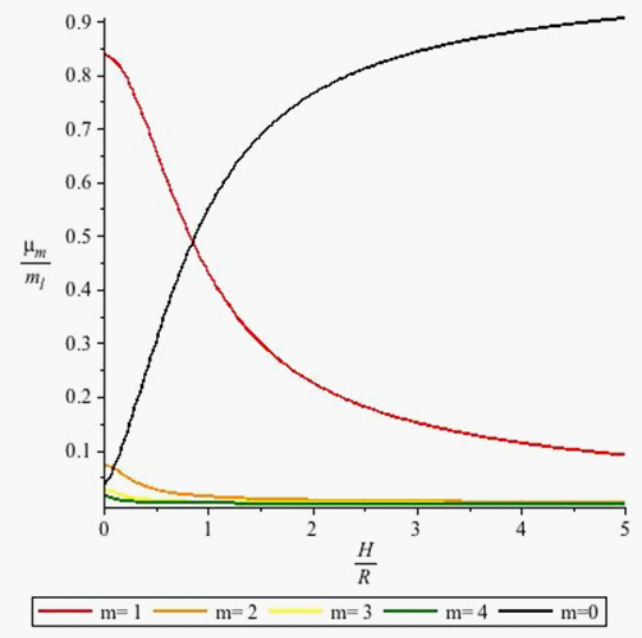

Figure 27: Plot of μ_m/m_l vs H/R

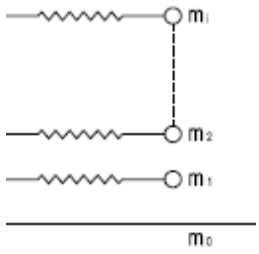

Figure 28: Illustration of the spring-mass analog

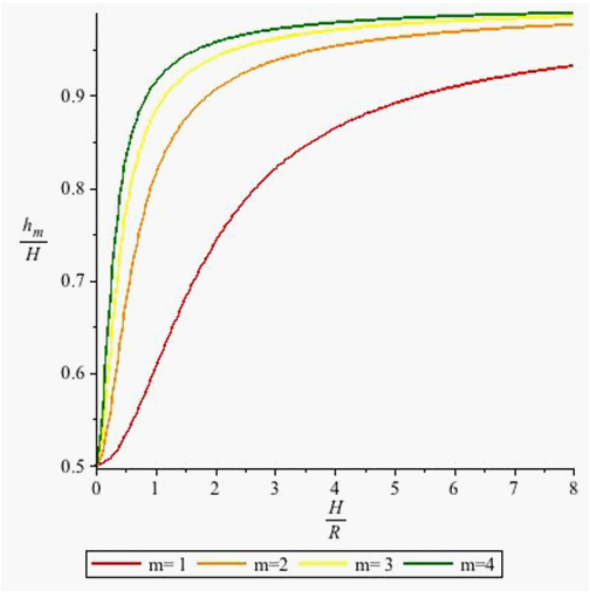

Figure 29: Plot of h_m/H vs H/R

We turn to the calculation of other quantities. In order to calculate the bending moment immediately above the bottom plate of the tank we substitute (122), (95) and (69) into (81) For each mode m we define a constants h_m , h_{imp} via

$$\frac{h_m}{H} = 1 + \frac{1 - \cosh\left(\lambda_{1m}\frac{H}{R}\right)}{\lambda_{1m}\frac{H}{R}\sinh\left(\lambda_{1m}\frac{H}{R}\right)}, \tag{128}$$

and

$$\frac{h_{imp}}{H} = \frac{m_l\frac{H}{2} - \sum_{m=1}^{\infty}\mu_m h_m}{\mu_0} \tag{129}$$

then expression (81) for the bending moment reads

$$M_y(t) = -h_{imp}\mu_0 a_O\left(t\right) - \sum_{m=1}^{\infty} h_m\mu_m\omega_{1m}^2\tilde{L}_m. \tag{130}$$

In other words the force $\mu_m\omega_{1m}^2\tilde{L}_m$ provides a moment as if it is exerted at a height h_m from the base, while the first term gives the *impulsive* contribution. In Figure 11 we plot h_m/H versus H/R for the first four modes. We observe that for a given H/R the value of h_m/H increases as the order of the mode gets higher. This is explained as follows: the presence of the factor $\cosh(\lambda_{1m}z/R)$ in (74) means that the pressure profile concentrates on higher values of z as the order of the mode increases. Similarly we calculate the moment just below the bottom plate of the

tank by substituting (122), (95) and (69) into (87). For each mode m we now define a constant $h_m^{'}$ via

$$\frac{h_m^{'}}{H} = \frac{h_m}{H} + \frac{1}{\lambda_{1m}\frac{H}{R}\sinh\left(\lambda_{1m}\frac{H}{R}\right)}, \tag{131}$$

and then expression (87) for the moment reads

$$M_y^{'} = -\left(m_l\left(\frac{H}{2}+\frac{R^2}{4H}\right) - \sum_{m=1}^{\infty}\mu_m h_m^{'}\right) a_O\left(t\right) + \sum_{m=1}^{\infty} h_m^{\prime}\mu_m\omega_{1m}^2\tilde{L}_m. \tag{132}$$

To obtain the pressure distribution we substitute (122), (95) and (69) into (73)

$$\begin{aligned} p(r,z,\vartheta,t) = a_O\left(t\right)\rho R\cos\vartheta\left(\sum_{m=1}^{\infty} C_m(r,z) - \frac{r}{R}\right) \\ -\rho R\cos\vartheta\sum_{m=1}^{\infty} C_m(r,z)\omega_{1m}^2\widetilde{L}_m(t) + g\rho(H-z), \end{aligned} \tag{133}$$

where we abbreviated

$$\mathcal{C}(r,z) = \sum_{m=1}^{\infty} C_m(r,z) - \frac{r}{R}, \tag{134}$$

$$C_m(r,z) = \frac{2\cosh\left(\lambda_{1m}\frac{z}{R}\right)J_1\left(\lambda_{1m}\frac{r}{R}\right)}{(\lambda_{1m}^2-1)\cosh\left(\lambda_{1m}\frac{H}{R}\right)J_1\left(\lambda_{1m}\right)}. \tag{135}$$

For future use we identify the first, second, and third terms as *impulsive, convective* and *hydrostatic* respectively. In Figure 12 we plot the impulsive pressure on the tank walls (setting $r = R$ in (133)) as a function of z for four different values of H/R. It is important to note that

$$\mathcal{C}(r,H) = 0. \tag{136}$$

This is immediately seen using (134), (135) and (178).

We substitute (122), (95) and (69) in (72) to obtain the displacement of the surface

$$\xi(r,\vartheta,t) = -\frac{1}{g}R\cos\vartheta\sum_{m=1}^{\infty} C_m(r,H)\omega_{1m}^2\widetilde{L}_m(t), \tag{137}$$

where we used (136). Note that *convective components only* contribute to ξ.

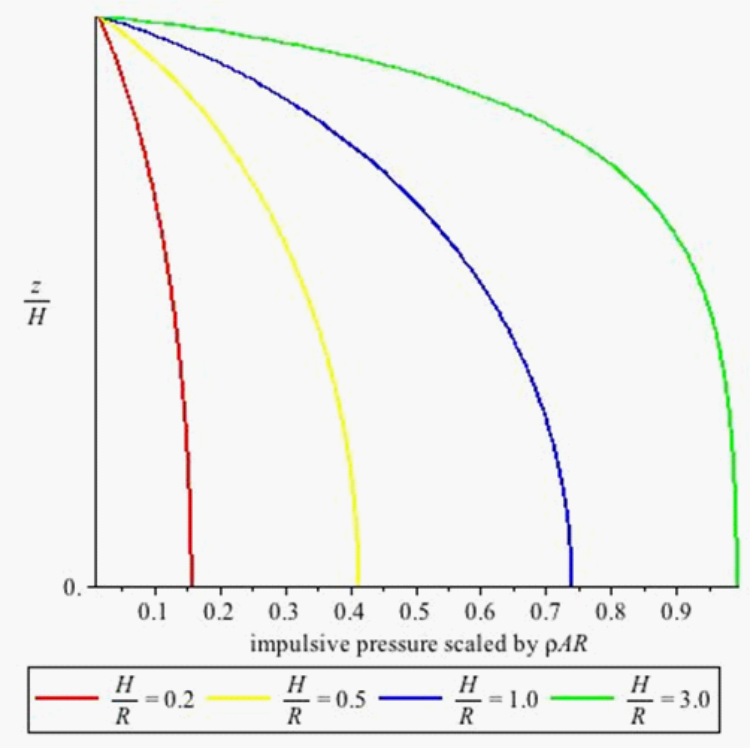

Figure 30: Height vs impulsive pressure on the wall scaled by ρaR. According to (134) this is a plot of $\mathcal{C}(R, z)$.

Before ending this subsection we return to the expression of the force (92) in the case of sinusoidal lateral excitation and express it in terms of impulsive and convective masses:

$$F_x = -\mu_0 A \cos\Omega t - A\sum_{m=1}^{\infty}\mu_m \cos\omega_{1m}t - A\sum_{m=1}^{\infty}\mu_m \frac{\omega_{1m}^2}{\omega_{1m}^2-\Omega^2}\left(\cos\Omega t - \cos\omega_{1m}t\right). \tag{138}$$

3.9 Calculation of the response given the accelerogram: the Discrete Fourier transform (DFT)

To calculate the various dynamical quantities we need $l_m(t)$ and $g_m(0)$ obtainable via the inverse Fourier transforms (118) and (108) respectively. The accelerogram gives the ground acceleration at discrete times and the above mentioned inverse FTs are to be calculated via the Discrete Fourier Transform (DFT method).

The accelerogram $a_O(t')$ extends from an initial time $t'=0$ to some final time which, for example in the case of the Imperial Valley earthquake, equals 39.98 s. Values in this case are given at 0.005 s intervals; this defines the time-step Δt. We thus have a total of 39.98/0.005=7996 intervals and 7997 data points. These data points are stored in a MAPLE `Array`. MAPLE, as is the case with all modern mathematical packages, handles the DFT via the Fast Fourier transform algorithm (FFT). The latter stipulates that the size of an `Array` must equal a power of 2. The total number of data points must be sufficienty large so that the damping reduces the response to a negligible value. (DFT works with periodic signals so take must be taken that the acceleration at $t=0$ as given by the accelerogram indeed vanishes.) In the present case we choose $N=2^{16}=65536$ data points and fill the remaining $65536-7997$ data entries with zeros. We denote by

$$L = N\Delta t \tag{139}$$

the total length of time and then

$$\hat{a}_O(\omega) = \int_{-\infty}^{\infty} dt e^{-i\omega t} a_O(t) = \int_0^L dt e^{-i\omega t} a_O(t). \tag{140}$$

We further approximate the area represented by the integral by a sum of rectangles to obtain

$$\hat{a}_O(\omega) = \int_0^L dt e^{-i\omega t} a_O(t) = \Delta t \sum_{k=1}^{N} a_O(t_k) e^{-i\omega t_k} = \Delta t \sum_{k=1}^{N} a_O(t_k) e^{-i\omega kL/N}, \tag{141}$$

where t_k is the left end-point of each interval:

$$t_k = k\Delta t = kL/N. \tag{142}$$

We further define the discrete angular frequencies

$$\omega_n = 2\pi n/L \quad , \quad n = 1..N, \tag{143}$$

and hence obtain from (141):

$$\hat{a}_O(\omega_n) = \frac{L}{N}\sum_{k=1}^{N} a_O(t_k)e^{-i2\pi nk/N}. \tag{144}$$

DFT guarantees that if $a_O(t_k)$ is a periodic signal then so is $\hat{a}_O(\omega_n)$. The quantity appearing in the above equation **without** the L factor is the FFT of the `Array` $a_O(t_k)$ and is evaluated in MAPLE by typing the `FastFourierTransform` command. The result is given as an array $\hat{a}_O(\omega_n)$.

To calculate $l_m(t)$ we proceed in three steps as follows:

- From the array $a_O(t_k)$ we calculate via FFT the array

$$\frac{1}{N}\sum_{k=1}^{N} a_O(t_k)e^{-i2\pi nk/N}. \tag{145}$$

  The presence of $1/N$ means that we adopt the `FullNormalization` option of the MAPLE package.

- We multiply the above by the transfer function at the discrete points ω_n to obtain the `Array`

$$\hat{l}_m(\omega_n) = -\frac{1}{-\omega_n^2 + \omega_{1m}^2 + 2i\eta_m\omega_n\omega_{1m}}\hat{a}_O(\omega_n). \tag{146}$$

To obtain the discretized version of (118) we approximate it by a sum of rectangles:

$$l_m(t_l) = \frac{\Delta\omega}{2\pi}\sum_{n=1}^{N}\hat{l}_m(\omega_n)e^{i\omega_n t_l} = \frac{1}{L}\sum_{n=1}^{N}\hat{l}_m(\omega_n)e^{i2\pi nl/N}. \tag{147}$$

The right hand side of the above equation **without** the $1/L$ factor is the inverse DFT of $\hat{l}_m(\omega_n)$. Note that the L factors in (144) and (147) cancel out. Hence the third step:

- Through `InverseFourierTransform` we evaluate the inverse DFT of $\hat{l}_m(\omega_n)$ to arrive at the response function $l_m(t_l)$ evaluated at discrete times.

In a similar manner we calculate $g_m(t)$:

- We use the quantity (145).
- We multiply by the transfer function to obtain the array

$$-\frac{i}{\omega_{1m}}\frac{\omega_n}{-\omega_n^2+\omega_{1m}^2+2i\eta_m\omega_n\omega_{1m}}\hat{a}_O(\omega_n) \tag{148}$$

- Through inverse DFT we calculate $g_m(t_l)$.

  Using expression (126) we obtain $\tilde{L}_m$, through which we can calculate all quantities of interest.

4 Comparison with codes

4.1 Introduction

In this section we will discuss how current design guidelines treat the problem of liquid-containing tanks subject to earthquake motion. A rigorous analysis of the seismic response of tanks should include the hydrodynamic pressures on the tank wall and base, the liquid-shell interaction, the deformation of the tank walls and the deformability of the foundation soil, and the modification of the response due to soil-structure interaction. The complexity of this problem requires high computational and analytical effort. The seismic codes propose several analysis procedures, valid for specific design situations. The treatment of the several aspects that should be taken into account may vary among the existing design codes, while some codes deal with only specific types of tanks. Although the general features regarding the calculation of the design forces are maintained, the policies they employ may vary, thus leading to notably different results in some cases.

In this section we will concentrate on the treatment of the hydrodynamic response of rigid vertical circular tanks on-ground, fixed to the foundation. Special emphasis will be given to the procedure analysis proposed by Eurocode 8 (EC8), Earthquake Resistant Design of Structures, Part 4: Tanks, Silos and Pipelines (1).

4.2 Results and discussion

The model used for the seismic analysis of liquid storage tanks should be able to accurately reproduce the stiffness, the strength, the damping and the geometrical properties of the structure, and account for the hydrodynamic response of the contained liquid, and, if relevant, for the effects of the interaction with the foundation soil. Eurocode 8 and the other widely used codes such as ACI 350.3, AWWA standards, API 650 (USA), NZSEE (New Zealand) refer to the spring-mass analog introduced in Subsection 2.8 and the subsequent separation to impulsive and convective modes.

According to the review by Jaiswal, Rai and Jain (2007), Eurocode 8 and NZSEE guidelines use the hydrodynamical model of Veletsos and Yang (1977) and ACI 350.3, AWWA standards and API 650 use the mechanical model of Housner (1963) with modifications of Wozniak and Mitchell (1978). The derivation of the mechanical spring-mass analogue used in Eurocode 8 is explained in Subsection 2.8. Tanks are generally analysed using linear elastic response. Eurocode 8 allows for the use of 'modal response spectrum' analysis and for the use of dynamic time history analysis in order to evaluate the design forces referring to the tank.

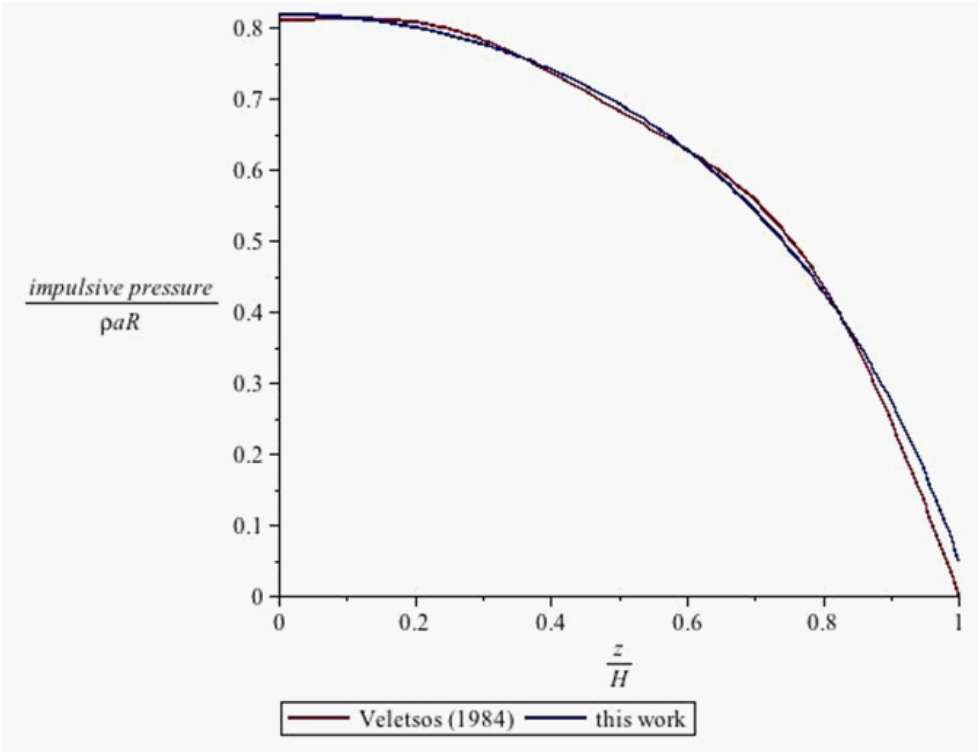

Concerning damping, we note: (i) structural damping in the ultimate limit state: 5%, (ii) contents damping: 0.5 % (for water and other liquids). Eurocode 8 suggests the following procedure as a general method of analysis.

The first step is to calculate the impulsive pressure under a given ground acceleration time history, $A_g(t)$. In our case the impulsive pressure is given by the first term in eqn (133) with the coefficients $C_m(r,z)$ being given by equation (135). Eurocode gives the impulsive pressure in the form

$$p_i(\xi,\varsigma,\vartheta,t) = C_i(\xi,\varsigma)\rho H\cos\vartheta A_g(t), \tag{149}$$

where ξ,ς are the nondimensional coordinates $\xi = r/R, \varsigma = z/H$ respectively, and $C_i(\xi,\varsigma)$ is a coefficient introduced by Veletsos (1984):

$$C_i(\xi,\varsigma) = 2\sum_{n=0}^{\infty}\frac{(-1)^n}{I_1'(\nu_n/\gamma)\,\nu_n^2}\cos(\nu_n\varsigma)\,I_1\left(\frac{\nu_n}{\gamma}\xi\right), \tag{150}$$

in which $\nu_n = \frac{2n+1}{2}\pi$, $\gamma = H/R$, I_1 and I_1' denote the modified Bessel function of first order and its derivative. In Figure 33 we show that our expression is equivalent to Veletsos to a very good approximation (the two results are identical if one sums an infinite number of modes).

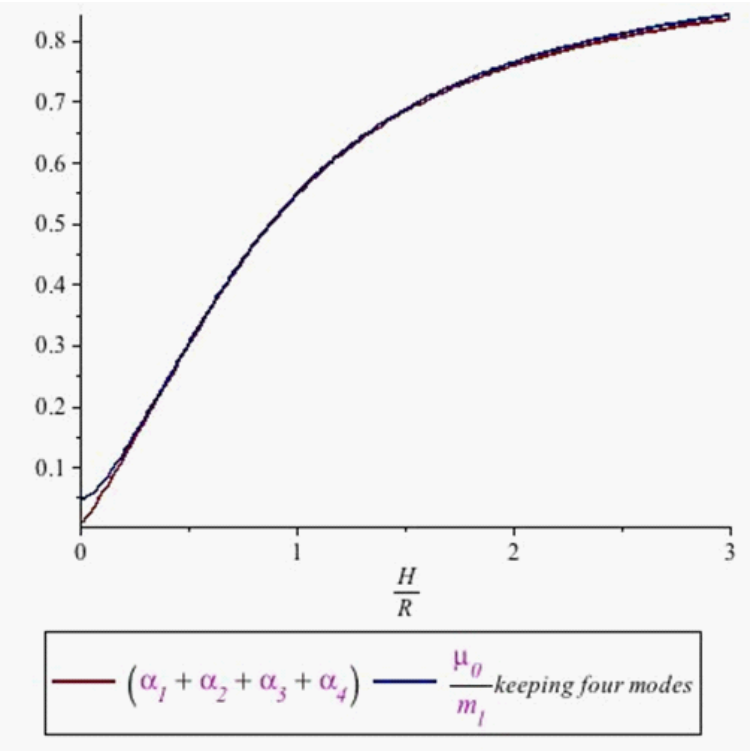

The variation of the pressure with depth is given in Figure 33. The impulsive base shear is given by

$$Q_i(t) = m_i A_g(t),$$

where m_i is the impulsive mass, which in the case of Veletsos (1984) is given by

$$m_i = m2\gamma \sum_{n=0}^{\infty} \frac{I_1(\nu_n/\gamma)}{I_1'(\nu_n/\gamma)\,\nu_n^3} \tag{151}$$

where $m = \varrho\pi R^2 H$ us the total contained mass of the fluid. Agreement is shown in Figure 33. Concerning the impulsive force, see also remark following equation (157).

'Regarding the moment, Eurocode makes a distinction between the moment immediately above the bottom plate of the tank (denoted by M_i), and the moment immediately below the bottom plate of the tank (denoted by M_i'). Eurocode stipulates that the former should be used for the calculation of the stresses and stress resultants in the tank walls and at the connection to the base, while the later should be used for stability against overturning.

$$M_i'(t) = m_i h_i' A_g(t), \tag{152}$$

where

$$h_i^{'} = H \frac{\frac{1}{2} + 2\gamma \sum_{n=0}^{\infty} \frac{\nu_n + 2(-1)^{n+1} I_1(\nu_n/\gamma)}{I_1'(\nu_n/\gamma)\nu_n^4}}{2\gamma \sum_{n=0}^{\infty} \frac{I_1(\nu_n/\gamma)}{I_1'(\nu_n/\gamma)\nu_n^3}} \tag{153}$$

and

$$M_i(t) = m_i h_i A_g(t), \tag{154}$$

where

$$h_i = H \frac{\sum_{n=0}^{\infty} \frac{(-1)^n I_1(\nu_n/\gamma)}{I_1'(\nu_n/\gamma)\nu_n^4} \left(\nu_n(-1)^n - 1\right)}{\sum_{n=0}^{\infty} \frac{I_1(\nu_n/\gamma)}{I_1'(\nu_n/\gamma)\nu_n^3}}. \tag{155}$$

Concerning our calculation of the moment see remark following equation (158).

The next step is the calculation of the convective pressure, base shear, and moment components. The expression for the convective pressure is

$$p_c(\xi, \varsigma, \vartheta, t) = \rho \sum_{n=1}^{\infty} \psi_n \cosh(\lambda_n \gamma \varsigma) J_1(\lambda_n \xi) \cos\vartheta A_{cn}(t), \tag{156}$$

where

$$\psi_n = \frac{2R}{\left(\lambda_n^2 - 1\right) J_1(\lambda_n) \cosh(\lambda_n \gamma)}. \tag{157}$$

Expression (156) exactly coincides with the second term of our (**??**). Note that our results for the convective and impulsive forces are formulated in terms of convective masses m_m only, and there is no need to calculate the coefficients appearing in (151) (denoted by a_i in Veletsos (1984)). $A_{cn}(t)$ in (156) represents the response acceleration of an oscillator of angular frequency ω_{cn} (given by (35) and plotted in Figure 34 afainst H/R) subject to an external excitation). Eurocode asserts that only the first sloshing mode needs to be taken into account for design purposes and one of the objectives of this thesis is to verify this assertion. The convective base shear is calculated through

$$Q_c(t) = \sum_{n=1}^{\infty} m_{cn} A_{cn}(t),$$

where m_{cn} is the nth modal convective mass coinciding with our result (**??**). The moment in the tank wall immediately below the bottom plate of the tank is

$$M_c'(t) = \sum_{n=1}^{\infty} m_{cn} A_{cn}(t) h_{cn}^{'} = \sum_{n=1}^{\infty} Q_{cn}(t) h_{cn}^{'},$$

where

$$h_{cn}^{'} = H\left(1 + \frac{2 - \cosh(\lambda_n \gamma)}{\lambda_n \gamma \sinh(\lambda_n \gamma)}\right)$$

and the moment in the tank wall immediately above the bottom plate of the tank is

$$M_c(t) = \sum_{n=1}^{\infty} m_{cn} A_{cn}(t) h_{cn} = \sum_{n=1}^{\infty} Q_{cn}(t) h_{cn}, \tag{158}$$

where h_{cn} coincides with our expression (128). The Eurocode expressions for impulsive and convective moments coincide with the first and second terms of our (**??**) respectively. Note that our results are expressed in terms of h_m and m_m and there is no need to calculate the complicated summation (155). The estimation of the necessary freeboard is based on the height of the sloshing wave. The Eurocode assumes that the dominant contribution comes from the first mode, whose maximum, in accordance with the remarks preceding (39), occurs at the wall:

$$d_{\max} = 0.84 R S_e(T_{c1})/g,$$

which is obtained from Veletsos' (1984) equation (C-37) for $r = R$. $S_e(T_{c1})$ is the elastic response spectral acceleration at the 1st convective mode.

The contribution of the second mode is examined in a following section.

In the calculation of the total force, pressure and moment the inertia of the tank walls must be taken into account (which is negligible in the case of steel tanks but not so in the case of concrete tanks). The behaviour factor used for the calculation of the design forces differs for the impulsive and convective components. The convective response is not associated with energy dissipation, whereas the hysteretic energy dissipation that may accompany the impulsive and inertia components is expressed through the use modification of the elastic response spectrum by the behaviour factor q that may be equal to or higher than 1.5 (whereas q=1 must be used for the convective design forces). According to the above procedure, the total design forces are obtained through the

addition of the convective first mode time-history and impulsive time-history (including the inertia components). When the response spectrum approach is used instead, Eurocode, together with ASCE 7 suggests that the calculation of the maximum dynamic response is obtained through the use of absolute summation rule. Other codes such as ACI 350.3, D-110, D-115, API 650 and NZSEE use the SRSS rule.

5 Application to the analysis of near-fault phenomena

5.1 Introduction

Liquid storage tanks fall in the class of structures (together with high-rise buildings and suspension bridges) with large fundamental period. For example for a tank of radius $R = 10$ m and $H = 25$ m the period of the first ($m = 1$) mode is 4.67 seconds (according to equation (36)). It is thus of interest to consider excitations with long-period components. Long-period ground motion can be generated by far-source large crustal earthquakes through the help of path effects, or by near-fault earthquakes through forward rupture directivity and fling-step effects (Koketsu & Miyake (2008), Shuang and Li-li (2007)). A description of the above mechanisms and details on their mathematical modelling can be found in Dabaghi & Der Kiureghian (2014). In fact, in the abscence of seismograms, long-period ground motions can be identified through the damaged caused to tanks by liquid sloshing. An example of near-fault long-period ground motion is provided by the 1979 Imperial Valley earthquake, whose impact on liquid storage tanks are detailed in section 2; the response of tanks of various H/R ratios shall be examined later on in this chapter using the formalism developed in section 3.

A characteristic of near-fault ground motions is the presense of one or more pulse-type wave shapes in the velocity (or less often in the acceleration and displacement) time-history, high ratio of peak ground velocity to peak ground, acceleration (v_{PG}/a_{PG}), and sometimes large permanent ground displacements generated by the directivity. In this section we will examine the behaviour of tanks of four different H/R ratios (0.3, 0.5, 1.0, 2.5) in near-fault phenomena by applying time-history analysis in (a) synthetic wavelets and (b) original accelograms. These results will be compared with results of analyses for three far-fault accelerograms.

5.2 Pulses

An insight in the response of a structure modelled as a set of oscillators may be obtained by using synthetic wavelets that involve a minimum number of input parameters while at the same time allow enough flexibility to represent reasonably accurately near-source pulses. The Gabor wavelet has been used in this context and consists of a harmonic oscillation enveloped by a Gaussian (bell-shaped) function. The Gabor wavelet is defined by four parameters: the amplitude $\mathcal{A}$, the prevailing angular frequency ω_p, a constant γ that characterizes the decay rate (big γ means slow decay), and a constant n that characterizes the overall phase. The

latter shall be taken as zero in what follows. Thus under a Gabor pulse the ground velocity is given by

$$v_O(t) = \mathcal{A} \exp\left(-\frac{\omega_p^2 t^2}{\gamma^2}\right) \cos\left(\omega_p t\right). \tag{159}$$

The Gabor pulse is discussed in and an alternative is offered by Mavroeidis and Papageorgiou (2003). Their pulse has the form

$$v_O(t) = \frac{\mathcal{A}}{2}\left(1 + \cos\left(\frac{\omega_p}{\gamma}\left(t - \tilde{t}\right)\right)\right) \cos\left(\omega_p\left(t - \tilde{t}\right) + n\right), \tag{160}$$

where $\mathcal{A}$, ω_p, and γ have the same physical meaning as in the Gabor pulse, $\tilde{t}$ the time at which the enveloping function attains its maximum, and n the phase of the amplitude-modulated harmonic. Note however that the Mavroeidis-Papageorgiou (MP) pulse has no exponential to force its decrease so one has to stipulate when the pulse is switched on and off. Mthematically this is easily taken care of by mulpipyingby a Heaviside function. The pulse is taken to exist for times

$$\tilde{t} - \frac{\pi\gamma}{\omega_p} \leq t \leq \tilde{t} + \frac{\pi\gamma}{\omega_p}. \tag{161}$$

The ground acceleration is obtained by differentiating (160) with respect to time:

$$a_O(t) = -\frac{\mathcal{A}}{2}\omega_p\left(\frac{1}{\gamma}\sin\left(\frac{\omega_p}{\gamma}t\right)\cos\omega_p t + \left(1 + \cos\left(\frac{\omega_p}{\gamma}t\right)\right)\sin\omega_p t\right). \tag{162}$$

We are interested in the contribution of the second mode whose angular frequency, for values H/R between 0.2 and 3.0, varies from 2.029 to 2.286 (according to (35)). From Table 3 of MP we see that the Imperial Valley (Station EMO-SN component), Northridge (Station JFA- SN component) and Erzincan (Station ERZ- SN component) earthquakes provide resonance near these values, while their magnitude is between 6.5 and 6.7 Mw hence making them relevant to greek reality. We consider pulses with parameters $\mathcal{A}$, ω_p, γ, n and $\tilde{t}$ as suggested by MP to simulate the above earthquakes.

For the Imperial Valley earthquake we use $A = 78cm/\sec, \gamma = 2.3, n = 0.0, \omega_p = 2.136, \tilde{t} = 4.95$.We apply (161) and obtain

$$1.57 \leq t \leq 8.32 \tag{163}$$

Figures 35 and 36 show the velocity and acceleration pulses respectively. According to (162) $a_O(t_0) = 0$ and the first term in (102) vanishes.

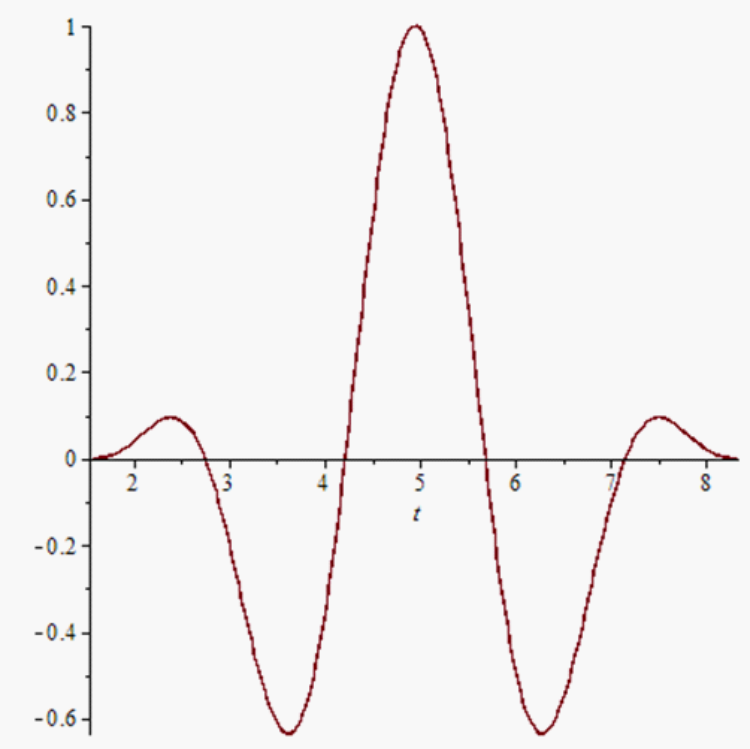

In a typical MAPLE worksheet we compute $\dot{a}_O(t)$ and then employ the method of paragraphs 3.8.3, 3.8.4 to calculate the response $\tilde{L}_m$. In what follows we keep no more than two convective modes. We then compute pressure, force, and height of the wave through (73), (77) and (**??**) respectively. The procedure is repeated for the four different values of H/R and for the earthquakes mentioned in the previous subsection; results are quoted for the Imperial Valley earthquake only.

In Figure 47, 48 we plot the oscillator responses $\tilde{L}_1$, $\tilde{L}_2$ vs time in the case $H/R = 1.$. Note that in this particular case the responses are of the same order of magnitude; this could have been seen from the Fourier spectrum of the accceleration. In Figure 38 we show the force contributions using equation (125). We note that:

(a) The extrema of the impulsive contribution occur at the same times as the extrema of the acceleration since the two are in phase.

(b) The magnitude of the convective contribution of the 2nd mode is quite smaller than the magnitude of the 1st mode despite the fact that the oscillator responses are comparable.This is due to the fact that the convective mass of the 2nd is correspondingly smaller than the convective mass of the 1st (see Figure 31).

In Figure 39 we plot the moment above base as function of time using equation (130).

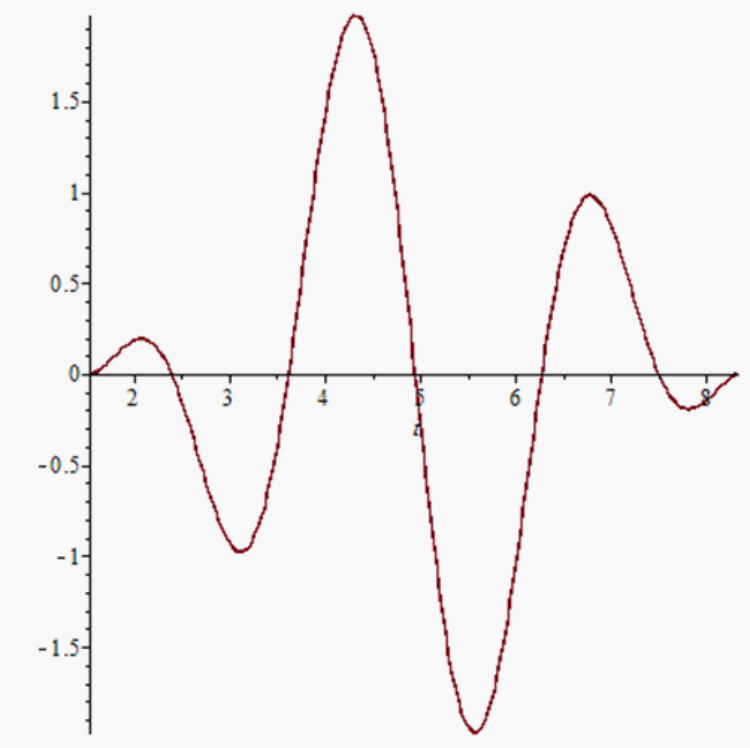

Figure 31: Acceleration graph of the Imperial Valley pulse

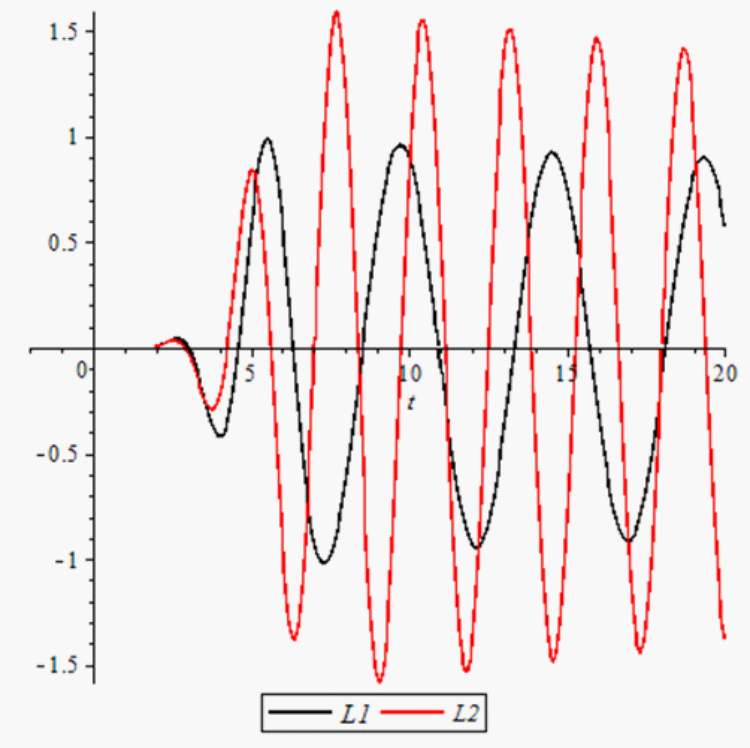

Figure 32: Oscillator responses $\tilde{L}_1$, $\tilde{L}_2$ for the Imperial Valley pulse

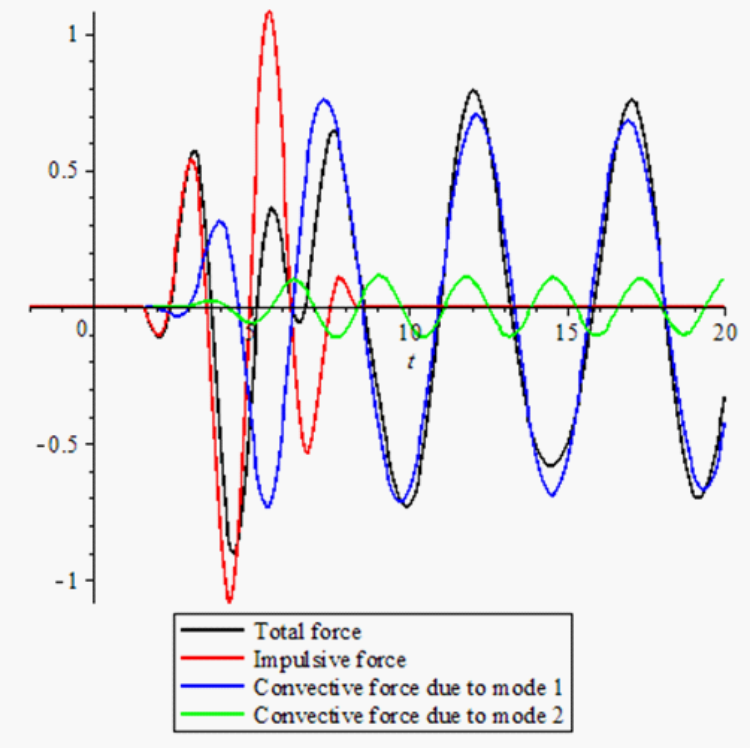

Figure 33: Contributions to $F/(m_l A)$ for the Imperial Valley pulse

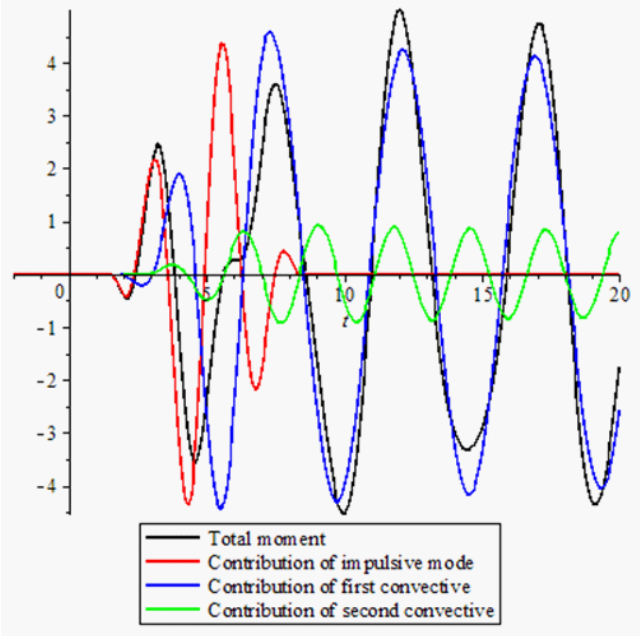

Figure 34: Contributions to (moment above base)/$(m_l A)$ for the Imperial Valley pulse

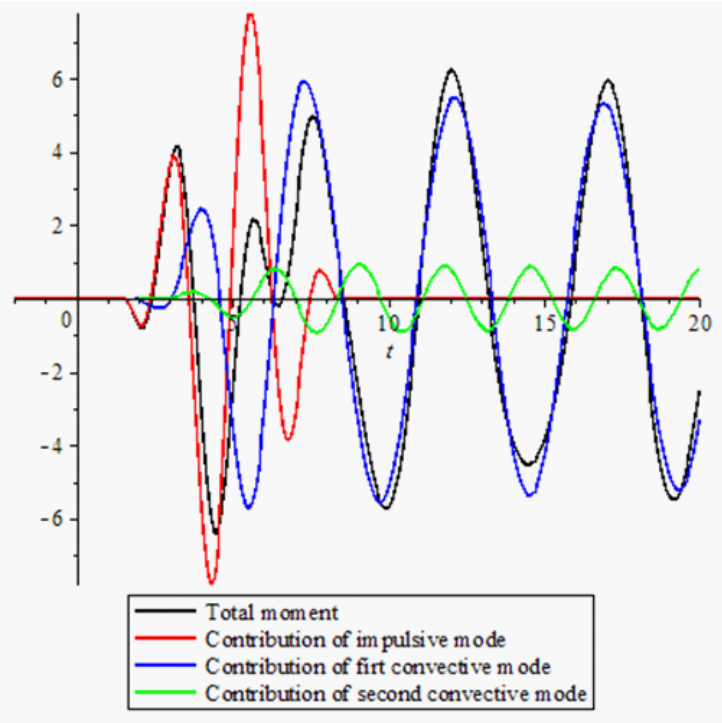

In Figure 40 we plot the moment below base as function of time using equation (132). Note that the total below base moment achives higher values than the above base one due to the fact that the former is subject to an extra contribution from the impulsive force (red curve in Figure 38).

In Figure 41 we plot pressure versus height at $t = 11.970$ s This is approximately the moment when the maximum value of pressure occurs. The increase in pressure as one moves towards the surface is due to the presence of the hyperbolic cosine in the convective modes (see (135), (133)). The fact that the coefficient in front of z in the second convective mode is larger than that in the first ($\lambda_{12} > \lambda_{11}$) makes the effect more pronounced when the second mode is substantial.

In Figure 42 we plot the shape of the surface at the moment of that the height of the sloshing wave is maxmum. Note that the maximum height occurs at the moment of maximum convective presssure on the tank walls. This is always true as can be seen by comparing (137) and (133). In the present case it happens that the times of maximum convective pressure and maximum convective plus impulsive pressure coincide; however it will be seen that the latter is by no means generally true.

In Figure 43 (as well as in Figure 42) we plot the surface displacement along the radial direction at times where the former is quite pronounced.

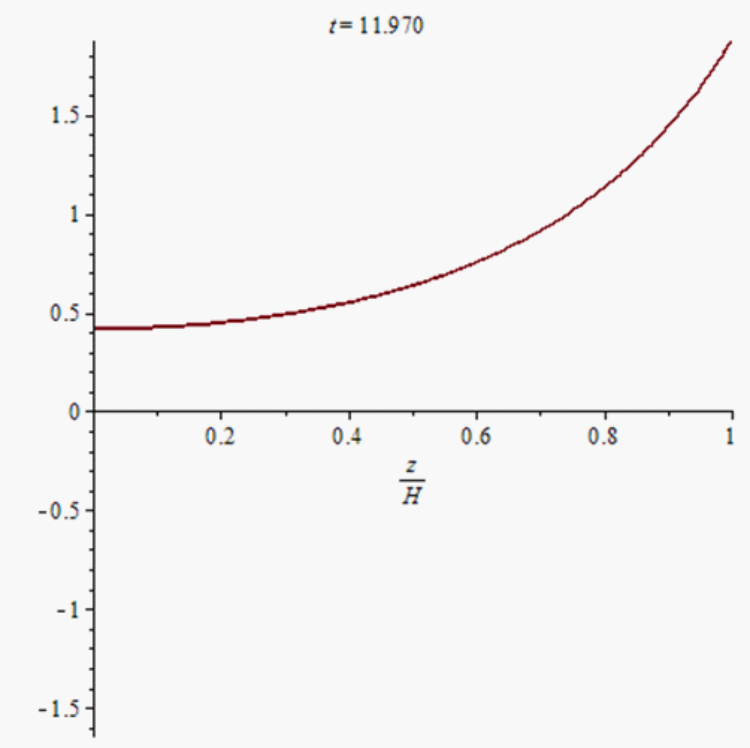

Figure 35: Plot of $p/(A\rho R)$ vs height. Hydrostatic pressure is not included.

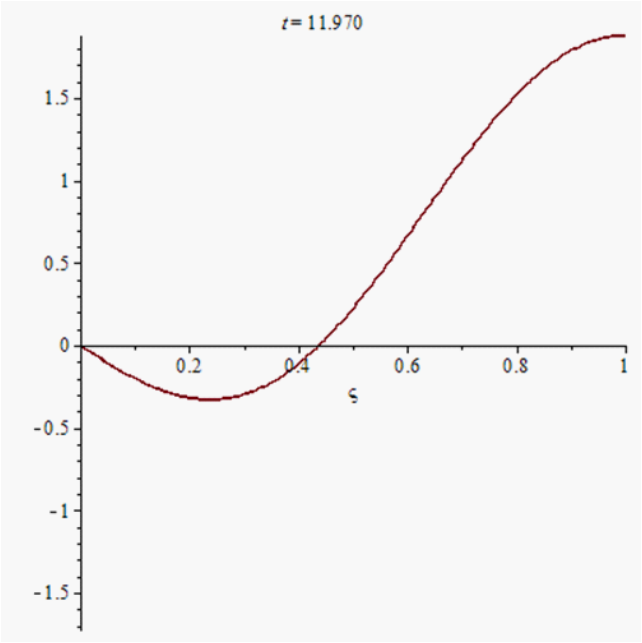

Figure 36: Surface displacement $\frac{g\xi}{AR}$vs the normalized radial direction $\varsigma = \frac{r}{R}$

We see from Figures 23, 24 that the occurrence of a minimum of the wave-pattern in Figure 42 is due exclusively to the inclusion of the second mode. The fact that the maximum in Figure 43 occurs *away from the wall* is again due to the second mode.

Results for pulses corresponding to other earthquakes for various values of H/R are summarized and discussed in a following section.

5.3 Original accelerograms of near-fault earthquakes

5.3.1 Oscillator responses

We apply the procedure described in paragraphs 3.8.3, 3.8.4 and in Subsection 3.9 to the accelerograms corresponding to the earthquakes Imperial Valley (Station EMO-SN component), Northridge (Station JFA-SN component) and Erzincan (Station ERZ- SN component) (source: PEER Gound Motion Database). We present in detail the analysis of the Imperial Valley earthquake for $H/R = 1$. The accelerogram is shown in Figure 44 and the power spectrum is given in Figures 45 and 46.

We observe that the power spectrum has two nearby maxima at $\omega = 2.388$ s^{-1} and $\omega = 3.707$s^{-1}. On the other hand we note that in the range of H/R from 0.3 to 2.5 the angular frequency of the first mode ranges from 0.952 s^{-1} to 1.340 s^{-1} and that of the second mode ranges from 2.194 s^{-1} to 2.286 s^{-1}.. So we are near resonance and sloshing

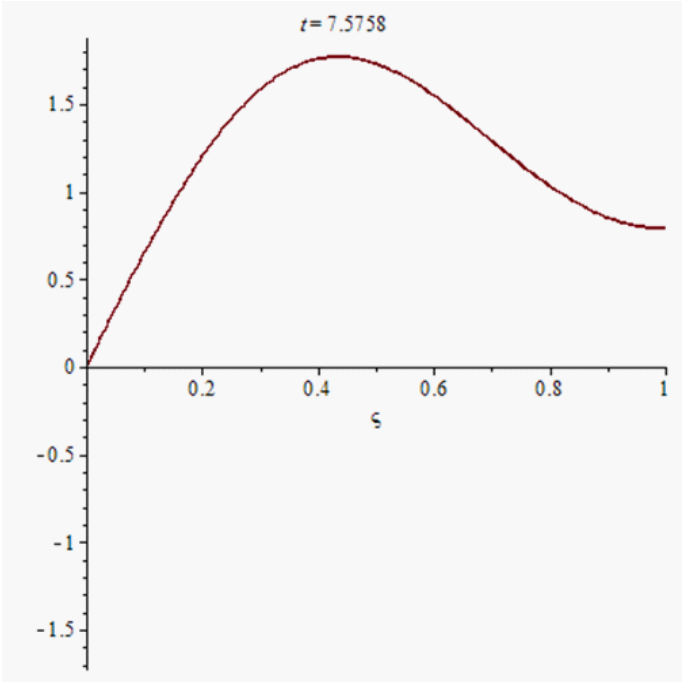

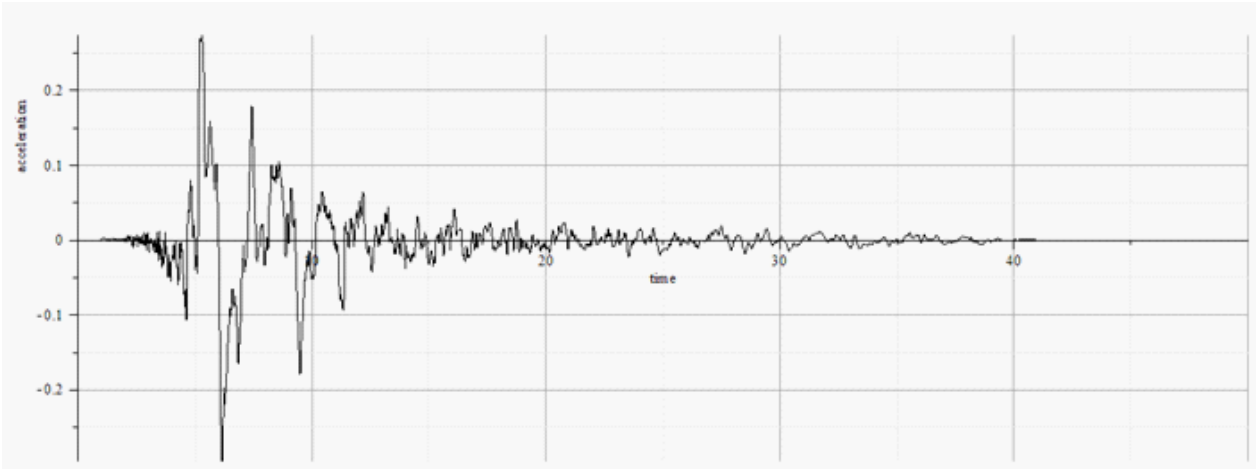

Figure 37: Acceleration in units of g vs time

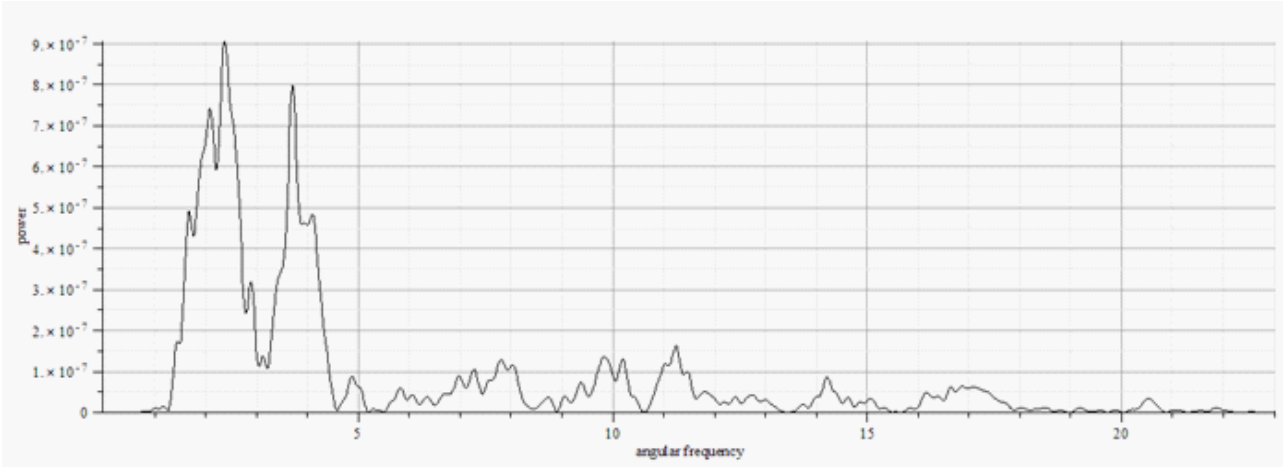

Figure 38: Power spectrum of the accelerogram of Figure 43

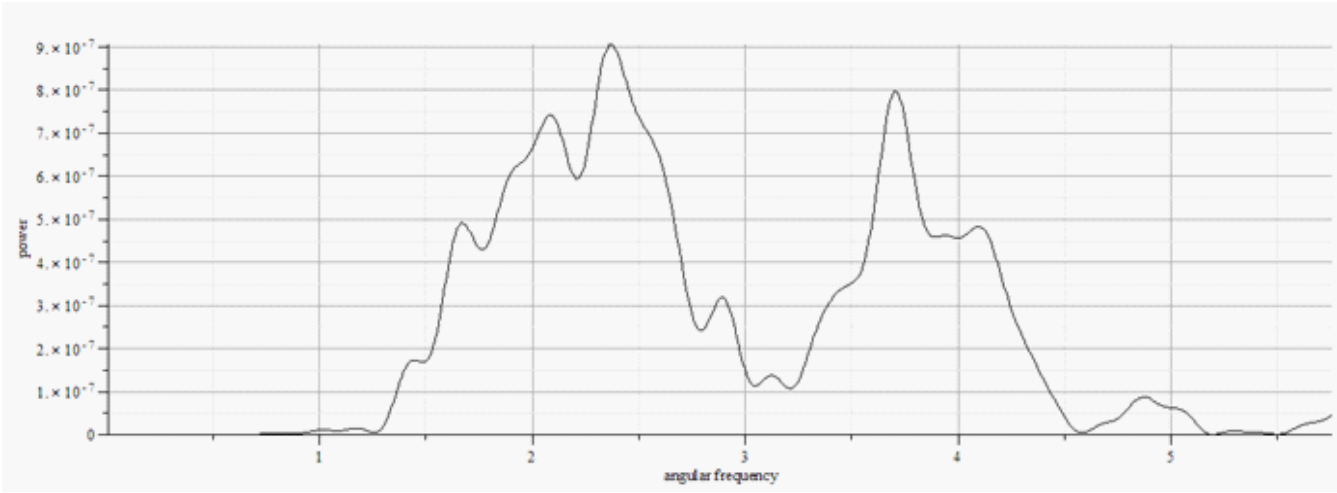

Figure 39: Magnified power spectrum

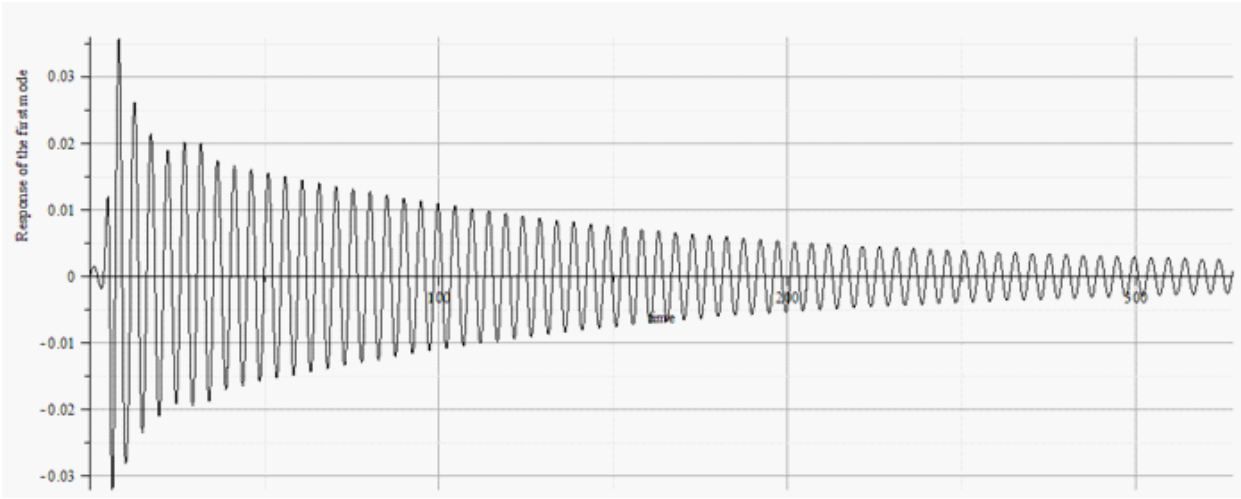

Figure 40: Oscillator response $\tilde{L}_1$

effects are of interest in the case of this particular earthquake. The responses $\tilde{L}_1$, $\tilde{L}_2$ as functions of time are given in Figures 47 and 48 for the case $H/R = 1.0$.

We observe that the maxima $\tilde{L}_1$, $\tilde{L}_2$ are of comparable magnitude. We also note the profiles of $\tilde{L}_1$, $\tilde{L}_2$ are free of noise. This is due to the fact that each oscillator acts as a low-pass filter cutting off high frequency noise (see the transfer funtion in equation (146)). The faster decay of $\tilde{L}_2$ is due to the stronger exponential decrease according to equation (126). Based on $\tilde{L}_1$, $\tilde{L}_2$ we calculate force, pressure, moment and height of the wave as functions of time. From now on we denote by the subscripts 0, 1, 2 the contributions of the impulsive, first convective and second convective modes respectively. The sum of these three terms gives the total force, pressure and moment.

5.3.2 Force

Figures 49 to 53 show F_0, F_1, F_2 and total force$F$ respectively as functions of time. Results are given in the SI and, as far as the force is concerned, per unit mass of the liquid. Recall that according to the remark made before equation (139) we had to calculate the response for a time interval $65536 \times 0.005\ \text{s}^{-1} = 327.5\ \text{s}^{-1}$.

We observe the following:

1. The impulsive force F_0 is proportional to the ground acceleration and hence vanishes for times greater than 40 s. On the other hand, theconvective contributions F_1, F_2 are proportional to the responses $\tilde{L}_1$, $\tilde{L}_2$ and decay accordingly.

2. Concerning the relative magnitude of the maximum values of

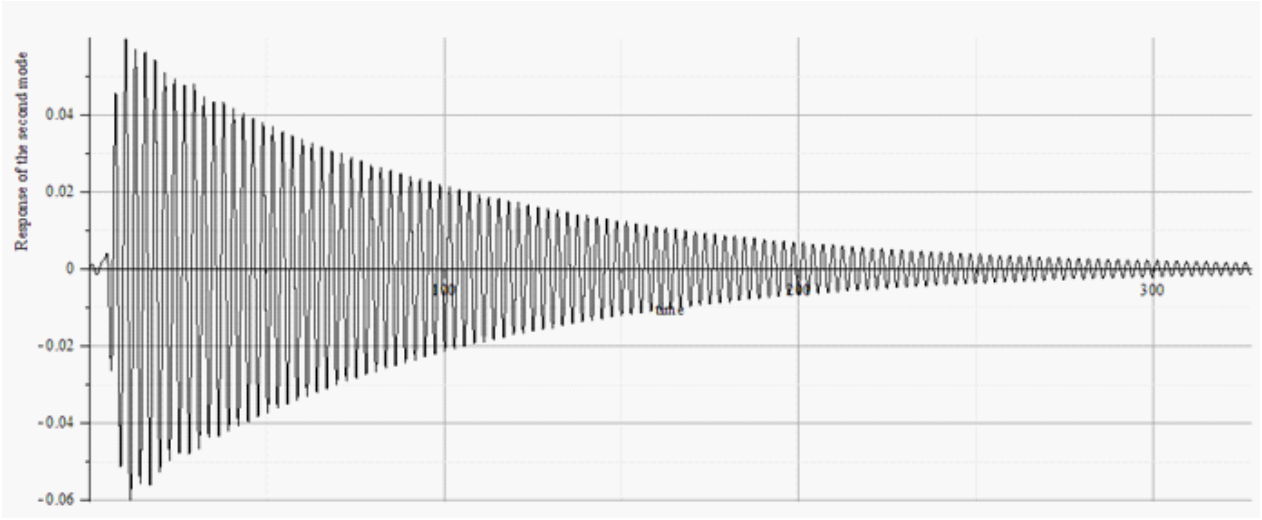

Figure 41: Oscillator response $\tilde{L}_2$

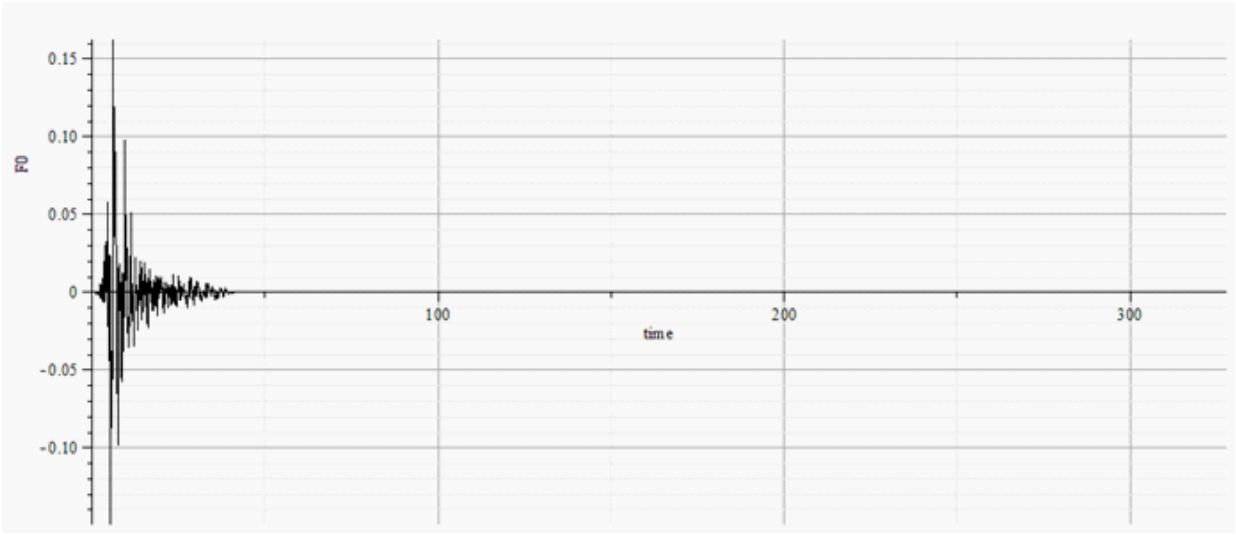

Figure 42: Impulsive force F_0/m_l vs time

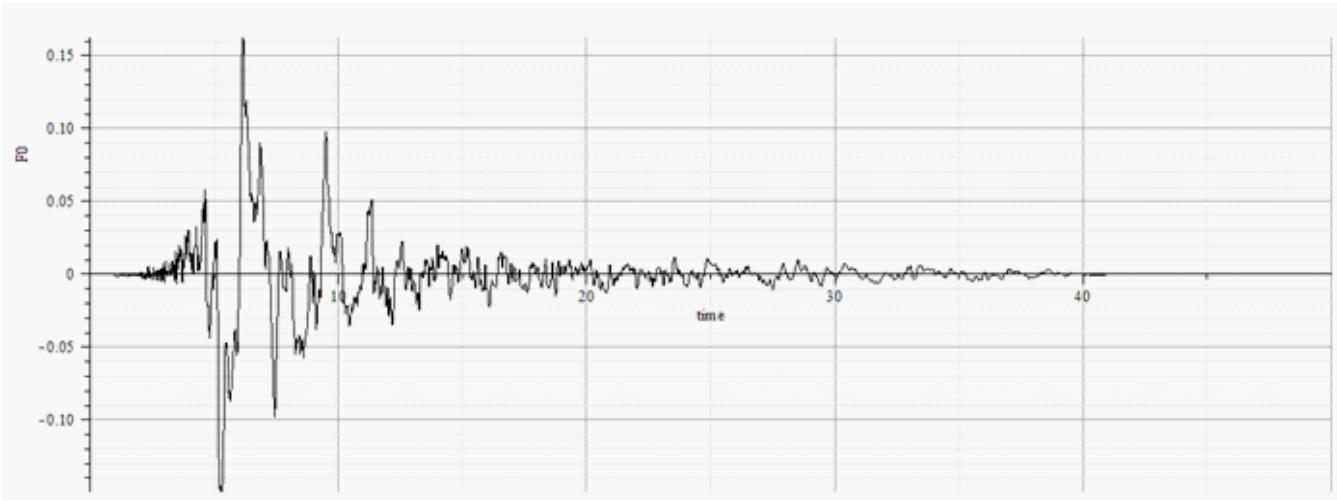

Figure 43: Magnified view of F_0 vs time

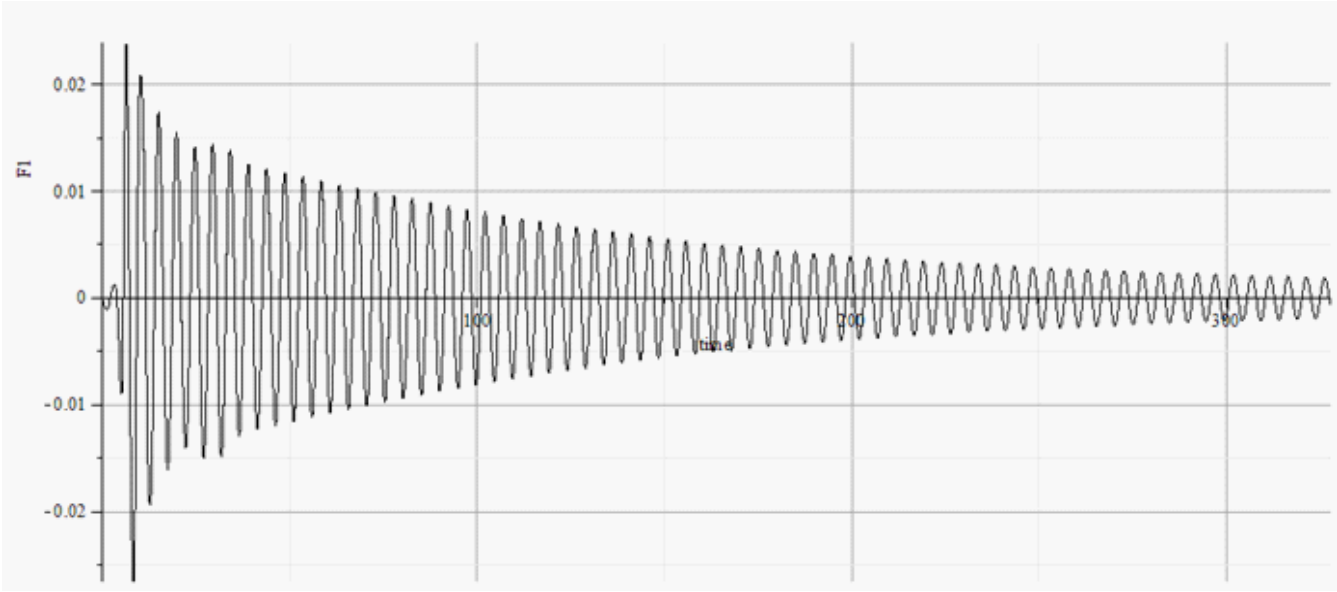

Figure 44: Convective F_1/m_l vs time

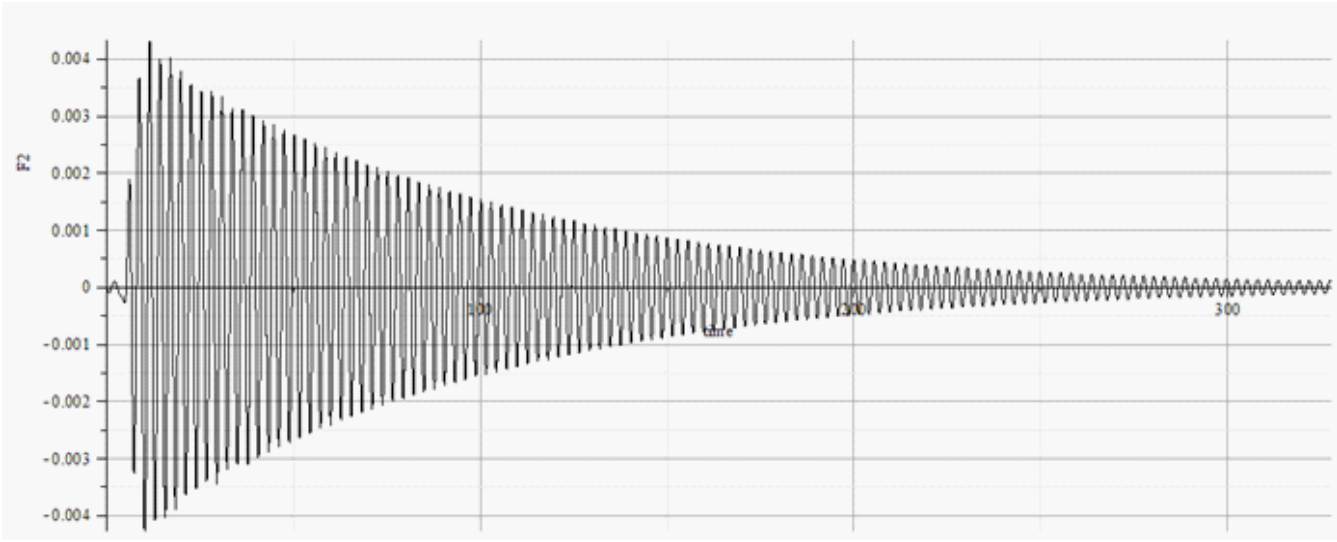

Figure 45: Convective F_2/m_l vs time

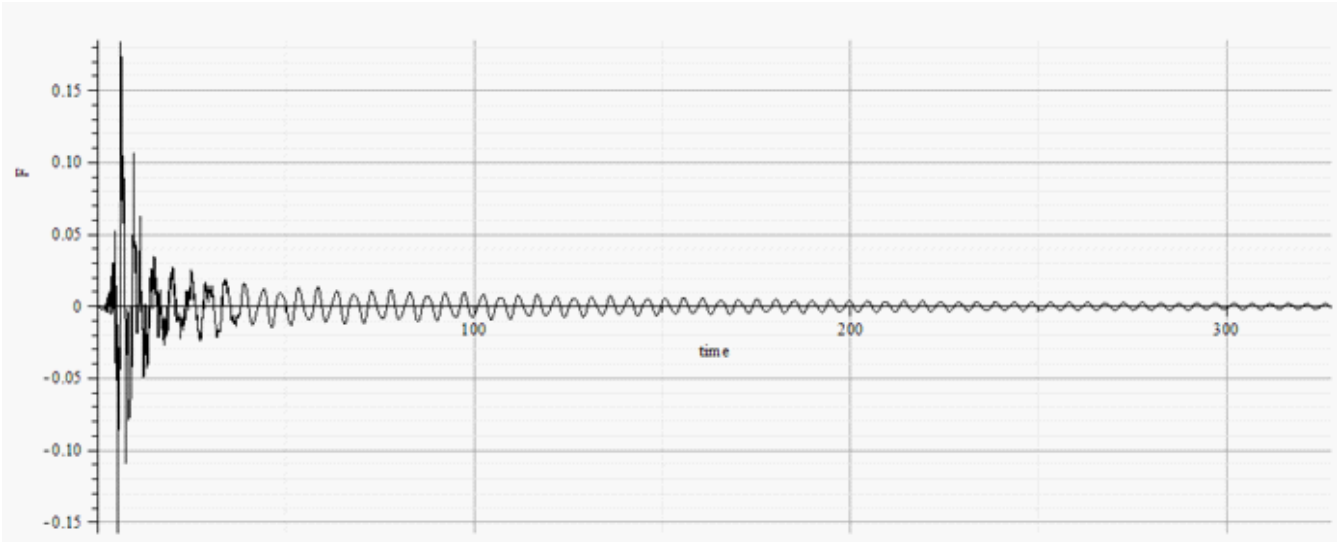

Figure 46: Total F vs time

F_0 and F_1 we note that for $H/R = 1$ the impulsive mass m_0 and the convective mass of the first mode m_1 are almost equal according to Figure 29. Comparing the maximum ground acceleration from Figure 44 to the maximum acceleration $\omega_{1m}^2 \tilde{L}_1$ deduced from Figure 47 and using $\omega_{1m} = 1.31$ s^{-1} we deduce that the maximum of F_1 is about one order of magnitude less than the maximum of F_0. This is indeed borne out by comparing Figures 50 and 51.

3.The smallness of the maximum of F_2 compared that of F_1 is explained by the smallness of convective mass m_2 compared to m_1 (see Figure 29 and equation (125)).

To appreciate the orders of magnitude involved, note:
$F_{0\,\max}/(F_{0\,\max} + F_{1\,\max} + F_{2\,\max}) = 88.5\%$,
$F_{1\,\max}/(F_{0\,\max} + F_{1\,\max} + F_{2\,\max}) = 9.3\%$,
$F_{2\,\max}/(F_{0\,\max} + F_{1\,\max} + F_{2\,\max}) = 2.2\%$,
$F_{0\,\max}/F_{\max} = 87.6\%$
$F_{1\,\max}/F_{\max} = 9.19\%$
$F_{2\,\max}/F_{\max} = 2.16\%$

It is clear that despite the that we are near resonance with the second convective mode, its contribution to the total force is negligible.

5.3.3 Pressure

According to the discussion in Section 3 the maximum of the impulsive pressure occurs at the bottom of the tank ($z = 0$), while the maximum of the convective occurs at top ($z = H$). In Figures 54 to 58 we plot scaled by ρR vs time. Figures 54, 55 show the impulsive pressure at the bottom vs time. Figures 56, 57 show the pressure at the top of the wall due to the first and second convective modes respectively (convective pressures at the bottom are negligible). We observe that the maximum impulsive contribution is larger than the maixima of p_1 and p_2 by a factor of ten, which was to be expected given the similar situation with the forces. Convective pressues p_1 and p_2 are of comparable order of magnitude. This is to be understood as follows. We have already mentioned that the responses $\tilde{L}_1$, $\tilde{L}_2$ are of comparable magnitude. According to equation (133) the convective pressure depends on $C_m\omega_{1m}^2$ and ω_{1m}^2 roughly cancels with $\lambda_{1m}^2 - 1$ present in the denominator of (135).

It is evident from the orders of magnitude involved in the graphs of the Figures 54 to 57 that the maximum pressure occurs at the bottom of the tank and is due mainly to the impulsive contribution. 58 shows the pressure at the bottom as a function of time. Figure 59 shows the pressure profile along the z-axis at the moment of maximum impulsive pressure (i. e. at the moment of maximum acceleration). Note that the contribution of the convective modes. However, before discarding

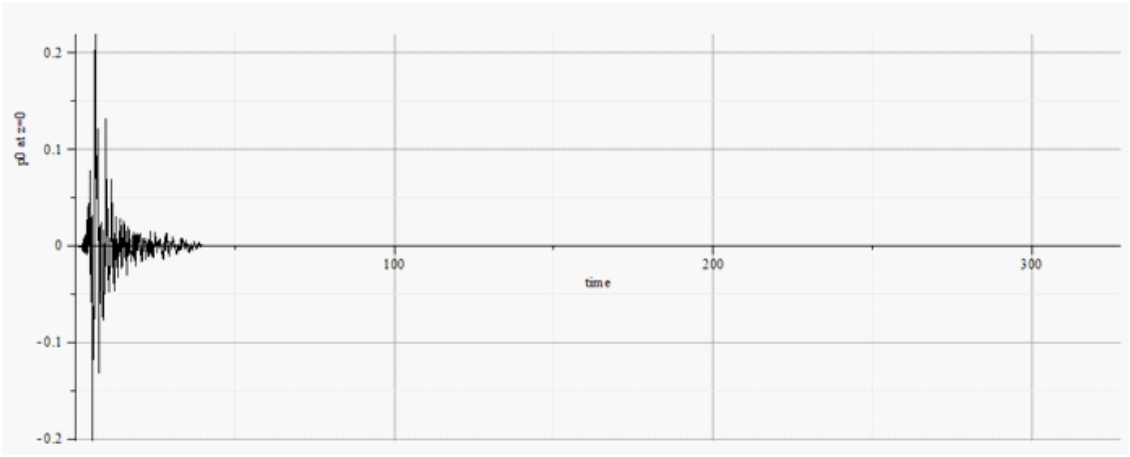

Figure 47: Impulsive pressure $p_0/(\rho R)$ at bottom vs time

the importance of convective pressures p_1 and p_2 for design purposes one should take into account the fact that these pressures act for a long time (much longer than the duration of acceleration), in contrast to the impulsive pressure.

5.3.4 Moments

Observations similar to the force can be made regarding moments. We show only the total contributions to moment above and moment below base.

5.3.5 Displacement of the surface

In Figure 62 we plot the height of the wave vs radial distance at a moment when the former is quite pronounced. Note that the wave has a maximum at about $r/R = 0.42$. The fact that the maximum does not occur on the wall (and that the hump in the Figure is so obvious) is a manifestation of the importance of the second convective mode (a similar remark has been made in the discussion of pulses).

In Figure 63 we choose $r/R = 0.42$ (where the maximum in Figure 62 occurs) and plot the height of the wave vs time.

If we ignore the contribution of the second mode we can show that the maximum height (now occurring at $r = R$) equals about 0.05 (in the units of Figure 63). We thus observe that (a) the contribution of the second mode to the height of the wave amounts to 20% of that of the first mode, (b) taking into account the second mode the maximum occurs about half-way between axis and walls.

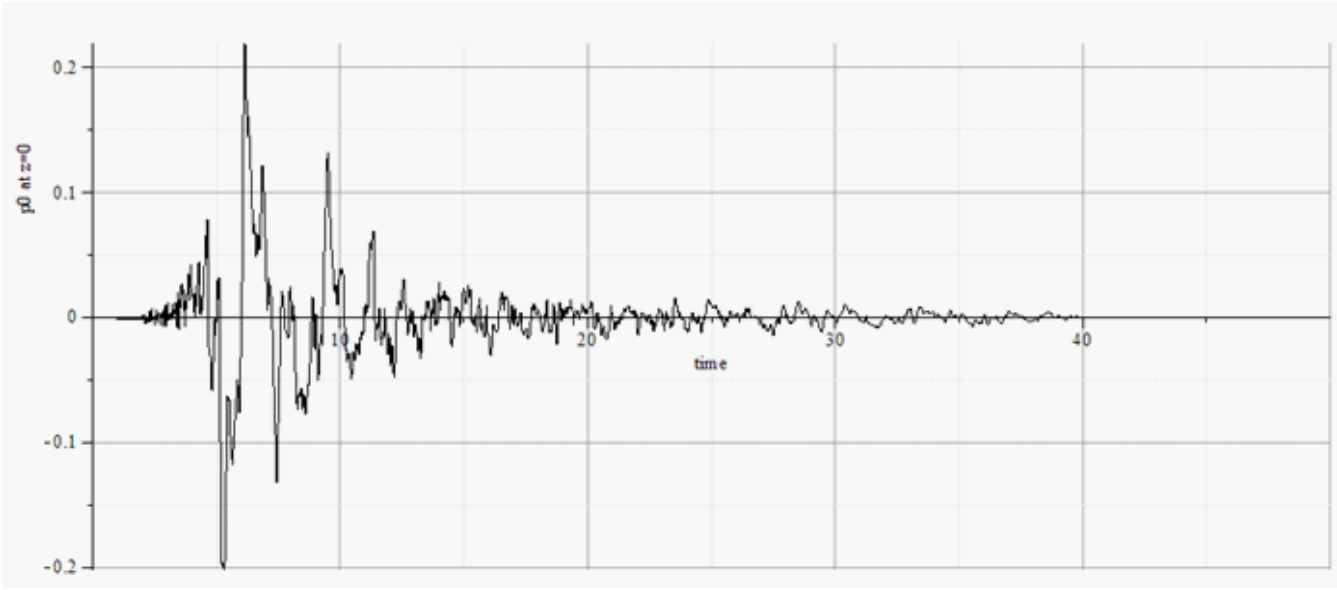

Figure 48: Magnified view of impulsive pressure $p_0/(\rho R)$ at bottom vs time

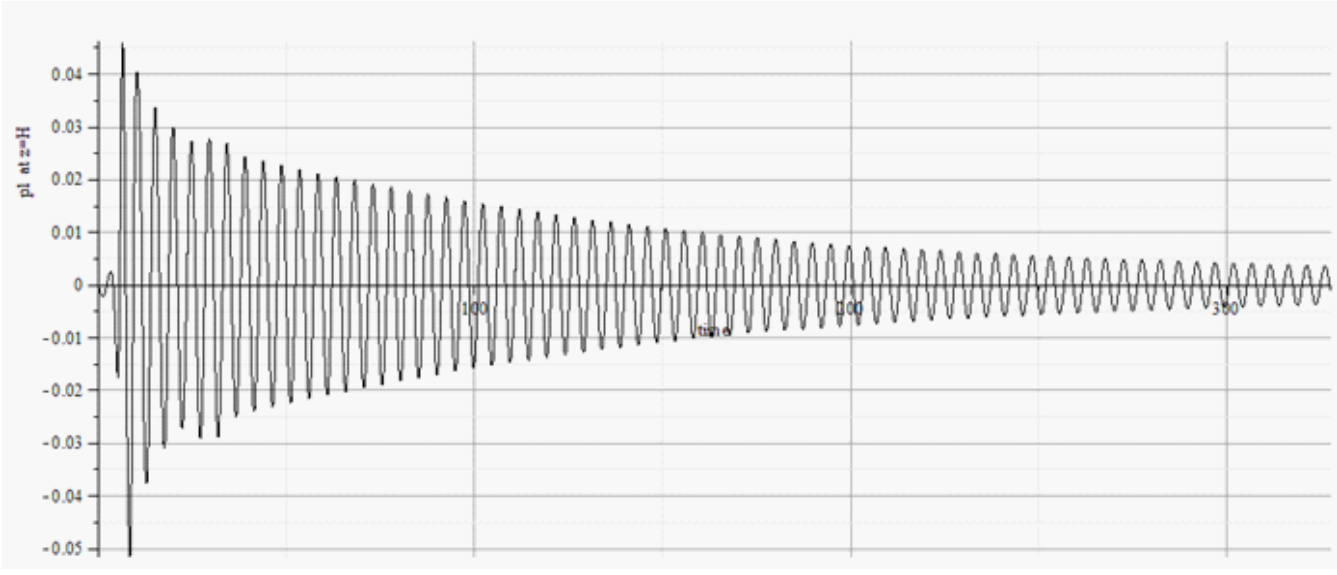

Figure 49: Convective pressure $p_1/(\rho R)$ at top vs time

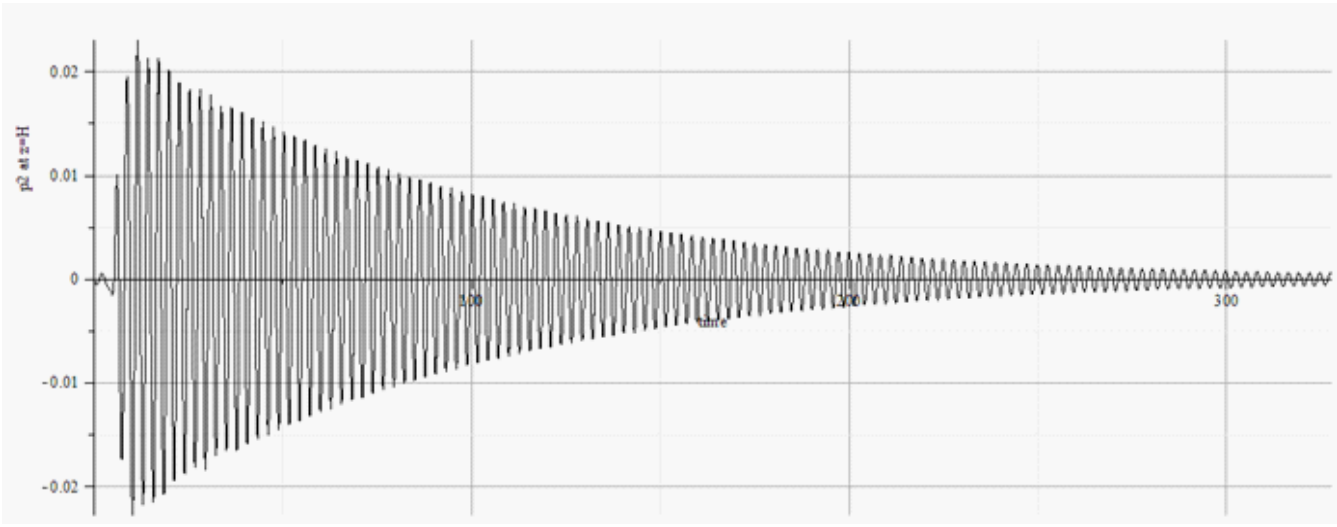

Figure 50: Convective pressure p_2 at top vs time

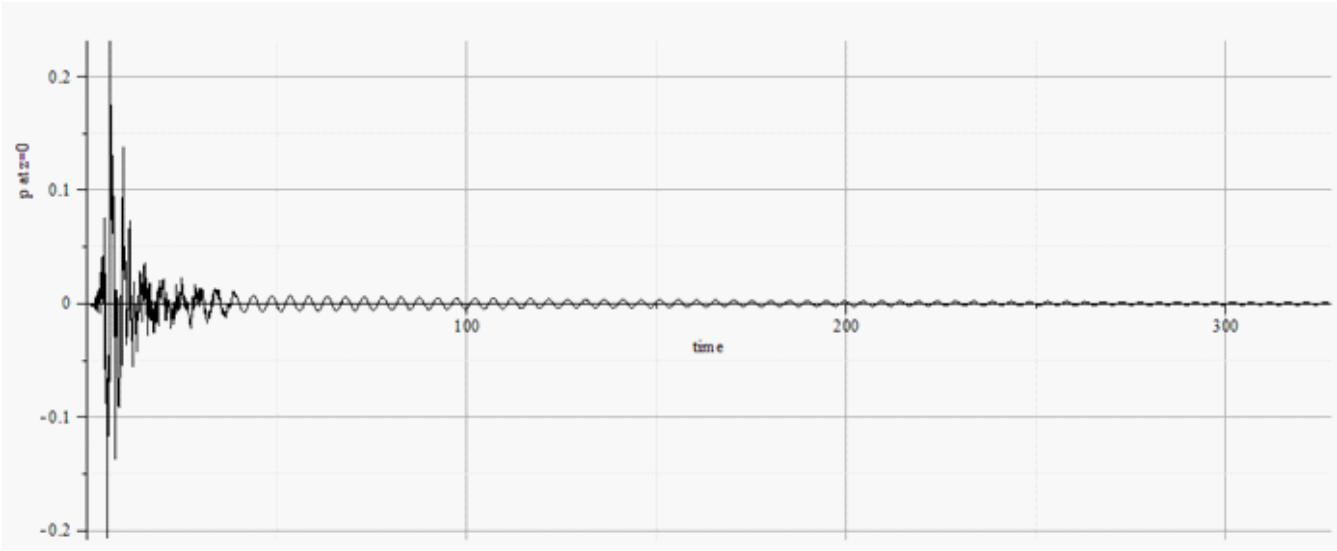

Figure 51: Total pressure $(p_0 + p_1 + p_2)/(\rho R)$ at bottom vs time

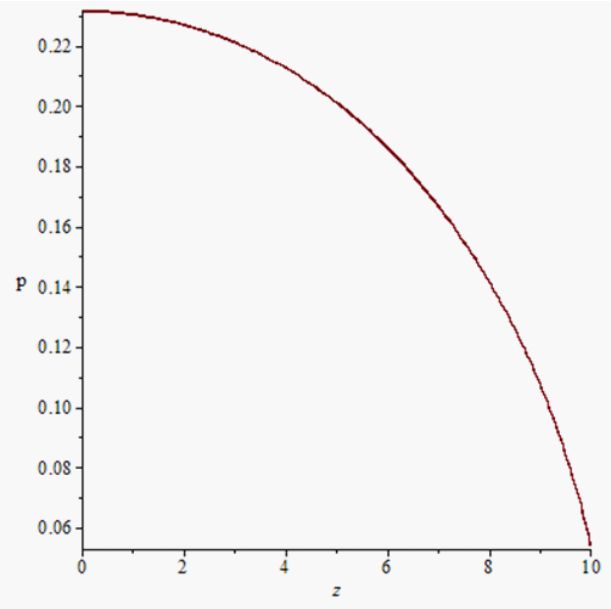

Figure 52: Total pressure/(ρR) vs height at the time when the former achieves an overall maximum

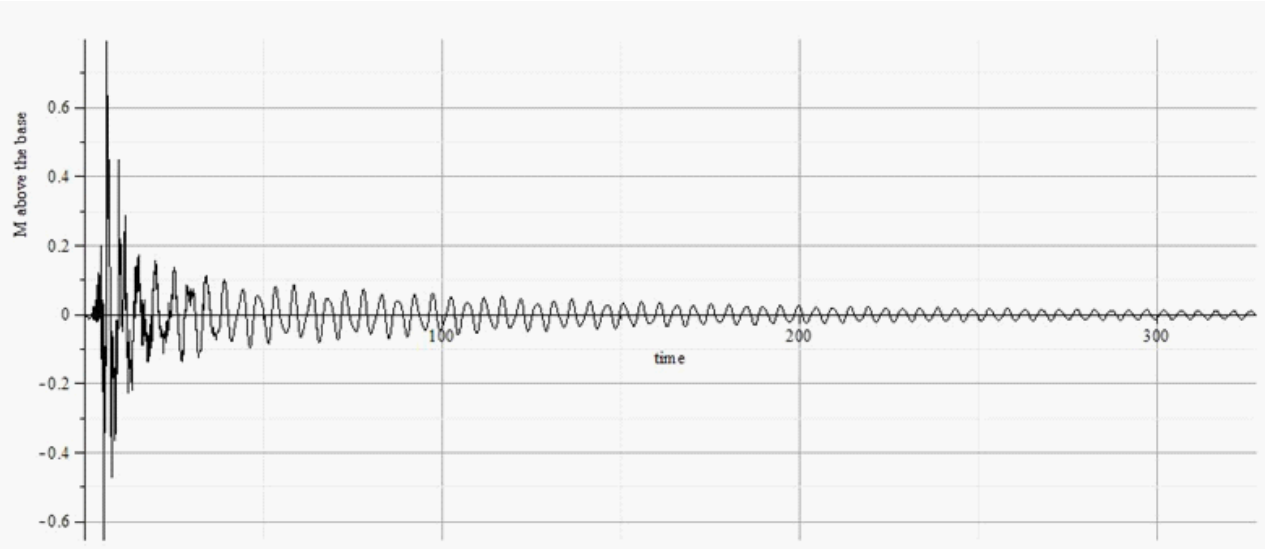

Figure 53: Total moment above base//(ρR) vs time

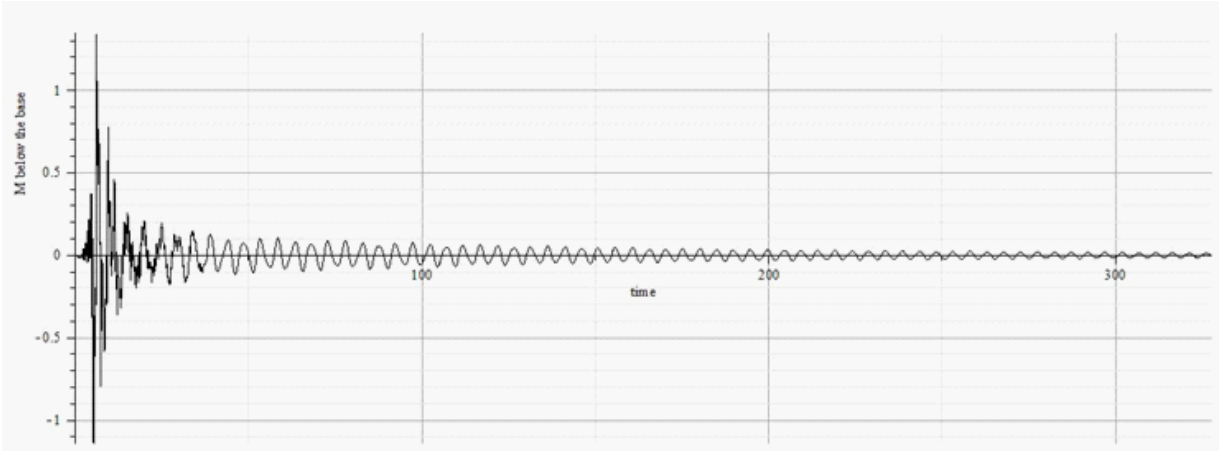

Figure 54: Total moment below base/(ρR) vs time

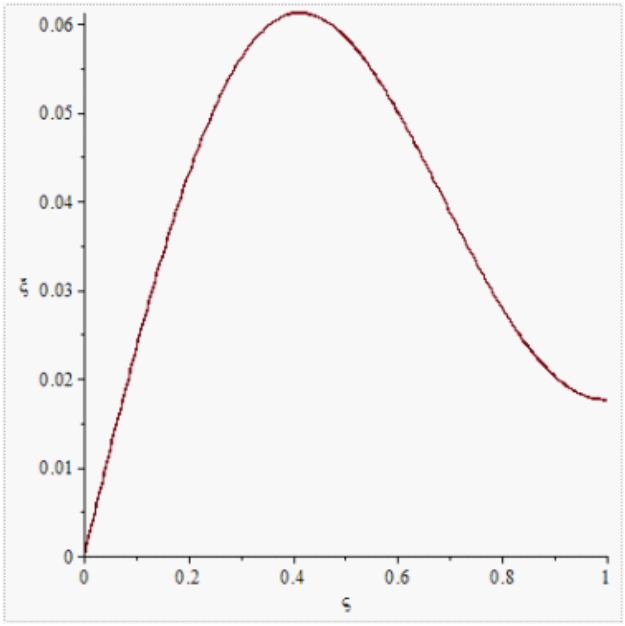

Figure 55: The height of the wave $\times g/R$ vs radial distance

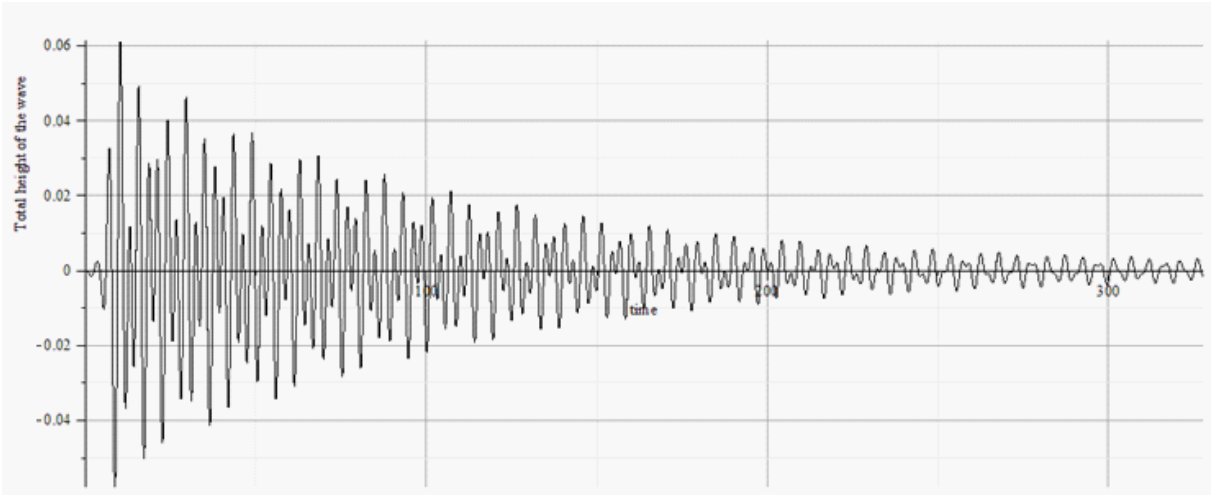

Figure 56: Height of the wave $\times g/R$ vs time at $r/R = 0.42$

5.4 Discussion of the results for three earthquakes and for four values of the parameter H/R

In the previous subsection we discussed at length the predictions for force, pressure, moments and height of the wave in the case of the Imperial Valley earthquake in the case of $H/R = 1$. We have carried out similar analyses for the Northridge and Erzincan earthquakes. As mentioned in the introduction to the present section the three earthquakes were analyzed for $H/R = 0.3,\ 0.5,\ 1,\ 2.5$.

In the graphs below whenever we refer to a quantity (force or height of the wave) we mean its *maximum* value over time computed via the methods of the previous paragraph. When we use the adjective *average* we mean the average over the three earthquakes.

In Figure 64 we plot the average responses $\tilde{L}_1$, $\tilde{L}_2$ corresponding to the first and second convective modes as a function of H/R. It is evident that the magnitude of the response of the second mode is substantially higher than that of the first mode (by a factor 2.7). This is a consequence of the fact that the selected earthquakes are at resonance with the second convective mode (this is evident in the power spectrum of the Imperial Valley accelerogram). In the analysis that follows we will examine how this resonance is manifested in two fundamental quantities of interest, base shear and height of the sloshing wave.

We conclude that:

1. The response is dominated by the impulsive mode with the contribution of the first mode being relatively small

2. Despite the fact that the earthquake is in resonance with the

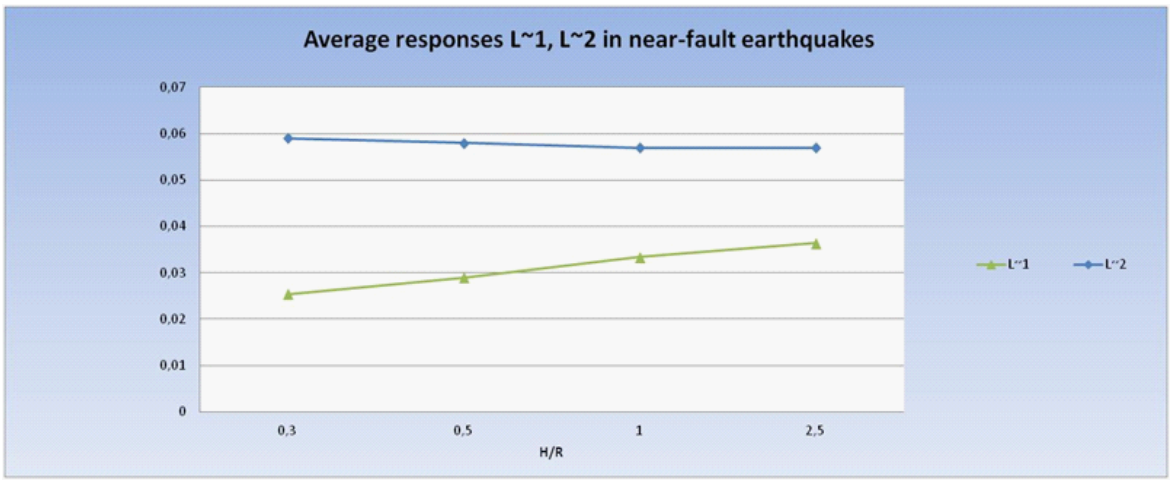
Average responses L~1, L~2 in near-fault earthquakes
0,07
0,06
0,05
0,04
0,03
0,02
0,01
0
0,3
0,5
1
2,5
H/R
L~1
L~2

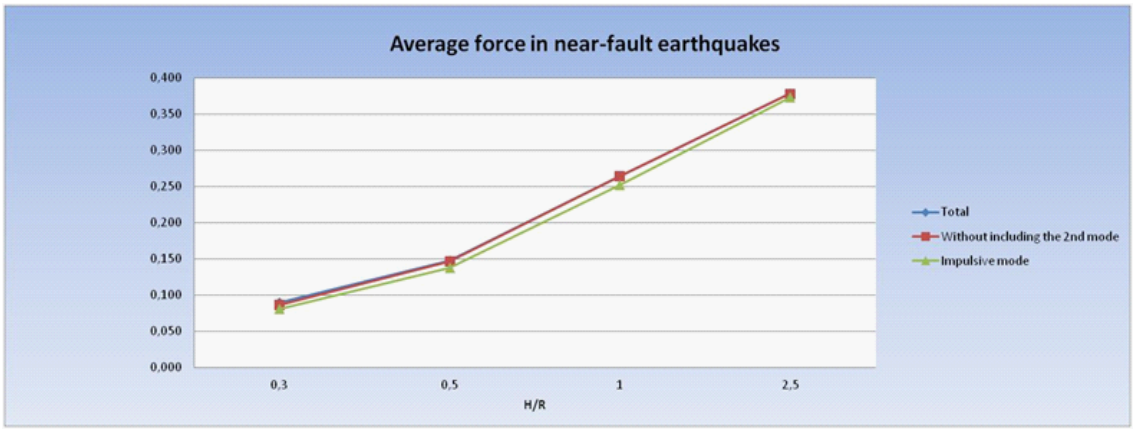
Average force in near-fault earthquakes
0,400
0,350
0,300
0,250
0,200
0,150
0,100
0,050
0,000
0,3
0,5
1
2,5
H/R
Total
Without including the 2nd mode
Impulsive mode

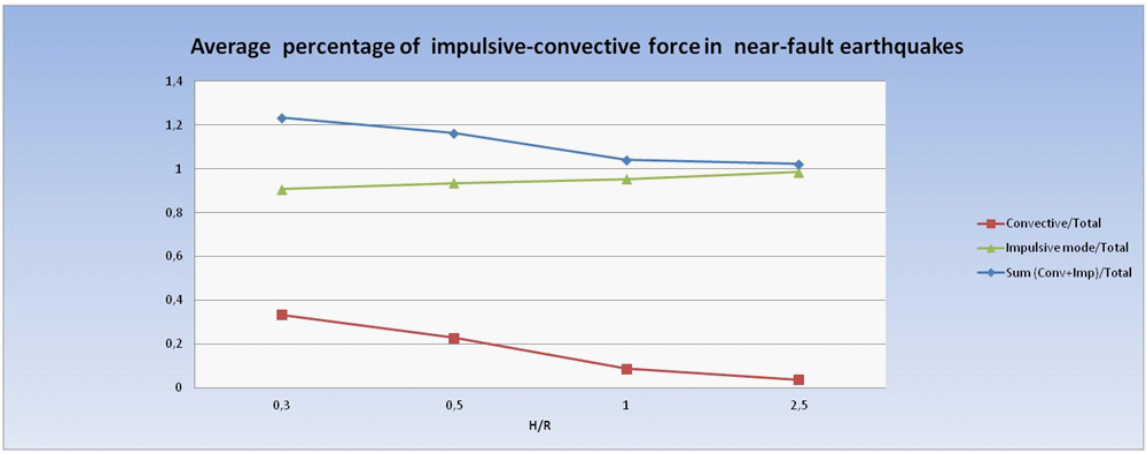

second convective mode the smallness of convective mass μ_2 compared to impulsive mass μ_0 and first convective mass μ_1 result to a small force contribution of the second convective mode (3% of the total at most).

3. The total force increases as H/R increases because μ_0 increases.

Figure 66 shows the participation of each component – impulsive mode and the two convective modes- to the overall force. The values shown are the ratios of the average maxima of each component to the average maximum of the total force. Note that summing up these maxima (i. e. using the absolute summation rule) does not result to the maximum of the total force. For this reason we also show the ratio of this sum to the actual total force. The following observation can be made:

The contribution of the convective component is relatively low (about 30% at most) compared to the contribution of the impulsive component, and decreases as we move to higher values of H/R. This can be explained as follows: for small values of H/R, where $\mu_1 > \mu_0$ the acceleration $\omega_1^2 \tilde{L}_1$ of the first oscillator is significantly lower than the peak ground acceleration a_O (values of $\tilde{L}_1$ are low, as expected by the power spectra of the earthquakes, and values of ω_1 are also low in this range of H/R). For larger values of H/R (larger than 1), while the response acceleration rises to values comparable to a_O (due to the higher value of ω_1), μ_1 decreases and μ_0 increases, thus resulting to the domination of the impulsive force for all H/R values.

The contribution of the second mode is more pronounced in the calculation of the height of the sloshing wave (where there is no impulsive component). The consideration of the 1st mode only, as proposed by Eurocode 8, significantly underestimates the height of the sloshing wave. For instance, for $H/R = 0.5$ and $H/R = 0.3$ this underestimation ranges from 30% to 50%, respectively, as shown in Figure 67 Consideration of

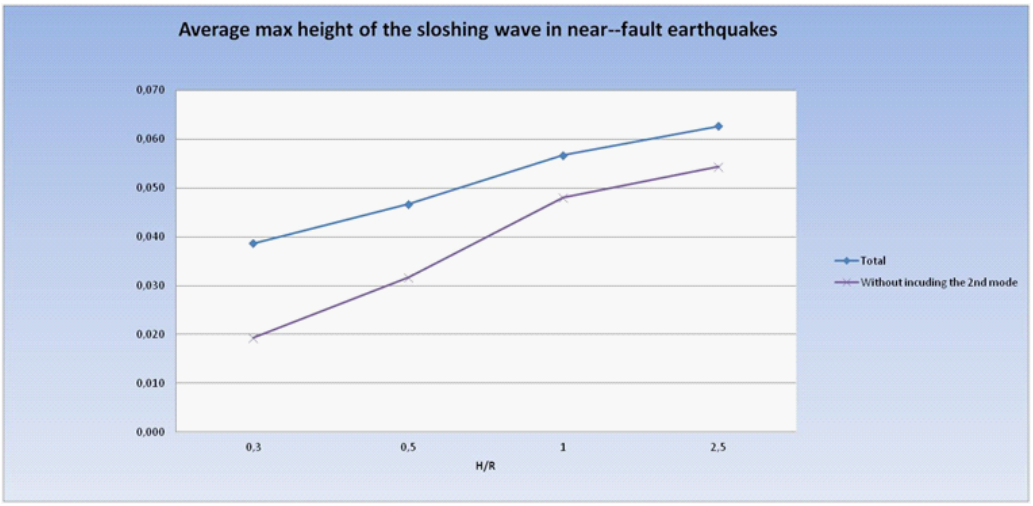

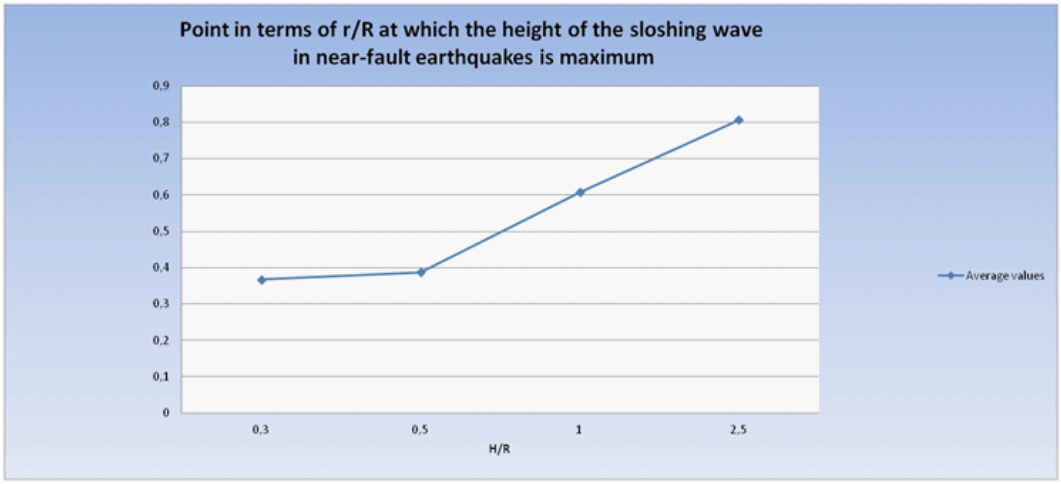

the second mode is thus significant for the estmation at the design stage of the necessary height of the free board.

Observing the same plot we may conclude that the contribution of the second mode decreases as the ratio H/R increases. This is attributed to the factor in front of $\tilde{L}$ in the equation that gives the height of the wave. We calculate the ratio $\xi 2/\xi 1$. The multiplier of $L2/L1$consists of a constant (<1), the dependence of r/R, and a function of H/R(which decreases as H/Rincreases).

Furthermore, it should be noted that the dominance of the second mode results to a corresponding profile of the free surface (see profiles of the second modes in Section 3). This is demonstrated by plot 68 that shows, in terms of r/R, the point at which the height of the wave has a maximum.

Note that considering the only the first mode, the maximum height

of the wave occurs at the tank wall ($r = R$). However, the contribution of the second mode significantly changes the profile of the wave. We see that for small values of H/R (<1) the maximum height occurs closer more towards the center (r/R is below 0.5, approaching the value 0.37, where the second profile of the Bessel function has a maximum). This may pose a question regarding the design of the tank roof (especially in the case of floating roofs). As we move towards higher values of H/R the behavior of the surface approaches the profile of the first mode (r/R approaches 1.0), something expected since the overall contribution of the second mode decreases.

Futher discussion of these issues is included in a paper in progress.

6 Appendix A The boundary conditions at the free surface

We derive the kinematic boundary condition following Debnath (2005). We first consider a fixed tank. The free surface is described by equation (13):

$$z - \xi(x, y, t) = H. \tag{164}$$

Two points at the surface separated in space by dx, dy, dz and in time by dt satisfy (taking the differential of the above):

$$\begin{aligned} dz - \frac{\partial \xi}{\partial x} dx - \frac{\partial \xi}{\partial y} dy - \frac{\partial \xi}{\partial t} dt = 0, \Rightarrow \\ \frac{dz}{dt} - \frac{\partial \xi}{\partial x}\frac{dx}{dt} - \frac{\partial \xi}{\partial y}\frac{dy}{dt} - \frac{\partial \xi}{\partial t} = 0. \end{aligned} \tag{165}$$

In terms of velocities the above reads

$$v_z - \frac{\partial \xi}{\partial x} v_x - \frac{\partial \xi}{\partial y} v_y - \frac{\partial \xi}{\partial t} = 0, \tag{166}$$

and in terms of the velocity potential

$$\frac{\partial \Phi}{\partial z} - \frac{\partial \xi}{\partial x}\frac{\partial \Phi}{\partial x} - \frac{\partial \xi}{\partial y}\frac{\partial \Phi}{\partial y} - \frac{\partial \xi}{\partial t} = 0. \tag{167}$$

This is equation (14).

In the case of a moving tank we take the surface to be described again by (164) where the coordinates x, y, z now refer to the moving frame (see Figure). We thus arrive at (165) where quantities dx/dt, dy/dt, dz/dt stand for velocities relative to the *moving frame.* Equation (166) now reads:

$$v_{rel,z} - \frac{\partial \xi}{\partial x} v_{rel,x} - \frac{\partial \xi}{\partial y} v_{rel,y} - \frac{\partial \xi}{\partial t} = 0. \tag{168}$$

We express the above in terms of the velocity potential (56) to arrive again at (167).

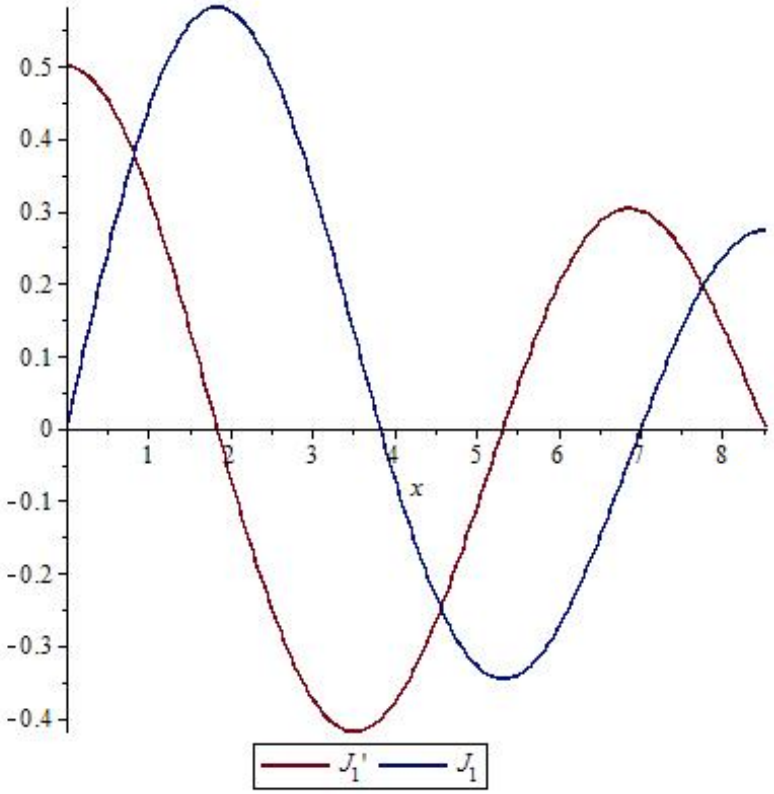

7 Appendix B The zeros λ_{nm} of J_n'

The mth root of the Bessel derivative J_n' is denoted in the text by λ_{nm} (see second line after (29)). In the table below we give the first five roots for the Bessel function derivatives J_0', J_1', J_2' (Weisstein 2014):

	J_0'	J_1'	J_2'
1st	3.831	1.841	3.054
2nd	7.015	5.331	6.706
3rd	10.173	8.536	9.969
4th	13.323	11.706	13.170
5th	16.470	14.863	16.347

It is shown in the text that the roots of J_1' are of particular interest. The plot of J_1' is easily obtained in MAPLE (Figure).

By making use of the zoom facility of MAPLE we can compute some further zeros of J_1'. We obtain $\lambda_{16} \simeq 18.015$, $\lambda_{17} \simeq 21.164$, $\lambda_{18} \simeq 24.311$, $\lambda_{19} \simeq 27.457$.

8 Appendix C The Fourier-Bessel expansion

Let a function $f(x)$ be defined for $0 \leq x \leq 1$. As in the text, λ_{nm}denote the zeros of J_n'. Then $f(x)$ can be expanded in the so-called Fourier-Bessel series:

$$f(x) = \sum_{m=1}^{\infty} A_m J_n(\lambda_{nm} x), \tag{169}$$

where the coefficients A_m are given by

$$A_m = \frac{2}{(1 - \frac{n^2}{\lambda_{nm}^2}) J_n^2(\lambda_{nm})} \int_0^1 x f(x) J_n(\lambda_{nm} x) dx. \tag{170}$$

We apply the expansion for the case $n = 1$, $f(x) = x$, to obtain

$$x = \sum_{m=1}^{\infty} A_m J_1(\lambda_{1m} x). \tag{171}$$

The integral

$$\int_0^1 x^2 J_1(\lambda_{1m} x) dx \tag{172}$$

is evaluated using Maple to give:

$$-\frac{\lambda_{1m} J_0(\lambda_{1m}) - 2 J_1(\lambda_{1m})}{\lambda_{1m}^2} \tag{173}$$

On the other hand, it is well known that

$$J_1'(t) = J_0(t) - \frac{J_1(t)}{t}. \tag{174}$$

Applying the above for $t = \lambda_{1m}$ we obtain that

$$J_0(\lambda_{1m}) = \frac{J_1(\lambda_{1m})}{\lambda_{1m}}, \tag{175}$$

and substituting (175) in (173) we obtain

$$\int_0^1 x^2 J_1(\lambda_{1m} x) dx = \frac{J_1(\lambda_{1m})}{\lambda_{1m}^2}. \tag{176}$$

Substituting (176) in (170) we obtain

$$A_m = \frac{2}{\left(\lambda_{1m}^2 - 1\right) J_1(\lambda_{1m})}. \tag{177}$$

Hence

$$x = \sum_{m=1}^{\infty} \frac{2}{\left(\lambda_{1m}^2 - 1\right) J_1(\lambda_{1m})} J_1(\lambda_{1m} x). \tag{178}$$

9 Appendix D The integrals in $E^{(1m)}$

We define

$$I_1 \equiv \int_C dS \Psi_{1m}^2. \tag{179}$$

The surface element dS reads in polar coordinates

$$dS = r dr d\vartheta. \tag{180}$$

We use (32) to write (recall that α_1 is absorbed in $\tilde{T}_{1m}$):

$$I_1 = \cosh^2\left(\lambda_{1m}\frac{H}{R}\right) \int_0^R dr \int_0^{2\pi} d\vartheta r \cos^2\vartheta J_1^2\left(\lambda_{1m}\frac{r}{R}\right). \tag{181}$$

The ϑ integral is elementary and gives π:

$$I_1 = \pi \cosh^2\left(\lambda_{1m}\frac{H}{R}\right) \int_0^R dr r J_1^2\left(\lambda_{1m}\frac{r}{R}\right). \tag{182}$$

To compute the above integral we change variable to

$$x = \frac{r}{R}$$

and obtain

$$I_1 = \pi \cosh^2\left(\lambda_{1m}\frac{H}{R}\right) R^2 \int_0^1 dx x J_1^2(\lambda_{1m}x).$$

Using Maple we obtain

$$\int_0^1 dx x J_1^2(\lambda_{1m}x) = \frac{1}{2}\frac{\lambda_{1m}J_0^2(\lambda_{1m}) + \lambda_{1m}J_1^2(\lambda_{1m}) - 2J_0(\lambda_{1m})J_1(\lambda_{1m})}{\lambda_{1m}}.$$

Using (175) the above is simplified to

$$\int_0^1 dx x J_1^2(\lambda_{1m}x) = \frac{1}{2}\left(1 - \frac{1}{\lambda_{1m}^2}\right) J_1^2(\lambda_{1m}).$$

Hence

$$I_1 = \frac{\pi}{2}R^2\left(1 - \frac{1}{\lambda_{1m}^2}\right)\cosh^2\left(\lambda_{1m}\frac{H}{R}\right) J_1^2(\lambda_{1m}). \tag{183}$$

We define

$$I_2 \equiv \int\limits_C dS\Psi_{1m} = \cosh\left(\lambda_{1m}\frac{H}{R}\right)\int\limits_0^R drrJ_1\left(\lambda_{1m}\frac{r}{R}\right)\int\limits_0^{2\pi} d\vartheta\cos\vartheta.$$

The ϑ integral vanishes and

$$I_2 = 0. \tag{184}$$

We define

$$I_3 \equiv \int\limits_C dS\Psi_{1m}\frac{\partial\Psi_{1m}}{dz}$$

Substituting from (32) we obtain

$$I_3 = \frac{\lambda_{1m}}{R}\cosh\left(\lambda_{1m}\frac{H}{R}\right)\sinh\left(\lambda_{1m}\frac{H}{R}\right)\int\limits_0^R dr\int\limits_0^{2\pi} d\vartheta r\cos^2\vartheta J_1^2\left(\lambda_{1m}\frac{r}{R}\right) =$$

$$= \frac{\pi}{2}\lambda_{1m}\left(1-\frac{1}{\lambda_{1m}^2}\right)R\cosh\left(\lambda_{1m}\frac{H}{R}\right)\sinh\left(\lambda_{1m}\frac{H}{R}\right)J_1^2(\lambda_{1m}). \tag{185}$$

10 Appendix E Transfer function and the Fourier transform

Consider the harmonic oscillator

$$m\ddot{u} + c\dot{u} + ku = p(t), \tag{186}$$

where m, c, k are the mas, viscous damping, and spring constants respectively, p is the external force, and u is the oscillator's response. The transfer function is a function of the angular frequency defined by (see Chopra (2007)):

$$H(\omega) = \frac{1}{-m\omega^2 + i\omega c + k}. \tag{187}$$

Then the response of the oscillator under an arbitrary external force $p(t)$ can be computed in the following threee steps:

(i) We first take the FT of the external force:

$$\hat{p}(\omega) = \int_{-\infty}^{\infty} dt e^{-i\omega t} p(t). \tag{188}$$

(ii) We multiply $\hat{p}(\omega)$ by the transfer function $H(\omega)$ to obtain the FT of the response:

$$\hat{u}(\omega) = H(\omega)\hat{p}(\omega). \tag{189}$$

(iii) We take the inverse FT of $\hat{u}(\omega)$ to obtain the response as a function of time:

$$u(t) = \frac{1}{2\pi} \int_{-\infty}^{\infty} d\omega e^{i\omega t} \hat{u}(\omega). \tag{190}$$

Note however that this provides **one** solution of differential equation (186). Suppose however that we wish the solution to satisfy boundary conditions

$$U(t_0) = U'(t_0) = 0. \tag{191}$$

Let then $u_1(t)$, $u_2(t)$ be the solutions of the **homogeneous** version of (186) (i. e. with the right hand side equal to zero). Then the function $U(t)$

$$U(t) = u(t) + Au_1(t) + Bu_2(t) \tag{192}$$

satisfies (186) and can be made to satisfy boundary conditions (191) if A, B satisfy the linear system:

$$u(t_0) + Au_1(t_0) + Bu_2(t_0) = 0, \tag{193}$$

$$u'(t_0) + Au_1'(t_0) + Bu_2'(t_0) = 0. \tag{194}$$

Finally note that a solution of (186) satisfying given boundary conditions is more often obtained via the Laplace transform. In the present case we prefer the FT since it can be readily adapted to the discrete case via the Discrete Fourier Transform.

11 REFERENCES

Boggess A and Narcowich F J "A First Course in Wavelets with Fourier Analysis", John Wiley and Sons, New Jersey

Chopra A K 2007 "Dynamics of Structures", Pearson-Prentice Hall, New Jersey

Curle N and Davies H J 1968 "Modern Fluid Dynamics Volume 1: Incompresible Flow", D Van Nostrand Company Ltd, LondonStochastic

Dabaghi M & Der Kiureghian A 2014 "Modeling and Simulation of Near-Fault Ground Motions for Performance-Based Earthquake Engineering", Pacific Earthquake Engineering Research Center, University of California, Berkeley

Eurocode 8: Design provisions of earth- quake resistance of structures, Part 4: Silos, tanks and pipelines. European Committee for Standardization, Brussels, 1998.

Haroun M A 1980 "Dynamic Analyses of Liquid Storage Tanks" California Institute of Technology Report EERL 80-04,Pasadena, California

Hoskins L M and Jacobsen L S 1934 *Bulletin of the Seismological Society of America* **24** 1

Housner G W 1954 "Earthquake Pressures on Fluid Containers" California Institute of Technology Report NR-081-095, Pasadena, California

Housner G W 1957 *Bulletin of the Seismological Society of America* **47** 15

Housner G W 1963 *Bulletin of the Seismological Society of America* **53** 381

Jacobsen L S 1949 *Bulletin of the Seismological Society of America* **39** 189

Jaiswal O R, Rai D C and Jain S K 2007 *Earthquake Spectra* **23** 239

Ibrahim R A 2005 "Liquid sloshing and dynamics: theory and applications", Cambridge University Press,New York

Koketsu K and Miyake H 2008 *J Seismol* **12** 133

Mavroeidis G P and Papageorgiou A S 2003 *Bulletin of the Seismological Society of America* **93** 1099

Meirovitch L 2001 "Fundamentals of Vibrations", McGraw-Hill, Boston

Shuang L and Li-li X 2007 *Acta Seismologica Sinica* **20** 105

Spiegel M R 1959 "Vector Analysis", Schaum's Outline Series, McGraw-Hill, New York

Veletsos A S 1984 "Seismic response and design of liquid storage tanks", Guidelines for the Seismic Design of Oil and Gas Pipeline Systems, ASCE, New York, pp. 255

Veletsos A S and Yang J Y 1977 "Earthquake Response of Liquid Storage Tanks", Proceedings of 2nd Annual Engineering Mechanics Division Special Conference, ASCE, New York

Weisstein E W 2014 *Bessel function zeros* From *Mathworld* - A Wolfram Web Resource *http://mathworld.wolfram.com/BesselFunctionZeros.html*

Westergaard H M 1931 *Proceedings of the American Society of Civil Engineers* **57** 1303